Characterisation and *in vivo* validation of contrast agents by means of magnetic resonance imaging

Dissertation

der Mathematisch-Naturwissenschaftlichen Fakultät

der Eberhard Karls Universität Tübingen

zur Erlangung des Grades eines

Doktors der Naturwissenschaften

(Dr. rer. nat.)

vorgelegt von

Tanja Savić

aus Novi Sad, Serbien

Tübingen

2019

Gedruckt mit Genehmigung der Mathematisch-Naturwissenschaftlichen Fakultät der Eberhard Karls Universität Tübingen.

Tag der mündlichen Qualifikation:	29.05.2019
Dekan:	Prof. Dr. Wolfgang Rosenstiel
1. Berichterstatter:	Priv.-Doz.Dr. Goran Angelovski
2. Berichterstatter:	Prof.Dr. Klaus Scheffler

Erklärung/Declaration

„Ich erkläre hiermit, dass ich die zur Promotion eingereichte Arbeit mit dem Titel: “Charakterisierung und *in vivo* Validierung von Kontrastmitteln unter Verwendung der Kernspintomographie” selbständig verfasst, nur die angegebenen Quellen und Hilfsmittel benutzt und wörtlich oder inhaltlich übernommene Stellen (alternativ: Zitate) als solche gekennzeichnet habe. Ich erkläre, dass die Richtlinien zur Sicherung guter wissenschaftlicher Praxis der Universität Tübingen (Beschluss des Senats vom 25.5.2000) beachtet wurden. Ich Amtliche Bekanntmachungen der Universität Tübingen 2015, Nr.5, S. 154 versichere an Eides statt, dass diese Angaben wahr sind und dass ich nichts verschwiegen habe. Mir ist bekannt, dass die falsche Abgabe einer Versicherung an Eides statt mit Freiheitsstrafe bis zu drei Jahren oder mit Geldstrafe bestraft wird.“

“I hereby declare that the thesis I submit for my doctorate with the title: „Characterisation and *in vivo* validation of contrast agents by means of magnetic resonance imaging“ is my own independent work, that I used only the sources and resources cited and have clearly indicated all content adopted either word-for-word or in substance. I declare that the University of Tübingen’s guidelines to ensure good academic practice (Senate decision of 25.5.2000) have been observed. I solemnly swear that this information is true and that I have not concealed any relevant information. I am aware that making a false declaration is punishable by a fine or by a prison term of up to three years.”

Tübingen, den

Datum/Date Unterschrift/Signature

Contents

Abbreviations

BAPTA	1,2-bis (o-aminophenoxy) ethane-N,N,N',N'-tetracetic acid
BBB	blood-brain-barrier
bSSFP	balanced steady state free precession
CA	contrast agent
CCA	common carotid artery
CEST	chemical exchange saturation transfer
CNR	contrast to noise ratio
CSI	chemical shift imaging
CV	cresyl violet
DO3A	1,4,7,10- tetraazacyclododecane- 1,4,7- triacetic acid
DWI	diffusion weighted magnetic resonance imaging
ECA	external carotid artery
FLASH	fast low angle shot magnetic resonance imaging
ICA	internal carotid artery
MCA	middle cerebral artery
MRI	magnetic resonance imaging
paraCEST	paramagnetic chemical exchange saturation transfer
PPA	pterygopalatine artery
RARE	rapid acquisition with refocused echoes magnetic resonance imaging
RF	radio frequency
SNR	signal to noise ratio
tMCAo	transient middle cerebral artery occlusion
TR	repetition time
TTC	Triphenyl tetrazolium chloride
UTE	ultrashort echo time magnetic resonance imaging
ZTE	zero echo time magnetic resonance imaging

Abstrakt

Die Magnetresonanztomographie (MRT) gilt als eine der führenden Techniken für die biomedizinische Forschung und die klinische Diagnostik. Trotzdem sind weitere Entwicklungen erforderlich, um es zu ermöglichen, pathophysiologische Prozesse besser zu erkennen und zu beobachten. Ebenso wichtig ist die Entwicklung eines neuen Ansatzes zur direkten Überwachung der neuronalen Aktivität, da das zur Zeit meistgenutzte Verfahren, das Signaländerungen aufgrund von Variationen im Sauerstoffgehalt des Blutes misst, die tatsächliche Aktivität nur indirekt aufzeichnet. Ein anderer Ansatz, der auf der Anwendung von responsiven MR Kontrastmitteln (rKM) beruht, hat das Potenzial, deutliche Fortschritte bei der Bewältigung dieser Probleme zu erzielen.

Das Hauptziel meines Projektes war die Entwicklung neuer *in vivo* experimenteller Verfahren, die eine direkte Überwachung der neuronalen Aktivität und pathophysiologischer Prozesse ermöglichen sollen. Dazu wurde das Potenzial der rKM eingesetzt, insbesondere derjenigen, die die Verfolgung wesentlicher Biomarker erlauben. In Anwesenheit von rkM wurden verschiedene Stimulationen angewendet, durch die die Homöostase des beobachteten Biomarkers gestört wurde. Dadurch wurde die Messung und Quantifizierung der rKM mit Hilfe von MRT-Bildgebungsprotokollen möglich.
Als wichtigste entwickelte Anwendung wurde eine Methode zum [Ca^{2+}] Tracking etabliert, die für Echtzeit-Detektion und -Überwachung von zerebraler Ischämie genutzt werden kann. Ein solcher Ansatz könnte entscheidende Informationen für die effektive Reaktion auf diese Krankheit bringen, die eine der häufigsten Ursachen für Hirnschäden ist. In einem weiteren Projekt wurden neue Methoden für die konzentrationsunabhängige Abbildung des pH-Wertes, einem wichtigen Biomarker für die klinische Diagnose und Therapieüberwachung von Tumoren, entwickelt. Weiterhin wurden die Vorteile eines neuentwickelten Bildgebungs-Protokolls genutzt, um einen hohen Signalkontrast zwischen Proben von rKM mit unterschiedlichen [Ca^{2+}] erreicht. Zuletzt wurden die Vorteile eines MRI-Kontrastmittel, das wahlweise durch Änderung der T_1-Wichtung, des CEST-Effekts oder des ^{19}F-Signals verwendet werden kann, gezeigt.

Die Ergebnisse dieser Arbeit demonstrieren das große Potenzial von rKM für ein tieferes Verständnis zahlreicher biologischer Prozesse durch die Verfolgung

spezieller Biomarker. Dieses Projekt zeigt eindrucksvoll ihre Bedeutung in der Entwicklung von neuartigen *in vivo* experimentellen Verfahren für weitere Anwendungen, insbesondere für die direkte Echtzeitüberwachung der neuronalen Aktivität sowie anderer pathophysiologischer Prozesse im Gehirn.

Abstract

Magnetic resonance imaging (MRI) is considered one of the leading techniques used in biomedical research and clinical diagnostics. However, much work must still be done in order to enable detection and monitoring of pathophysiological processes. Equally important is the development of a novel approach for the direct monitoring of neural activity, since the present method, blood-oxygen-level-dependent signal, is indirect. A different approach, involving the use of responsive MR contrast agents (rCAs) has the potential to make significant progress in tackling these problems.

The main objective of my project was the development of novel *in vivo* experimental procedures that would allow the direct monitoring of neural activity and pathophysiological processes. To realize this, the potential of rCAs was exploited, particularly those involved in the tracking of essential biomarkers. In the presence of rCAs diverse stimulations were applied, perturbing the homeostasis of the targeted biomarkers. Consequently, this enabled the measurement and quantification of the rCA response using MR imaging protocols. Most importantly, using [Ca^{2+}] tracking a new technique was established that can be used for the real-time detection and monitoring of cerebral ischemia. Such an approach could bring crucial information about the effective recovery from a disease that is one of the most common causes of brain injury. This work also reports on new concentration independent methods for the mapping of pH, an important biomarker in the clinical diagnosis and therapy of tumors. Furthermore, through exploiting the advantages of a novel imaging protocol, high signal contrast between samples of rCA with different [Ca^{2+}] was obtained. Lastly, the benefits of employing an MRI probe that could be utilized either as a T_1-weighted, CEST or ^{19}F MRI CA were emphasized.

Significantly, the findings obtained from this work demonstrate the great potential of rCAs for the deeper understanding of numerous biological processes by tracking targeted biomarkers. Most importantly, this project supports their further application in the developmental advancement of novel *in vivo* experimental procedures. In particular, those that would enable the direct and real time monitoring of neural activity, as well as other pathophysiological processes over the region of interest.

1. Introduction

1.1. MRI and image contrast generation

The principle of MRI is based on the interaction of static and altering magnetic fields with the nuclear spin of magnetic active nucleus ($I \neq 0$), in most cases hydrogen atoms ($I = 1/2$) [1]. At equilibrium, under the presence of B_0, a net magnetization vector aligns with B_0 (z-direction), according to Boltzmann distribution between two states ($I = \pm 1/2$). With the application of a RF pulse perpendicular to the B_0 (xy plane), M is tipped towards xy plane, inducing the precession of M. After the pulse, M relaxes back to its equilibrium state and produces free induction decay that is detected with a radiofrequency coil. Relaxation processes include two independent mechanisms: the interaction of spins with their environment ("spin-lattice" decay) and the dephasing of spins ("spin-spin" decay) (Fig.1). The first mechanism represents the recovery of longitudinal M (T_1), parallel to B_0 and is characterized with the longitudinal relaxation time. T_1 represents the time required for M_z to recover 1-1/e (63 %) of its starting value. The second mechanism, happening simultaneously, implies the decaying of transversal M, represented with the transversal relaxation time (T_2). T_2 is the time necessary to decay M_{xy} down to 1/e (37 %) of its initial value.

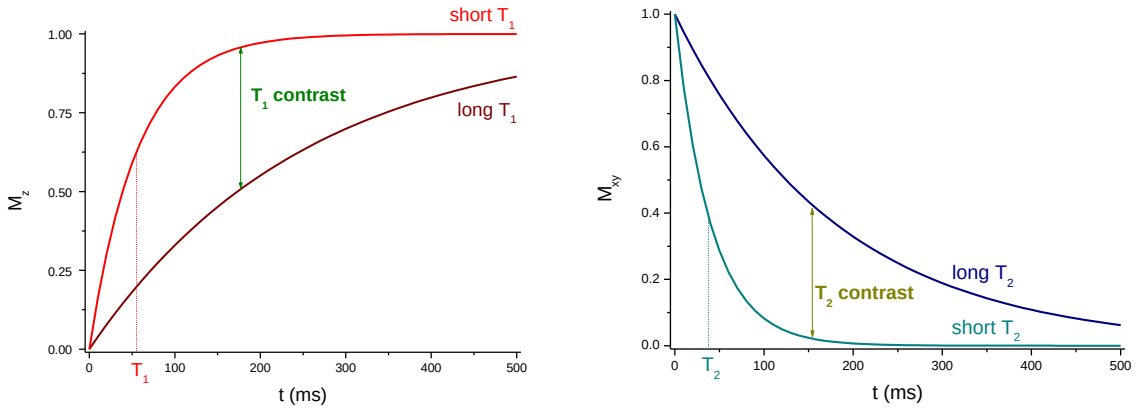

Figure 1. Longitudinal and transversal relaxation of magnetization.

Subsequently, the contrast and brightness of an MR image depends primarily on the spin density and their microenvironment (T_1 and T_2 relaxation times). Nonetheless, with the development of advanced imaging pulse sequences, it became possible to emphasize desired contrast mechanism and therefore increase the sensitivity of the MRI measurement.

1.1.1. T_1- *and* T_2-weighted MRI

T_1-weighted MRI emphasizes the difference in T_1 relaxation times of distinctive tissues. It is based on M_z relaxation. Namely, after application of the RF pulse, M_z returns back to its equilibrium state, however, depending on the tissue T_1 relaxation time, the recovery of M_z will take a characteristic time, thus producing an image with T_1-weighted contrast. Tissue with the short T_1 relaxation time will recover most of its initial M_z during a given repetition time and thus appear brighter on the T_1-weighted image.

T_2-weighted MRI highlights the difference in T_2 relaxation times of distinctive tissues. It is based on M_{xy} relaxation. Here, after application of B_1, M_{xy} starts decaying. This process depends on the T_2 relaxation time of the tissue, and for some imaging pulse sequences also on magnetic field inhomogeneity that additionally shortens T_2 relaxation time. Opposite to T_1 weighted contrast, tissue with a shorter T_2 relaxation time, even though it relaxes faster, appears darker on the image since it induces signal for a shorter time.

Another image contrast has been introduced with the development of bSSFP, a rapid gradient-echo imaging pulse sequence [2, 3]. Namely, under specific conditions the MR signal will depend on T_2/T_1 ratio of the tissue, where tissues with higher T_2/T_1 ratios will appear brighter. The main benefits of T_2/T_1-weighted MRI is sub-second acquisition times, and a much higher signal to noise ratio per time than typical T_1- and T_2-weighted imaging sequences [4].

1.1.2. Chemical Exchange Saturation Transfer imaging

Chemical exchange saturation transfer is another technique that can be used to generate the MRI signal [5]. It is based on the chemical exchange between the solute protons that resonate at different frequency from the bulk water. Requirement for such system to produce the CEST effect is that the chemical exchange rate between solute protons and the bulk water falls under condition $\Delta\omega \geq k_{ex}$ [6, 7]. Practically, a selective RF pulse is sent to saturate the solute protons at their resonant frequency. If the aforementioned requirements are met, the saturated protons will chemically exchange with the bulk water before relaxing (Fig.2).

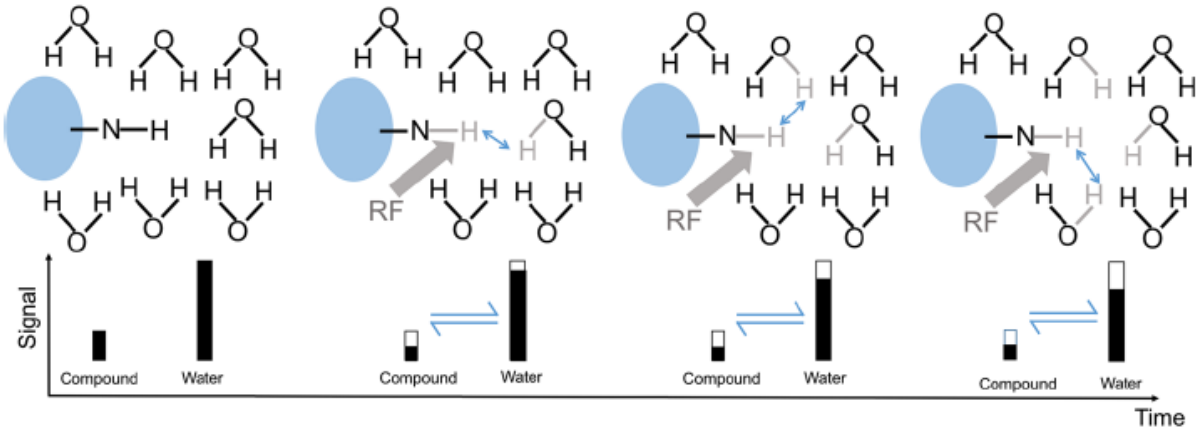

Wu. B., et al., *An overview of CEST MRI for non-MR physicists.* EJNMMI Physics. 2016.

Figure 2. CEST mechanism. In a water solution containing a compound with an amine group a selectively saturating RF pulse is applied at the frequency of amine protons. Saturated amine protons exchange with the surrounding water protons, resulting in the reduction of the water signal (vertical bars).

This process causes a decrease of *M* of bulk water that depends primarily on the magnitude of chemical exchange between the bound and bulk water protons [8]. As a result, CEST allows the indirect visualization of the saturation of solute protons through the observation of bulk water.

1.2. Advancement in MRI with the application of contrast agents

MRI is of great significance because of its non-invasive nature, unlimited tissue penetration depths and excellent spatiotemporal resolution. The technique's main drawback is represented by its poor sensitivity, resulting in the need for long acquisition times. Nonetheless, the development of MRI CAs has helped partially overcome this issue thanks to the enhancement of MRI signal they are able to induce. This lead to a large expansion of MRI applications, such as visualization of anatomical features and tissue functions [9]. It became possible to display with high reliability, blood vessels, track vascular perfusion and capillary permeability. Pathologies related to the disruption of the blood brain barrier such as multiple sclerosis or ischemic stroke could now also be detected. Crucially, the application of CAs allowed for improved differentiation between pathological and healthy tissues, which is important in establishing earlier diagnosis and treatments of many diseases [10].

1.2.1. T_1- and T_2-weighted contrast agents

These MRI CAs act by influencing T_1 (T_1 agents) and/or T_2 (T_2 agents) relaxation times of the neighboring nuclei, in most cases water protons. Reduction of relaxation times is accomplished using thermodynamically stable and kinetically inert complexes with highly paramagnetic metal ions, most commonly Gd^{3+}. While the application of T_1 CAs results in an enhancement, T_2 CAs instead cause a reduction of MRI signal. Therefore, they are also known as positive and negative CAs respectively [11].

1.2.1.1. Responsive contrast agents

A new class of contrast agents, known as responsive CAs have recently been developed [9, 12, 13]. Their main characteristic is the capability of altering their MRI relaxation efficiency in response to changes in the physical-chemical properties of their microenvironment. Essentially, these responsive CAs greatly contributed to the monitoring of various biological processes [14]. They are developed to report on enzyme activity, temperature, proteins and redox states, all of which are important biomarkers for the evaluation of disease states [9, 15]. Moreover, studies of metabolism, especially their involvement in neurochemical signalling processes benefited greatly with the usage of metabolite-responsive CAs [16-18]. Lastly, metal responsive CAs contributed notably to the assessment of the roles of metals in biological signalling pathways, redox homeostasis and neurodegenerative diseases [19, 20].

The design of such a CA should be attentive. It must be ensured that the MRI sensitivity of the responsive CA to a specific biomarker corresponds to its triggered variations under physiological conditions. Additionally, rather than high absolute values of relaxivity, their most important characteristic is the absolute Δr caused due to the presence of the biomarker. The greater the Δr is, the higher the sensitivity of a responsive CA for the desired biomarker, which was well demonstrated in the work of Jasanoff et.al. [18].

1.2.1.1.1. Calcium responsive contrast agents

CAs responsive to endogenous metal ions have received special attention because of their vital roles in biological signalling pathways and pathologies, as demonstrated in the extensive studies performed so far [21, 22]. Ca^{2+} is one of the most crucial metal

ions for the normal functioning of the organism and has essential roles in blood clotting, muscle contraction, fertilization and bone formation. Moreover, Ca^{2+} is of great importance for signal transduction pathways, where it acts as a secondary messenger. Equally, Ca^{2+} has a significant role in neurotransmitter release and lastly in neuronal activity [23-26]. Consequently, it is of paramount interest that such CAs are designed and successfully applied to *in vivo* systems. Specifically, in neuroimaging, Ca^{2+} responsive CAs, could replace the indirect reading of neuronal activity, commonly performed using the blood oxygenation level dependent signal [27].

The first reported calcium responsive CA (DOPTA-Gd) has two Gd-DO3A units linked by a BAPTA analog [28], known for its high selectivity for calcium [29, 30]. Without Ca^{2+}, the BAPTA iminodiacetate groups coordinate with Gd^{3+}, subsequent addition of Ca^{2+} causes them to flip and selectively bind Ca^{2+}. Consequently, due to these conformational changes, a coordination site becomes available for water to bind Gd^{3+} and thus increase the relaxivity of the complex. This mechanism has been used for many further CA designs, focused on optimizing the affinity towards extracellular Ca^{2+}, which is a more suitable target for MRI. For this purpose, derivatives of a few acyclic calcium chelators were used [31-37]. Interestingly, a Gd-DO3A system connected to a hexyl aminobis (methylenephosphonate) chelate reported an inverse response to Ca^{2+}, resulting in a decrease in relaxivity upon the addition of Ca^{2+} [38, 39]. Although these CAs showed remarkable sensitivity to Ca^{2+} changes, their *in vivo* diffusion was rather fast [40]. To overcome this problem, Ca^{2+} responsive CAs based on nanosystems were designed. Conjugating a high number of monomeric units of CA to nanosized systems [4, 41-46] allowed for longer imaging times resulting in an enhanced MR signal, while still retaining a high sensitivity for Ca^{2+}.

1.2.2. ParaCEST agents

CEST CAs present an alternative to gadolinium based MRI CAs [47]. The first exogenous agents were diamagnetic molecules with exchangeable -NH or -OH groups [8, 48]. However, their exchange protons resonances offsets were typically < 5 ppm from the bulk water. ParaCEST agents (CEST CAs with paramagnetic metal ions) on the other hand could induce much greater frequency shifts [47, 49, 50], thus having much faster exchange rates (typically 10^2-10^4 Hz) before reaching the boundary condition ($\Delta\omega \geq k_{ex}$). Typical lanthanide based CAs with coordinated water (excluding Gd^{3+}) [51] could be used as paraCEST CAs if their water exchange rates

fulfills the already mentioned requirement [49, 52, 53]. Simply, these CAs should have neither too fast water exchange, because then water would not be completely saturated, or too long, since then saturated water would not be efficiently exchanged. Therefore, further tuning could be obtained using different donor groups like amide and ketone derivatives [54-59] modifying the overall charge of the complex and steric hindrance at the site of water coordination [51, 53]. Nonetheless, even with optimized $\Delta\omega$ and k_{ex}, the sensitivity of paraCEST CAs still remains an issue. Therefore strategies to increase the number of exchangeable protons were also exploited [60-63].

With a choice of paramagnetic ion there is great potential for the fine-tuning of frequency shifts and relaxation of paraCEST CAs [64-67]. Equally importantly, the effect of paraCEST CAs could be controlled with presaturation pulse, i.e. it can be switched ‘’on’’ and ‘’off’’ at will [8]. These properties allow for the administration of multiple paraCEST CAs simultaneously, while being able to image each one of them individually [10, 68]. Consequently, they could be quite valuable responsive CAs. Similarly to T_1 and T_2 responsive CAs, they are beneficial for the determination of enzyme activity and temperature [9]. Tracking of metabolites such are glutamate and creatine facilitate the treatment of disorders in the central nervous system as well as aid the diagnosis of various muscle conditions [69]. In addition, with their binding to nucleic acids, they noticeably contributed to gene therapy tracking and thus disease treatments [70, 71].

ParaCEST agents that possess amide or amine exchangeable protons are of particular interest for pH sensing, because their chemical exchange with bulk water is base-catalyzed [53]. The tracking of pH is of great importance for clinical diagnosis, since it can significantly contribute to the characterization of tumors and monitoring of the efficacy of pH-dependent therapies [9, 72]. Additionally, such pH responsive paraCEST CAs could improve the diagnosis of many other pathologies such are ischemia and renal failure [15].

pH sensitivity was confirmed on a tetraamide-based ligand with phosphonate side chains [73]. Nevertheless, for an accurate determination of pH *in vivo,* the knowledge of the local CA concentration ([CA]) is required. As that is difficult to achieve, a ratiometric approach proposed by Ward et.al. that circumvents this problem became common [74]. Subsequently, pH monitoring was obtained with the co-injection of two different paraCEST CAs [75]. Further designs were based on single paraCEST CAs

with two non-equivalent CEST signals. Some of them include pH responsive amide protons and coordinated, unresponsive water molecule [76, 77], while others included pH responsive hydroxylic, amide and amine ligand groups [78-82]. Lastly, pH responsiveness was also obtained via changes in line width and the chemical shift of paraCEST agents [83, 84].

1.3. *In vivo* MRI with contrast agents

The utilization of contrast agents represents a breakthrough in the field of MRI applications. These agents improved the SNR images to such an extent that now more than 30 % of MRI experiments are performed in the presence of CAs [11]. However, despite the substantial progress in the development of CAs, their *in vivo* utilization remains challenging.

Commercially available CAs are of great significance in MRI diagnostics, providing enhanced contrast between normal and pathological tissues. For this purpose, the CA is noninvasively administered using intravenous injection. However, in preclinical neuroimaging, infusion of the CA requires alternate methods of administration. This is because the BBB presents one of the main obstacles for the non-invasive delivery of CAs in the brain. Even though new techniques for delivery through the BBB are immerging [85], invasive intracranial CA administration remains the most commonly used to ensure local delivery of the CA into the desired region of interest. Typically, this includes direct intracranial injection of the CA before MR imaging, or the implantation of a catheter or a pump for the continuous delivery of the CA during an experiment. Regardless of the chosen method of CA administration, it should be ensured that the infused local [CA] is sufficient in order to enhance the MR signal long enough during MRI acquisition. For that reason, diffusion of the CA should also be accounted for. Monomeric CAs diffuse rather fast, therefore for their administration higher [CA] are typically being used, however care must be taken not to impair the biocompatibility of the *in vivo* system [9]. Moreover, higher [CA] could cause additional issues, for example the CA could agglomerate, consequently reducing the T_2 relaxation time to such an extent that the MR image intensity could be significantly reduced or completely lost. Thus, another approach would be to use CAs based on nanosized systems (Chapter 1.2.1.1.1). In addition to improved sensitivity, they also allow longer recording times, due to their prolonged tissue

retention times [12].

Regardless, the effectiveness of contrast agents *in vivo* could be quite different from their behaviour *in vitro*, possibly even below detection limits. Focusing on extracellular CAs, once they are injected, they experience significantly different environments to that of *in vitro* experiments [86], meaning not only their diffusion through extracellular space is now compartmentalized, but also the viscosity is changed and the potential binding to proteins could additionally alter their response [87]. Consequently, relaxation obtained *in vitro* could be used only as an estimate for the *in vivo* environment, as relaxation rate of CAs *in vivo* are not necessarily linearly related to their concentration.

Moreover, in the case of CEST, CA proton/water exchange rates could be altered due to the presence of charged species like carbonates and phosphonates [5, 53]. Furthermore, besides CEST, there are competing processes that also contribute to changes of the bulk water signal *in vivo*. Namely, water could be saturated directly via exchangeable protons with small frequency shifts or the exchange could occur between bulk water and protons bound to semi-solid macromolecules with very short T_2 relaxation times. Therefore to reliably analyse CEST, Z- (CEST) spectra [8, 88] are used. Lastly, it should also be mentioned that the irradiation radiofrequency pulse for *in vivo* CEST MRI is rather constrained. Namely, the maximal length of the pulse is limited by the duty cycle of the amplifier. Most importantly, according to regulations the maximal specific absorption rate that object could receive must be restricted, thus the irradiation pulse saturation power and time must be set under a certain level.

1.3.1. *In vivo* MRI with responsive contrast agents

Responsive CAs also generate MR signal, however, what makes them unique is that they respond to changes in their microenvironment by altering their MR signal. For that reason, these CAs are capable of reporting the changes of various biomarkers in their proximity, and therefore are of great importance in developing a better understanding of biological processes that are necessary in the functioning of organisms.

Not every biomarker could be used as a target for rCAs. MRI is an imaging technique with low sensitivity, thus, only biomarkers present in μM concentrations

and above could be considered as viable targets [89]. Once chosen it is essential that high selectivity of the rCA towards the selected biomarker is achieved. However, for *in vivo* applications this presents a difficult task, since other competitive species could also be present, depending on the location of rCA administration. However, in any case, the occurrence of false positive signals or non-responsiveness of rCAs should be avoided.

Signal in MRI generally comes from the ^{1}H present in the tissue. Once the rCA is administered, a higher MR signal is generated. Unlike the case with non-responsive CAs, enhanced MR signal now depends on both the [rCA] and the [biomarker]. Accounting for the fact that these MR signal contributions cannot be separated, a few aspects must further be elaborated. Firstly, saturation of rCA with the biomarker should be avoided. This means that the condition [rCA] ≥ [biomarker] should be satisfied in order to be able to detect and monitor biomarker alterations. However, care must be taken so that the applied [rCA] does not impair the functioning of biological processes [33]. Secondly, the administered [rCA] in the region of interest should be sufficiently high so that MR signal changes, due to corresponding biomarker variations, could be detected. This means that additional MR signal alterations should be considered and compensated. For instance, loss of MR signal due to administered rCA diffusion through the tissue or binding of rCA to cell membranes. Additionally, some *in vivo* stimulations could cause alteration of normal animal physiology, thus could affect corresponding MR signal, as it is the case with tMCAo that causes reduces regional diffusion in the injured brain regions. Typical way to resolve these problems is by conducting control experiments. However, whenever possible, additional animal experiments or more complex animal surgeries should be avoided.

When utilizing rCAs, as mentioned, relaxivity changes occur not solely because of the alterations in their concentration but also of the targeted biomarker. This further means that a different MR signal could be obtained for the voxels exhibiting the same [biomarker] for example, but different [rCA]. Accordingly, in order to obtain meaningful results of the biomarker variations, local [rCA] should be known. However, this is not easily achievable, since the relaxivities that are obtained from *in vitro* calibrations cannot be used per se for *in vivo* systems [89], and so far direct *in vivo* determination of [rCA] has not been achieved [69, 90]. Instead, strategies to

evaluate [rCA] based on approximations like *in vitro* measurements [91-95] are used, or alternatively, concentration independent methods using ratiometric R_2/R_1 [96-98] or dual mode MRI [99, 100]. Still, most of these strategies are based on assumptions or require addition animal experiments.

Finally, *in vivo* experiments demand MR imaging protocols and also hardware that should meet specific requirements. This means, in some cases, additional time for preparation, testing and optimization must be spent before first experiments could be initiated. Moreover, expertise in data analysis could be needed in order to extrapolate the MR signal changes exclusively due to the biomarker changes, independently of other physiological variations. Last but not least, triggering of desired biomarker changes sometimes requires demanding and time consuming animal preparation, which optimization requires a certain period of time, as in the case of surgical preparation for remote tMCAo.

All the above mentioned, represent the everyday difficulties that must be dealt with when performing *in vivo* experiments. Nevertheless, research groups are continuously working on new designs that would enhance the MR rCAs responsiveness, as well as development of new methods that could expand their MRI application.

EBERHARD KARLS
UNIVERSITÄT
TÜBINGEN

Mathematisch-Naturwissenschaftliche Fakultät

Erklärung nach § 5 Abs. 2 Nr. 8 der Promotionsordnung der Math.-Nat. Fakultät

-Anteil an gemeinschaftlichen Veröffentlichungen-

Declaration according to § 5 Abs. 2 No. 8 of the PhD regulations of the Faculty of Science

-Collaborative Publications-

Savić, Tanja

List of Publications

1. Ratiometric Method for Rapid Monitoring of Biological Processes Using Bioresponsive MRI Contrast Agents. *ACS Sensors* **2016,** *1* (5), 483-487.
2. Early detection and monitoring of brain ischemia using a calcium-responsive MRI probes. **In preparation.**
3. Paramagnetic lanthanide chelates for multicontrast MRI. *Chemical Communications* **2016,** *52* (59), 9224-9227.
4. Paramagnetic Macrocyclic Platform for Efficient pH Mapping via CEST MRI. **Submitted.**

Nr.	**Accepted publication yes/no**	**List of authors**	Position of candidate in list of authors	Scientific ideas by the candidate (%)	Data generation by the candidate (%)	Analysis and Interpretation by the candidate (%)	Paper writing done by the candidate (%)
1	yes	6	1	15	45	40	50
2	no	6	1	40	70	50	35
3	yes	9	2	20	30	40	20
4	no	7	1	20	60	50	20

I confirm that the above-stated is correct.

_____

Date, Signature of the candidate

I/We certify that the above-stated is correct.

_____

Date, Signature of the doctoral committee or at least of one of the supervisors

3. Own work

The goal of my PhD project was to develop methodologies that would enable the direct monitoring of neural activity and pathophysiological processes over the whole brain. The concept was to design novel approaches for the unambiguous detection and monitoring of specific biomarkers in *in vivo* systems that are directly involved in a process under investigation. Accordingly, my work was mainly based on the characterization and *in vivo* validation of responsive CAs that included MRI experiments under various artificial and physiological stimulations of the targeted biomarkers.

As a result of my PhD project, a method that could track earliest changes during cerebral ischemia and also provided a mean for the direct monitoring of many other processes including neural activity (Chapter 3.2) was successfully developed. Moreover, approaches for the tracking of pH, which is important in the diagnosis and therapy monitoring of tumors (Chapter 3.4), were established. Furthermore, the advantages of a novel MRI imaging protocol that enables much faster acquisitions with a significantly increased contrast to noise ratio between rCA samples with different [Ca^{2+}] was elaborated. Thus, contributing to faster MRI acquisitions with rCA and their improved biomarker response range [4]. Lastly, the benefits of using a CA that could be used for the acquisition of multiple MRI contrasts [101] was also presented.

The above mentioned projects are summarized in the next sections.

3.1. Ratiometric Method for Rapid Monitoring of Biological Processes Using Bioresponsive MRI Contrast Agents

3.1.1. Background/Hypotheses

Responsive MRI contrast agents represent a powerful tool for the targeting of specific biomarkers. These CAs alter their MR signal as a consequence of changes in their microenvironment [9, 13]. Accordingly, many MRI rCAs have been developed so far, all aiming to produce maximal MR signal change upon specific biomarker alterations. However, what is difficult to achieve for these CAs is obtaining *in vivo* MR changes above the detection level, as a response to an alteration in their microenvironment, while accounting for [CA]-dependent MR signal variations.

In this study, a method for the dynamic monitoring of [Ca^{2+}] that was achieved by exploiting the rCAs distinct alterations of T_1 and T_2 with Ca^{2+} using a rapid imaging protocol was introduced. Accordingly, this study offers promising results that could lead to direct tracking of [Ca^{2+}] changes in *in vivo* systems and, consequently, monitoring of numerous biological processes including neural activity.

3.1.2. Materials and Methods

Dr. Serhat Gündüz has synthesized the dendrimeric rCA (**DSCA**) by coupling a monomeric rCA (**MSCA**) [41] with a fourth generation dendrimer. He also performed NMR relaxometric titrations [4]. Diffusion properties of both rCAs as a function of Ca^{2+} presence were performed using DLS and/or NMR spectroscopy. NMR diffusion experiments were used for **MSCA**, since its size was below the detection limit for DLS. These measurements were done on their respective Eu^{3+} analogues and included recordings (0.75 mM and 15 mM Eu^{3+} for DLS and NMR respectively) in the presence and absence of two equivalents of Ca^{2+}. MRI performed on tube phantoms included buffered solutions of **MSCA** and **DSCA** (1 mM Gd^{3+} concentrations) with different [Ca^{2+}] (0, 0.4, 0.8, 1.2 equivalents) that resembled the conditions in the anticipated functional MRI experiments [33]. Imaging included a comparison of typical T_1- (FLASH), T_2- (RARE) and T_2/T_1- (bSSFP) weighted imaging protocols, optimized for the highest CNR for each rCA, using numerical optimizations based on Bloch simulations.

3.1.3. Results and Discussion

Relaxometric titrations with Ca^{2+} showed that r_1 increased by 70 and 130 % for **DSCA** and **MSCA** respectively, which is to be expected for such systems [41]. On the other hand, r_2 increased greatly for **DSCA** (360 %), while **MSCA** changed in a similar range to its respective r_1 variations with Ca^{2+}. Combining these two effects and presenting their ratio, R_2/R_1, it was evident that significant changes could be observed for **DSCA**, while **MSCA** remains rather insensitive to Ca^{2+} (Figure 3).

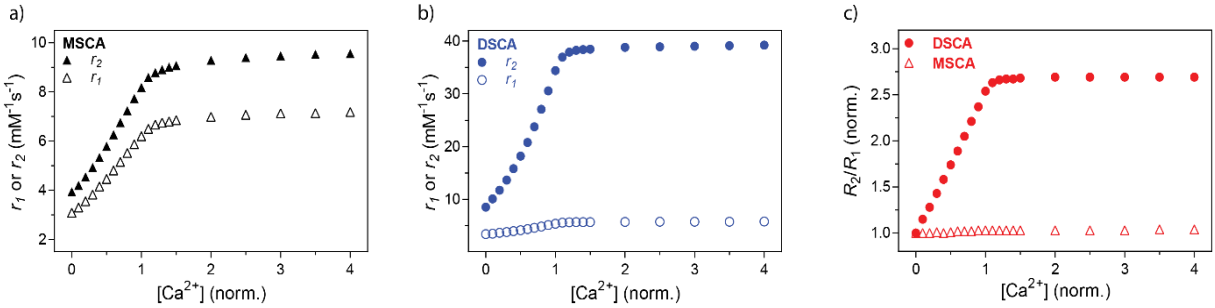

Figure 3. The effect of Ca^{2+} on a ratio of longitudinal and transverse relaxivities at 7 T (pH 7.4). r_1 and r_2 for **MSCA** (a) and **DSCA** (b) upon saturation with Ca^{2+} (HEPES), or its effect on the R_2/R_1 ratio on **MSCA** and **DSCA**, respectively (c). [Ca^{2+}] was normalized with concentration of Gd^{3+} (3 mM). The R_2/R_1 plots show normalized values where the final value (at Ca^{2+} saturation) is divided by the initial value (in absence of Ca^{2+}).

Accordingly, it can be discussed that even though **DSCA** showed a smaller increase in r_1 than **MSCA**, its application for functional T_2- and especially T_2/T_1-weighted imaging is quite suitable. Furthermore, diffusion measurements interestingly showed that the diffusion coefficient for both **MSCA** and **DSCA** reduces upon the addition of Ca^{2+} (Table 1).

Table 1. Diffusion coefficients and sizes obtained for Eu^{3+} complexes of **DSCA** and **MSCA**

Contrast agent	**Diffusion coefficient (10^{-11} m^{2}s^{-1})**		**Diameter (nm)**	
	No Ca^{2+}	+ Ca^{2+} (2 equiv)	No Ca^{2+}	+ Ca^{2+} (2 equiv)
DSCA	9.2 ± 0.9[a] 8.2 ± 0.7[b]	6.0 ± 0.2[a] 7.3 ± 0.2[b]	5.4 ± 0.5[a]	8.3 ± 0.3[a]
MSCA	32.0 ± 0.5[b]	28.3 ± 0.7[b]	1.5 ± 0.1[b]	1.7 ± 0.1[b]

[a]DLS measurements. [b]NMR measurements

The diameter of **DSCA** without Ca^{2+} (5.4 ± 0.5 nm) correlated well with previously published conjugates with G4 generation PAMAM dendrimers [102], while upon addition of Ca^{2+} its diameter increased significantly (8.3 ± 0.3 nm). Comparable results, however with lesser effect were obtained with **MSCA**, where diameter increased from 1.5 ± 0.1 nm to 1.7 ± 0.1 nm. These results clearly indicated that the addition of Ca^{2+} caused intramolecular conformational changes that induced the expansion and rigidification of **Ca-MSCA**/**Ca-DSCA** complexes respectively. Consequently, these changes influenced r_2 which was particularly observable for **DSCA**. Furthermore, MRI on tube phantoms depicted the advantage of the bSSFP imaging protocol (Figure 4).

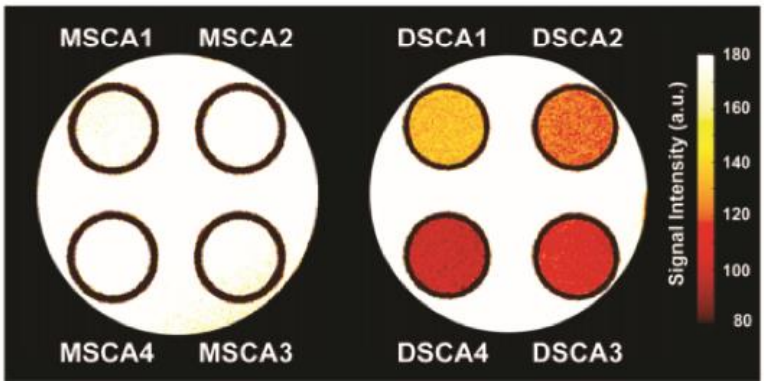

Figure 4. MRI on tube phantoms with **MSCA** and **DSCA** in the presence of Ca^{2+}. MR images obtained with bSSFP for different concentrations of Ca^{2+} (**MSCA** 1-4 or **DSCA** 1-4 indicate 0, 0.4, 0.8, 1.2 mM Ca^{2+}, respectively, [Gd^{3+}] = 1mM, pH 7.4, HEPES).

MR images with **DSCA** showed obvious changes in the T_2/T_1-weighted signal for samples with different [Ca^{2+}], while the **MSCA** signal remained unaltered. However, it must be pointed out that MRI with bSSFP requires a highly homogeneous magnetic field. Thus, even with MRI on tube phantoms, care must be taken that no significant change in the susceptibility exists, for example when the samples are placed free in the sample holder. Instead they should be immersed in water, making sure no air bubbles are present. Optionally, water could even be enriched with CA, resembling the relaxation time of the samples.

In order to make a comparison between the acquired imaging sequences, their SNR values were analyzed (Table 2).

Table 2. SNR values obtained for **DSCA** and **MSCA** in the presence and absence of 1.2 equiv. Ca^{2+}, using T_1, T_2- and T_2/T_1-weighted imaging sequences.

Contrast agent	T_1-weighted (FLASH) [a]		T_2-weighted (RARE) [b]		T_2/T_1-weighted (bSSFP) [c]	
	No Ca^{2+}	+ Ca^{2+} (1.2 equiv.)	No Ca^{2+}	+ Ca^{2+} (1.2 equiv.)	No Ca^{2+}	+ Ca^{2+} (1.2 equiv.)
DSCA	5.41	6.27	**11.83**	**8.50**	**9.75**	**7.39**
MSCA	4.81	6.12	13.44	12.60	10.41	10.95

a) **DSCA**: AT=3888 ms, **MSCA**: TA=3481 ms; b) **DSCA**: AT=9920 ms, **MSCA**: AT=14400 ms; c) TA=767.5 ms.

Namely, with bSSFP a 30 % signal change between samples with and without Ca^{2+} was obtained in just 0.8 seconds with SNR ~ 7-10. This presented a large signal alteration which was twice that which could be acquired using T_1-weighted imaging (14 % signal increase for **DSCA**, SNR ~ 5-6) with the same number of repetitions, while also recording for five times longer (4 seconds). Lastly, with T_2-weighted imaging the highest SNR and signal changes (SNR ~ 8-12, 40 %) were obtained, yet such results required the longest acquisition times, significantly longer than with bSSFP (10 seconds). Still, in order to have a direct comparison between imaging modalities, their CNR per unit of time were calculated and compared (Figure 5).

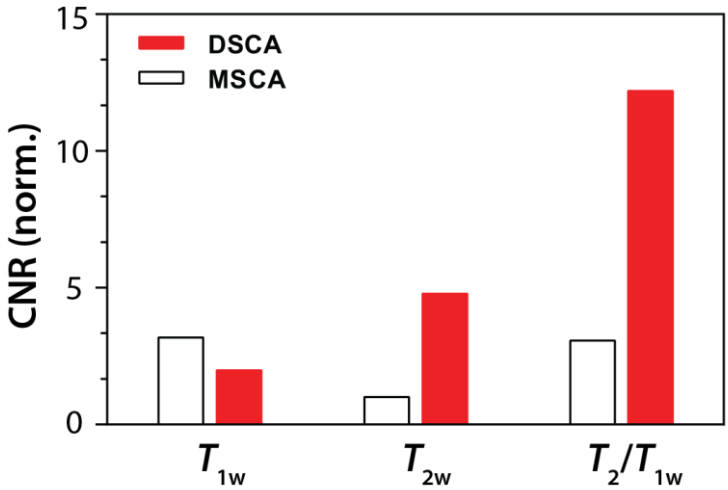

Figure 5. Comparison of normalized CNR for **MSCA** and **DSCA**, obtained with T_1-, T_2 -, T_2/T_1 -weighted imaging sequences. CNR values were obtained by subtracting SNR values and normalizing them by the square root of the respective acquisition time.

These results demonstrated that with bSSFP and **DSCA**, a CNR enhancement is more than two and a half times greater than T_2-, and six times greater than with the T_1-weighted imaging method. Moreover, such a method allowed for a CNR four times higher than that obtained for T_1-weighted imaging, a commonly used imaging modality with small sized rCAs, demonstrated here with **MSCA**.

3.1.4. Conclusion

It was demonstrated that the reported method can record changes in [Ca^{2+}] with sub-second temporal resolution and high CNR between samples with different [Ca^{2+}]. This further implies that our approach shows great potential for the monitoring of various biological processes that include Ca^{2+} alterations. Moreover, these results may have a much greater biological significance since our approach could be employed for the recording of neural activity in a direct manner with Ca^{2+} as its biomarker.

3.2. Early detection and monitoring of brain ischemia using a calcium responsive MRI contrast agent

3.2.1. Background/Hypotheses

Cerebral ischemia is one of the leading causes of mortality and disability in the world [103, 104]. The severity of brain injury caused by ischemia depends on complex pathophysiological processes. The duration of ischemia is one of its essential factors. In cases where blood flow could be re-established fast enough, the extent of tissue injury could be reduced and even restored within the penumbra [105].

Commonly used techniques for the diagnosis of cerebral ischemia fail in the detection of its early chronic stage [106-108]. Accordingly, a method that could detect ischemic changes in real time would significantly improve the chances of injury recovery. Upon cerebral ischemia, along with the cascade of occurring events, $[Ca^{2+}]$ decreases dramatically [25, 26]. Consequently, we have developed a method that is able to directly monitor the intensity and duration of cerebral ischemia by the real time tracking of *in vivo* variations of $[Ca^{2+}]$.

3.2.2. Materials and Methods

Synthesis of Ca^{2+} rCA $\mathbf{Gd_2L^1}$ was previously published [31], while the design, preparation of the control CA $\mathbf{Gd_2L^2}$ and NMR relaxometric titrations were performed by Dr. Giuseppe Gambino. The *in vitro* T_1-weighted MRI phantom contained 4 vials (each 350 µL) with $\mathbf{Gd_2L^1}$ and $\mathbf{Gd_2L^2}$ (1.25 mM CA = 2.5 mM Gd^{3+}) prepared with and without $[Ca^{2+}]$ (1.25 mM).

In vivo experiments were performed on male Wistar rats (300-340 g). Both CAs were continuously infused using an osmotic pump. The reservoir of continuous pump was placed subcutaneously in the dorsal side of the animal and the infusion cannula of the pump (3.6 mm depth) was fixed at the craniotomy site made in somatosensory cortex region using stereotaxic surgery.

The remote occluding device consisted of three main parts: 1) support tubing (PE-160, length 108 cm) with a custom made connector, 2) intra-arterial catheter (PE-50, length 1.5 cm), and 3) occluder (diameter 5-0, length 0.31 mm, 5-6 mm silicone coating) with its extension (PE-90, length 121 cm).

For remote tMCAo preparation, the animal was placed into the supine position and a 2 cm midline neck incision was made. Thereafter, the right CCA bifurcation was

exposed and its branches isolated. OA was double ligated (7-0) and dissected. The CCA and ECA were ligated (7-0) and the ICA was temporary clipped. Then, arteriotomy was performed on the distal part of the CCA, where the intra-arterial catheter, filled with heparin, was introduced until reaching the ECA/ICA bifurcation, and then fixed with two ligations (4-0). Support tubing was passed through the skin of the animal close to the incision site and then connected with the intra-arterial catheter. Following this, the occluder was advanced through the support tubing until the clip on the ICA. The clip was then removed and the occluder was quickly advanced until passing the bifurcation with the PPA; subsequently, the ICA was ligated with 7-0 ligature to stop the residual bleeding. Following the fixation of the support tubing, the wound was closed. To occlude the MCA inside the MRI scanner, the occluder extension was remotely advanced for 6-8 mm, until the resistance was felt, while reperfusion was performed with the opposite action.

In vivo MRI consisted of acquisitions using T_1-weighted and DWI sequences. The first part of MRI was divided in three sections: pre-ischemia (21 minutes), ischemia (53 minutes), and reperfusion period (31 minutes). During that time T_1-weighted images were acquired every 2 minutes. Thereafter DWI was recorded for confirmation of ischemia. Lastly, the catheter of the continuous pump was cut, and the diffusion of the CA was recorded (81 minutes) by acquiring T_1-weighted images as described above.

Analysis of the above mentioned MRI data was done by Dr. Vahid Bokharaie.

3.2.3. Results and Discussion

In vitro MRI phantom experiments in buffered media confirmed the results from *in vitro* relaxometric titrations that showed a difference in response of CAs as a function of [Ca^{2+}]. Namely, $\mathbf{Gd_2L^1}$ samples showed a significant change in T_1-weighted signals with the trend that the signal increased with addition of Ca^{2+}, while T_1-weighted signals of $\mathbf{Gd_2L^2}$ samples remained insensitive to [Ca^{2+}] (Figure 6).

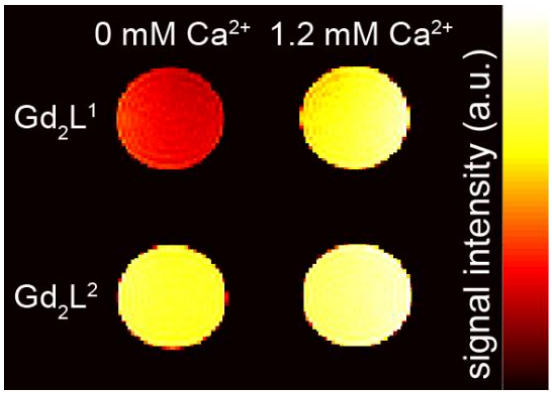

Figure 6. T_1-weighted MRI on tube phantoms. **Gd_2L^{1-2}** (2.5 mM Gd^{3+}) without and with 1.2 mM Ca^{2+}.

To confirm that this molecular MRI method is capable of detecting [Ca^{2+}] changes upon a relevant clinical event tMCAo protocol was used, as a reproducible model for transient cerebral ischemia. This model was chosen considering that the occlusion of the MCA and its branches causes about 70 % of human ischemic strokes worldwide [109, 110]. Our method consisted of continuous infusion of the CA (n=5 animals/CA), together with the tMCAo performed remotely, outside of the MRI scanner (Figure 7).

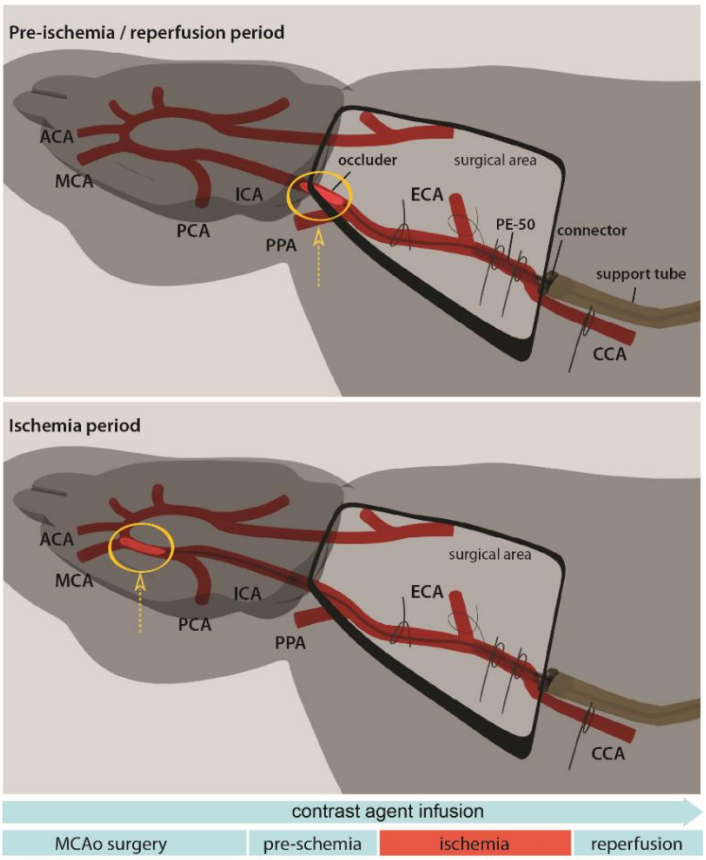

Figure 7. Preparation of the animal for tMCAo and the course of the experiment; Positioning of the occluder in the pre-ischemia and the reperfusion period (top) or during ischemia induction (middle). The location of the occluder is marked with the yellow circle. Course of experimental procedure (down).

Figure 7 depicted that the continuous infusion of the CA was performed at the very beginning of the experiment. With such an approach there was high enough T_1-weighted signal from the CA to start imaging as soon as MCAo preparation was completed and animal was transferred into the MRI scanner. However, it should be mentioned that such continuous pumps could get blocked during cannula insertion in the brain tissue. Additional difficulty was that periodically the infusion of the CA was stopped, which consequently influenced the acquired T_1-weighted imaging. Moreover, this problem impaired the possibility to record the control signal from the rCA by simultaneously administering additional CA into the contralateral hemisphere. Thus a method that allows for more direct control of CA infusion would be a valuable improvement for such measurements.

Moreover, MCAo was caused remotely. Even though that procedure required a longer surgical time and a significantly more complex preparation (that already requires a highly trained person for the direct approach), it allowed obtaining valuable additional information. Namely with this approach, T_1-weighted imaging could be acquired before the triggering of cerebral ischemia and also during the reperfusion period. Thus, [Ca^{2+}] changes could be recorded from the beginning of the ischemia onset and continue monitoring for the majority of ischemia chronic phase.

Data analysis based on K-means clustering on the masked normalized T_1-weighted images displayed the co-centric pattern of the recorded signal (Figure 8).

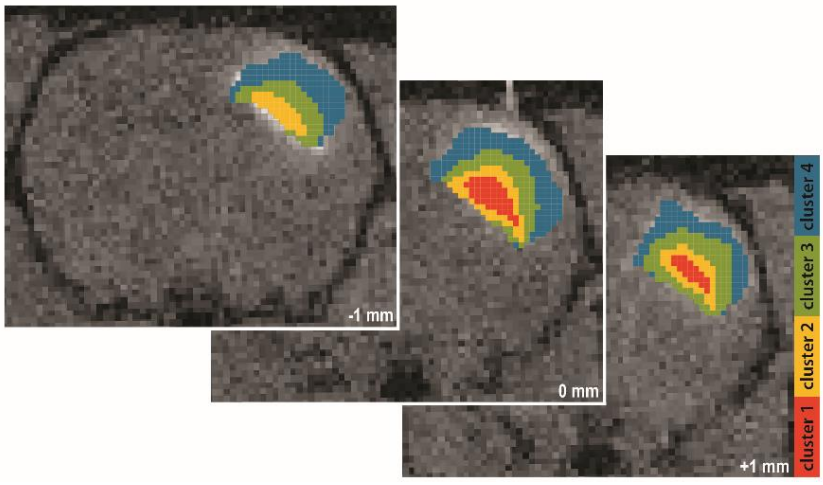

Figure 8. Cluster maps of the responsive agent **Gd_2L^1** infused in the rat brain.

Such behaviour was consistent with the expected local [CA] and its diffusion in the brain tissue. This is further confirmed with the centroids of the displayed clusters that showed higher signals on average for the ones closer to the site of CA infusion (Figure 9).

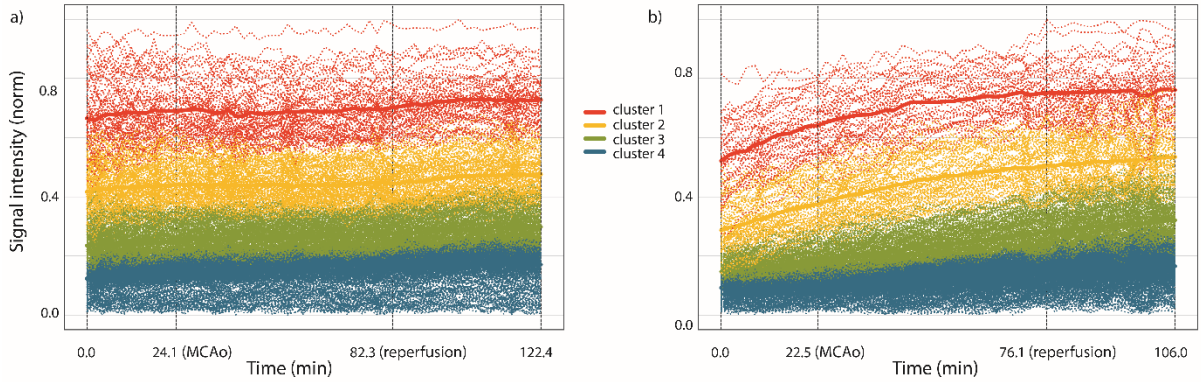

Figure 9. Centroids of corresponding cluster maps for $\mathbf{Gd_2L^1}$ (a) and $\mathbf{Gd_2L^2}$ (b) during the tMCAo experiment.

It should be mentioned that such behaviour was observed for all experiments, regardless on the number of clusters the analysis was performed with.

Upon ischemia induction and reperfusion, centroids of the clusters displayed clear and immediate changes in trends for the experiments with $\mathbf{Gd_2L^1}$. (Figure 9a). These observations were in compliance with the reported decrease of [Ca^{2+}] during ischemia and its recovery during reperfusion [25, 26]. Such alterations lead to changes in the r_1 of $\mathbf{Gd_2L^1}$ that consequently caused a reduction of signal intensity in the T_1-weighted image during the ischemia period and its recovery during reperfusion.

The responsiveness and sensitivity of $\mathbf{Gd_2L^1}$ towards Ca^{2+} was further validated with control experiments. They included tMCAo protocols with $\mathbf{Gd_2L^2}$ (Figure 9b) and also experiments with the injection of both CAs without tMCAo. All of them resulted in T_1-weighted signal intensities that were unaffected by ischemia induction, as well as reperfusion. Therefore, indicating that our method indeed could monitor early changes of cerebral ischemia, by tracking alterations in [Ca^{2+}].

Next, de-trending of the analysed signals was performed in order to emphasize the difference between the MRI responses of $\mathbf{Gd_2L^1}$ with $\mathbf{Gd_2L^1}$ during tMCAo and also the control experiments (Figure 10).

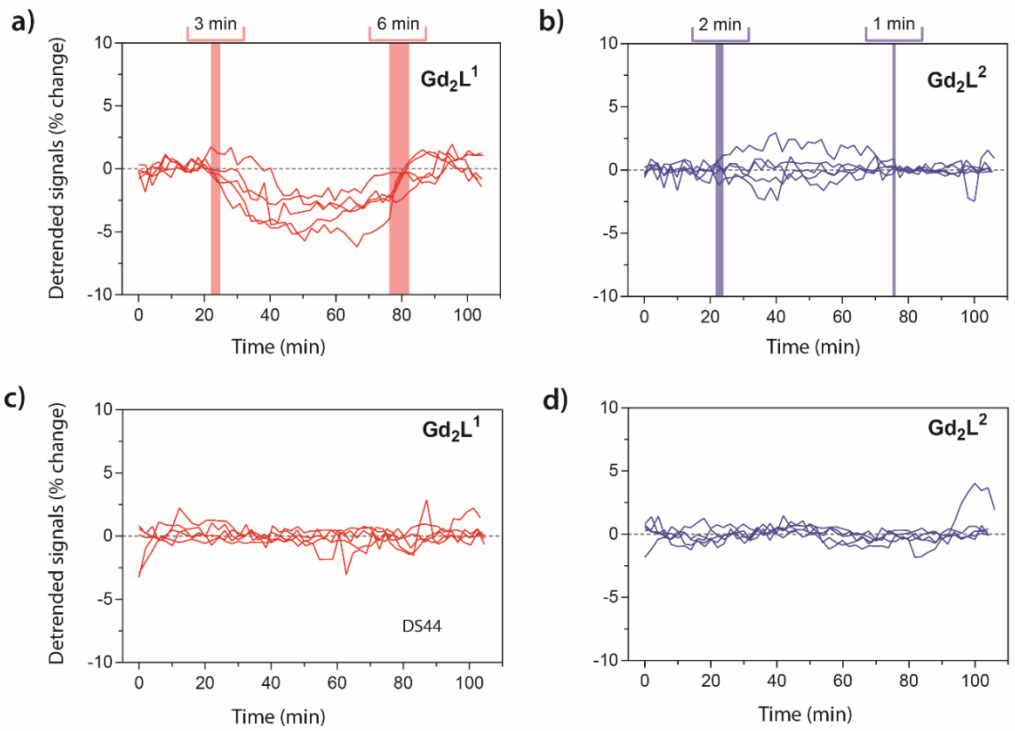

Figure 10. a) De-trended signals with (a,b) and without (c,d) tMCAo induction using **Gd_2L^1** (a,c) or **Gd_2L^2** (b,d) respectively.

Figure 10a displayed that up to a 5 % signal decline could be observed for experiments **Gd_2L^1** during the period of ischemia. On the contrary, the same experiments performed with **Gd_2L^2**, as well as control experiments with both CAs, showed no meaningful signal alterations. Lastly, mean values of the de-trended signals for all sets of experiments were presented to emphasize the suitability of this method to record ischemia onset and the further development of the ischemic injury (Figure 11).

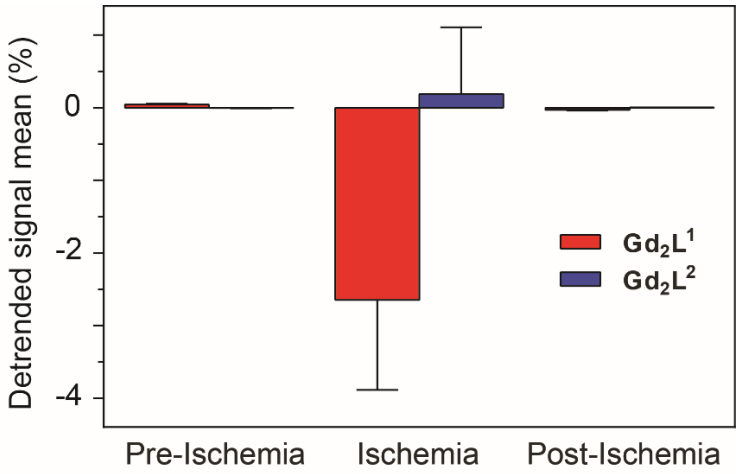

Figure 11. Average values of the de-trended signals during the recordings with **Gd_2L^1** and **Gd_2L^2** with tMCAo induction in the three segments (pre-ischemia, ischemia and reperfusion).

In specific, these signals separated by CAs and ischemia segments, showed clearly that the only significant response, a reduction in T_1-weighted signal, was observed for the tMCAo experiments with **Gd_2L^1**. These findings were also supported with the acquired DWI (Figure 12).

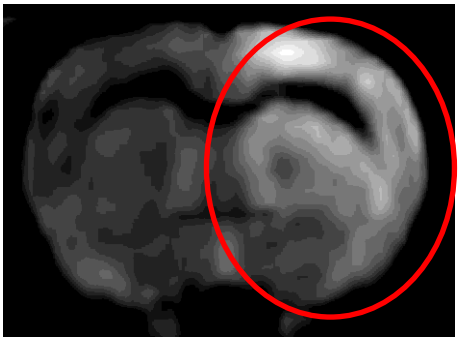

Figure 12. Confirmation of ischemia. DWI acquired after tMCAo performed on the right MCA. Ischemia affected brain area appears bright on DWI, here circled with red color.

This specific MRI method confirmed the successful induction of cerebral ischemia in the reported experiments by displaying increased signal intensity in the hemisphere of the brain where tMCAo was occluded. However it should be commented that due to the specific aim of the project, the recording of [Ca^{2+}] variations during ischemia and reperfusion, it was not possible to acquire DWI during or just after tMCAo. Instead, it must have been recorded after the reperfusion period that consequently lead to a slightly reduced hyperintensity on DWI in the brain area where tMCAo was caused. Additional techniques were tested for the confirmation of cerebral ischemia including TTC and CV staining, however the ischemic injury could not be confirmed with these methods. The reason was that all the experiments were terminal, and therefore typical period (24 hours) required for performing any of techniques could not be achieved.

3.2.4. Conclusion

The effectiveness of a novel method for accurately monitoring *in vivo* [Ca^{2+}] changes was successfully demonstrated. Most importantly, with this study a significant contribution for the early detection of cerebral ischemia was made that is of great importance for its successful treatment and recovery. Furthermore, this method could be used in much broader applications, for example in the detection and tracking of an immense number of pathophysiological processes that involve [Ca^{2+}] changes. Additionally, it could be used for the direct visualization and monitoring of neural activity with Ca^{2+}.

3.3. Paramagnetic lanthanide chelates for multicontrast MRI

3.3.1. Background/Hypotheses

In the visualization of biological processes, the combination of multiple imaging techniques provides great advantages [111, 112], although such an approach is proving to be technologically challenging [113, 114]. Thus, the design of a probe capable of generating different signals within the same imaging modality would represent a powerful tool.

MRI is a powerful imaging technique with not only unlimited tissue penetration depth and great spatio-temporal resolution but also the ability to generate diverse information by utilizing different MR contrasts including also distinct basic frequencies. With this study the potential of a multimodal CA that can be used only with MRI was presented. This was demonstrated with the acquisition of three different MRI methodologies, each of them contributing with diverse information.

3.3.2. Materials and Methods

Synthesis and ^{19}F NMR spectra were performed by Dr. Nevenka Cakić. CEST NMR experiments were recorded by Dr. Goran Angelovski. MRI phantom experiments that consisted of four samples with **GdL**, **EuL**, **TbL** (all 15 mM per complex) and water as control, placed in a syringe with saline solution were acquired by Dr. Christian Mirkes.

In vivo MRI experiments were performed on male Sprague-Dawley rats (150-250 g). ^{1}H MRI experiments were performed using isoflurane anaesthesia. For ^{19}F MRI experiments, a mixture of medetomidine and ketamine (1:10) i.p., with robinul as premedication, was used. The CA was injected intracranially into the somatosensory cortex of an animal using a precision pump. The needle was retracted stepwise 10 minutes post-injection in order to avoid leakage of the CA.
For the experiments with **GdL**, the animal was post-injection sutured and transferred into the scanner, while for *ex vivo* experiments with **EuL**, the animal was euthanized prior to transferring. In all experiments a reference tube containing a solution of NaF (192 mM) and Dotarem® (20 mM) was placed between the head of the animal and the RF coil. MRI was acquired in the time window between 0.5-3.3 hours post-injection.

With **GdL** (15 mM), ^{1}H T_1-weighted and ^{19}F MRI experiments were performed. ^{19}F MRI was acquired using the following imaging sequences: FLASH, bSSFP, 2D and 3D UTE, ZTE and CSI with the scans lasting up to 3.3 hrs.

With **EuL** (15 mM), T_1-weighted and CEST MRI experiments were recorded. CEST images were acquired using the RARE imaging sequence with a saturation pulse length and power of 5 s and 11.9 μT. The saturation offsets were screened with 5 ppm resolution at the start, and later with 1 and 0.5 ppm, respectively. The CEST image was quantified using the asymmetric magnetization transfer ratio, MTRasym = (Sb-SCEST)/Sb×100, where S represents the signal intensity of a given ROI at the resonance of CEST (SCEST) or background (Sb) signals, respectively.

3.3.3. Results and Discussion

The multicontrast of this CA was characterized with *in vitro* MRI on tube phantoms (Figure 13). MRI experiments at ^{1}H frequency showed that the highest T_1- and T_2-weighted signals were observed for **GdL**. This behaviour is expected, since Gd^{3+} has a strongest effect on water relaxation. Additionally, MRI at ^{19}F frequency showed great potential for all three complexes to be used for *in vivo* experiments and the direct determination of [CA]. Lastly, a strong CEST effect was only observed for **EuL,** having about 50 % CEST effect at 50 ppm (25 ^{0}C) [101].

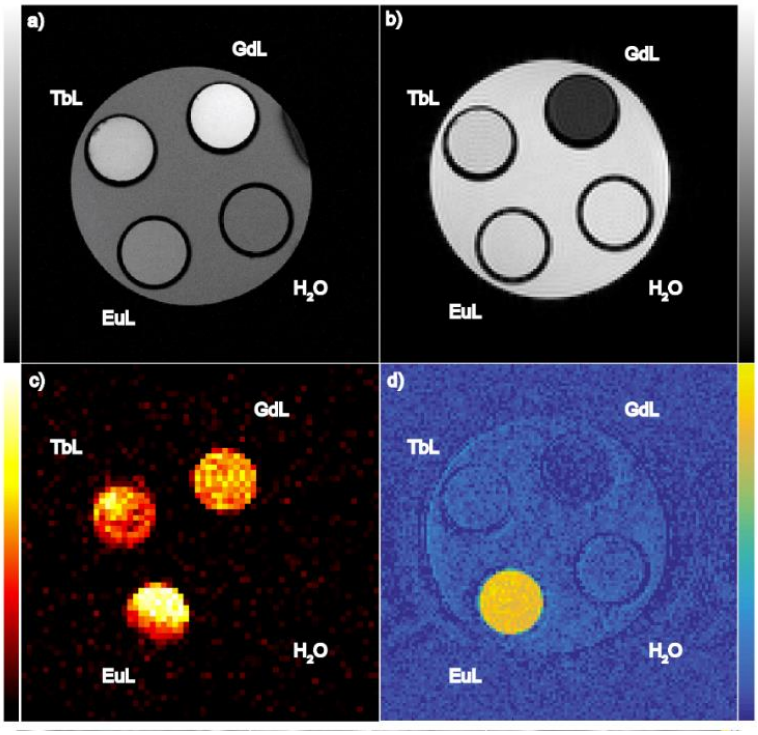

Figure 13. *In vitro* MRI on tube phantom (complex concentration 5 mM, pH 7.3, HEPES, 25 ^{0}C). a) T_1-weighted MRI b) T_2-weighted MRI c) ^{19}F MRI d) paraCEST MRI.

Intracranial injection of **GdL** resulted in the strongest T_1-weighted MRI signal (Figure 14 a). Additionally, over a period of MRI recording, it was observed that the diffusion of **GdL** was quite slow. This could indicate possible interactions with the surrounding tissue, as similar effects were previously reported for aminobisphosphonate containing contrast agents [38]. Experiments with **EuL** showed a weaker T_1-weighted MRI signal, however a very strong CEST signal (~ 10 % signal change) was observed at the frequency of the inner-sphere water molecule bound to Eu^{3+} (Figure 14b, 14c). This was a very promising result and greatly supported the usage of **EuL** as a paraCEST agent for further *in vivo* investigations.

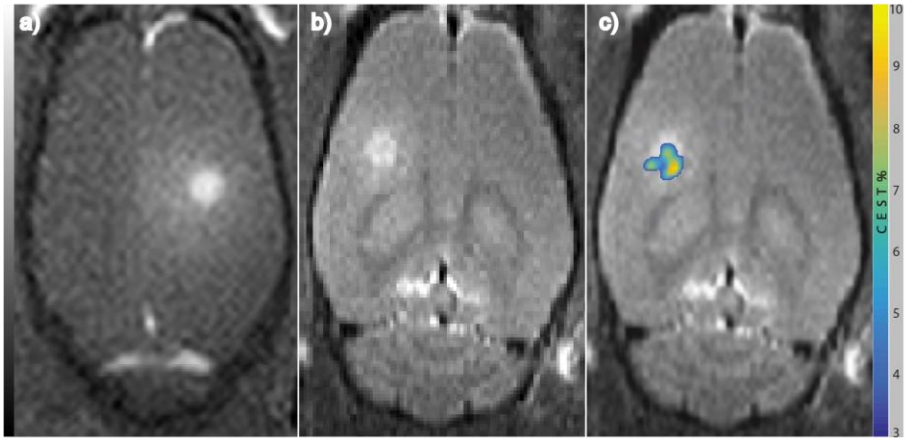

Figure 14. MRI experiments with a multicontrast agent. a) T_1-weighted MRI with **GdL** b) T_1-weighted MRI with **EuL** c) merged CEST and T_1-weighted MRI with **EuL**. Color bars show signal intensity in arbitrary units except %CEST in (c).

Regarding *in vivo* ^{19}F MRI, many imaging protocols were tested with both **GdL** and **EuL,** however no signal could be observed. As written above, these experiments were performed using non-fluorine containing anaesthesia to avoid any interference of the signal [115]. However, that consequently caused additional difficulties, since injectable anaesthesia had to be used. This implied that the depth of anaesthesia must frequently be adjusted while the animal is scanned. Nonetheless, as mentioned before, the absence of *in vivo* ^{19}F MRI signal could be explained by possible interactions of the CA with the surrounding tissue. This would consequently cause a significant reduction in the ^{19}F T_2 relaxation time, and possibly lead to a loss of signal. This hypothesis is supported with the one dimensional ^{19}F spectrum, where considerable signal broadening was observed for **GdL** injected into somatosensory cortex using intracranial injection.

3.3.4. Conclusion

The characterization of a novel MRI CA was performed. It was shown that this CA enables the generation of different MRI signals, namely T_1-weighted, CEST and ^{19}F MRI. Accordingly, by improving its design, this method could enable the precise determination of [CA] *in vivo*. Such progress would open the way to the development of a new class of rCAs that could allow for the quantification of biomarkers in clinical applications.

3.4. Paramagnetic Macrocyclic Platform for Efficient pH-Mapping via CEST MRI

3.4.1. Background/Hypotheses

Early diagnosis and treatment of diseases would not be as successful without the detection and monitoring of underlying biological processes. MRI is the leading technique that focuses on the development of such approaches. In particular, different MRI techniques were developed to detect changes of pH, as its alteration has an important role in many pathophysiological processes.

Some methods accomplished the recording of pH *in vivo* using diamagnetic and paramagnetic complexes [78, 79, 84, 116-119]. Nevertheless, an approach where the ratio of two CEST signals is used, has been shown to be advantageous, as its correlation with pH is independent of [CA]. The characteristics of a CA that can generate two CEST peaks were used and different approaches for the accurate determination of pH, independently on [CA], were developed.

3.4.2. Materials and Methods

Synthesis and characterization of the CA (**EuL**) was performed by collaborating research groups from the University of Vigo and University of Coruña in Spain. Saturation transfer NMR measurements were done using a 5 mM **EuL** sample prepared at various pH values ranging from 6.0 to 8.0. The Z-spectra were recorded using irradiation offsets in the range ± 20 ppm (0.5 ppm step), a saturation time of 5 s and set of saturation powers (2.5, 3, 5, 6, 7.5 μT). All NMR experiments were performed at two temperatures (25 and 37 ^{0}C).

MRI on tube phantoms were recorded at room temperature using six vials with the same concentration of **EuL** (3 mM) prepared in PBS at different pH values (6.0 – 8.0). Z-spectra were acquired using irradiation offsets in the range ± 20 ppm (139 points), a saturation time of 5 s and set of saturation powers (3, 4, 5, 6, 7.5 μT). Image analysis was performed with Matlab. Z-spectrum images were interpolated using splines and shifted to the center frequency to remove B_0 inhomogeneity artefacts.

In all experiments, the CEST effect was calculated using inverse asymmetry analysis applied on the normalized Z-magnetization (Equation 1).

$$MTR_{ind} = \frac{M_0}{M_{z+}} - \frac{M_0}{M_{z-}} \quad \text{Eq.1}$$

where M_0, M_{z+}, M_{z-} represent unsaturated water magnetization and magnetizations of the on-resonance recorded at frequency + Δω and the off-resonance recorded at frequency - Δω relative to bulk water.

For the generation of pH maps, the samples pH values were plotted as a function of ratio of corresponding MTR_{ind} signals. Their dependency was fitted using a first order exponential function. This function was then applied pixel-wise to the obtained MTR_{ind} ratio maps in order to obtain pH maps.

3.4.3. Results and Discussion

NMR experiments performed at different pH and saturation powers reported favourable exchange properties for both proton pools of **EuL** for pH responsiveness. With the increment of pH, exchange rates and thus their corresponding CEST signals were affected considerably. Plotting MTR_{ind} signals of both CEST peaks at different saturation powers as a function of pH resulted in a linear dependency until pH~7.4 was reached (Figure 15).

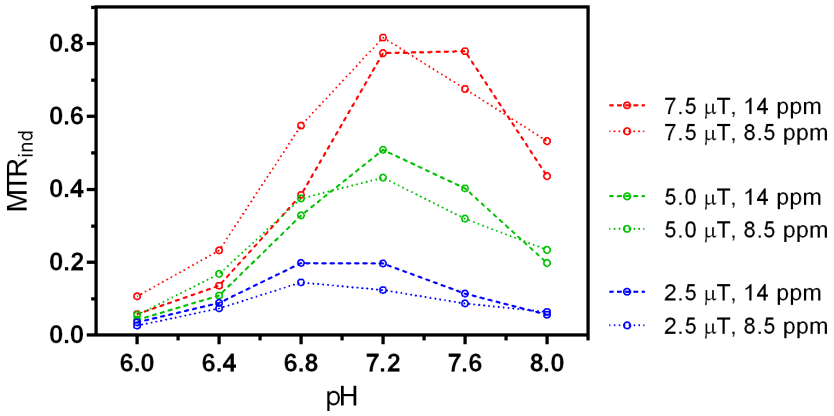

Figure 15. MTR_{ind} as a function of pH measured with NMR (5 mM **EuL** in PBS, 37 ^{0}C). Recordings were obtained using 2.5, 5, 7.5 μT and a saturation time of 5 s.

Loss of linearity for at pH values higher than 7.4 could be explained by exchange with the bulk water being too fast, resulting in a reduced MTR_{ind} signal and consequently a loss of linear pH dependency.

Additionally, different ratios of MTR_{ind} signals and presented them as a function of pH (Figure 16,17) were calculated in order to assess the possible approaches for pH sensing with this CA.

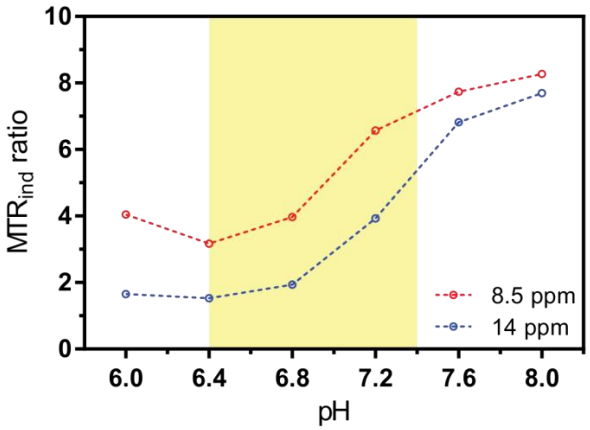

Figure 16. Single frequency ratio of MTR_{ind} signals obtained with NMR (**EuL**, 5 mM in PBS, 37 ^{0}C) at 7.5 μT and 2.5 μT for 14 ppm (blue) and 8.5 ppm (red) peaks using a saturation time of 5 s. pH range between 6.4-7.4 is highlighted with yellow color.

Single CEST peak MTR_{ind} ratios at two different saturation powers showed affirmative results for pH responsiveness. Namely, linear correlation was achieved in the physiological relevant pH range (6.4-7.4) and temperature. MTR_{ind} ratio signal changes for 8.5 ppm and 14 ppm CEST peaks recorded at 7.5 and 2.5 uT showed the best results, yielding 126 % and 251 % signal change respectively. The lower pH responsiveness obtained for the 8.5 ppm CEST peak could be explained by a twice as fast exchange with the bulk water that consequently exceeded the optimal exchange regime for obtaining the maximal CEST effect.

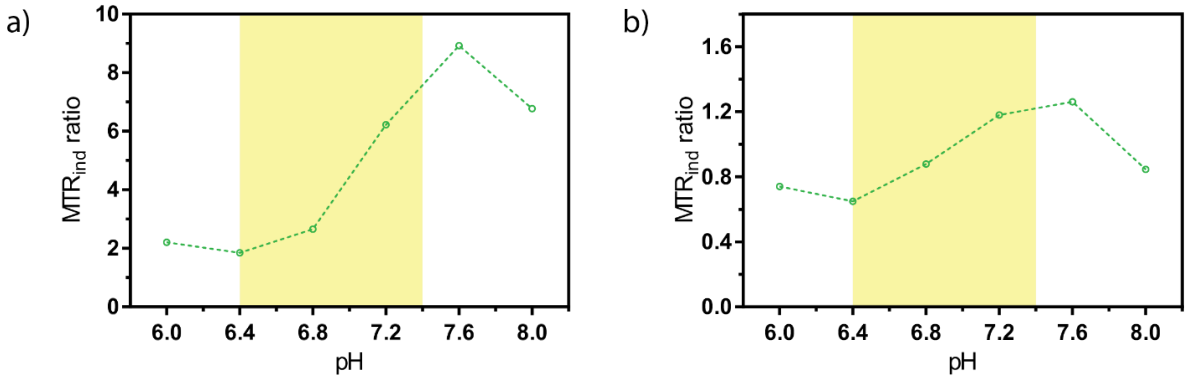

Figure 17. MTR_{ind} signal obtained with NMR (**EuL,** 5 mM in PBS, 37 ^{0}C) as a ratio of 14 ppm and 8.5 ppm CEST peaks recorded at saturation time of 5 s and a) 7.5 and 2.5 μT b) 5 μT saturation power respectively. pH range between 6.4-7.4 is highlighted with yellow color.

MTR_{ind} signal ratios that compared the two CEST signals offered another approach for pH sensing, considering they showed comparable pH responsiveness as single peaks (Figure 16). Among many tested combinations, MTR_{ind} ratios recorded at 7.5 μT and 2.5 μT (Figure 17a) or at 5 μT (Figure 17b) respectively, produced 309 % and

88 % signal change for the physiologically relevant pH range. It should be mentioned that pH sensing with such a CA could generate a much higher response in MRI signal with either approach than what could be obtained with monomeric Gd^{3+} based CAs.

Results from MRI experiments support NMR findings. Despite these recordings being done at room temperature, which lead to lower exchange rates and subsequently lower CEST signals, MTR_{ind} signals recorded in a range of saturation powers showed comparably favorable pH dependency (Figure 18).

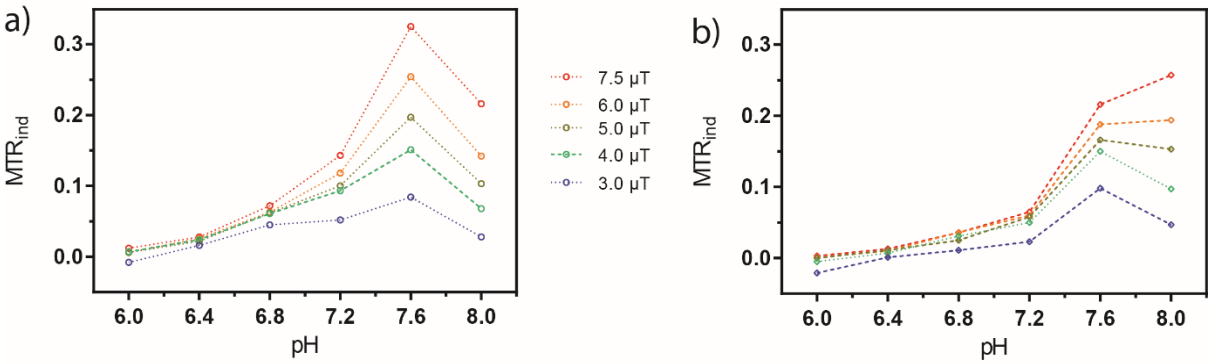

Figure 18. MTR_{ind} signals presented as a function of pH, obtained with MRI scanner (3 mM **EuL** in PBS, RT) using saturation time of 5 s and CEST frequencies at a) 9.7 ppm b) 15.3 ppm.

It should be mentioned that the lower temperature caused the extension of the pH responsive range for the 9.7 ppm CEST peak, from pH 7.4 as reported with NMR at 37^0C to pH 7.6 (Figure 18a).

A few attempts to perform MRI phantom measurements at 37 ^{0}C were also made. Initial efforts were with a custom made water circulating system in which the phantom was immersed. However, due to the thickness of the water tubing, the phantom temperature could only reach 25 ^{0}C. Nevertheless, MRI obtained with such a heating system resulted in motion artifacts due to the continuous water circulation around the phantom. Additional attempts have been made with an electrical heating system, however the acquired MRI also contained artifacts.

Nonetheless, despite the discrepancy between the temperatures of measurements performed with NMR and MRI, the corresponding pH responsiveness with MRI was obtained. Using different ratios of MTR_{ind} and pH values, pH maps with both ratiometric approaches were acquired (Figure 19).

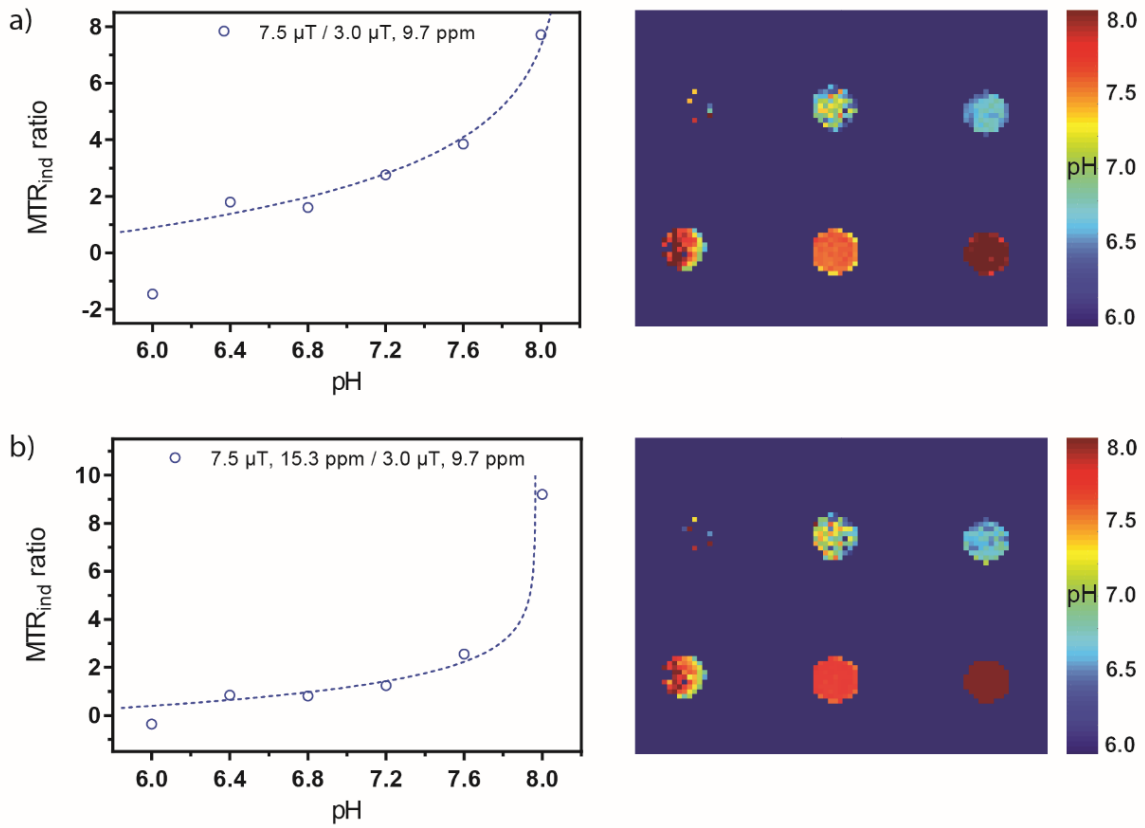

Figure 19. pH maps (right) obtained from the MTR_{ind} ratio (left) on MRI tube phantoms with **EuL** (3 mM in PBS, RT) using MTR_{ind} signals from a) 9 ppm CEST peak recorded at 7.5 and 3 µT and b) 15.3 ppm peak at 7.5 µT and 9.7 ppm peak at 3 µT. In both cases the saturation time was 5 s.

The generated pH maps (19a, 19b) showed good correlation for the majority of samples prepared at physiological relevant pH values (pH 6.0-8.0). Still, due to the low temperature, the ratio of MTR_{ind} signals at pH 6.0 were too low to obtain a clear reading of pH. However, such signals could be suppressed or filtered using MTR threshold. Nonetheless, both pH maps showed good enough coverage to be used for pH detection in solid tumors (pH 6.5-7.0) [120] or ischemia (pH 7.2-6.4) [121].

3.4.4. Conclusion

The CA that offers multiple methods for sensing pH in the physiologically relevant range was successfully characterised. This probe displays two strong CEST peaks, significantly shifted from bulk water that favourably responded to the alteration of pH. Using different approaches, either with a ratio of MTR_{ind} signals from an individual peak recorded at two different saturation powers, or as a ratio of MTR_{ind} signals from both peaks, it was possible to determine pH values independently from the [CA]. In conclusion, this paraCEST probe has a great potential for *in vivo* detection of pH.

4. Summary and Outlook

The utilization of rCAs represents a highly promising tool for the future applications of MRI in clinical practice. Considering that, still today, there are many diseases for which we still do not know the causes or cure, rCA enhanced MRI possess a great potential to tackle these problems. With rCAs we could accomplish a deeper comprehension of pathophysiological processes, and potentially help to determine the conditions under which certain diseases form. Furthermore, these new approaches could also lead to significant progress in the early monitoring, treatment and successful recovery of such pathologies that can hinder or change our lives significantly, or unfortunately terminate it. In addition to that, the tracking and real time quantification of specific biomarkers involved in neural activity, such as Ca^{2+}, could serve as a new and direct approach for the development of new fMRI techniques that would enable us to better understand the mechanisms of the brain.

Specifically, my PhD project gave new insights that could be used for the monitoring of essential biomarkers necessary for a better understanding of the pathophysiology of our organism. Within the discussed work a technique was developed that is able to detect and monitor the earliest changes that occur during cerebral ischemia. Thus, such an approach could help with timely and efficient therapy of this cerebrovascular disease that affects a significant number of people worldwide. Considering that Ca^{2+} is involved in a great number of biological processes, the application of this method could allow the direct tracking of neural activity. Moreover, with the development of a ratiometric pH mapping technique, considerable progress towards the clinical application of such a CA that could range from the characterization to the monitoring of oncological therapies was made. Furthermore, it was demonstrated that a novel approach, including dendrimeric rCAs and a non-standard imaging technique, such as bSSFP, enables rapid imaging with high SNR thus potentially allowing real-time monitoring of various pathophysiological processes. Lastly, a multicontrast MRI CA was characterized that offers the possibility of acquiring three different signals with only one imaging technique.

However, there are still many improvements to be made with preclinical *in vivo* applications of MRI rCAs, before they could be used in clinical practice. In my PhD project it was demonstrated that the reported method for the tracking of cerebral

ischemia can monitor changes in [Ca^{2+}], however these changes could not be quantified. For that reason, the development of a technique that allows for the local determination of [rCA] directly would be advantageous, without the need of internal standards or additional MRI acquisitions. If that is achieved, the local [Ca^{2+}] will be estimated in a straightforward manner. Nevertheless, once information about the local [rCA] is available, this method could be used for much broader applications, including many targeted biomarkers that yield detectable responses with MRI rCAs. Consequently, the direct quantification of essential biomarkers in real time would be accomplished.

It is also very important to mention that approaches that would enable non-invasive rCA administration are required before their clinical application could be initiated. In neuroscience this could be tested with novel techniques that enable the temporal delivery of CAs through the BBB. Once achieved, trials for the monitoring of cerebral ischemia and pH, using rCAs in humans could commence.

Nonetheless, now that the detection and tracking of essential biomarkers *in vivo* is achieved, there are many severe diseases that require urgently deeper comprehension for successful treatment and recovery. At the same time, such improvements could enhance our understanding of neurological processing. I am certain that rCA enhanced MRI would play a major role in these discoveries.

5. References

1. Brown RW, Cheng YCN, Haacke EM, Thompson MR, Venkatesan R. *Magnetic resonance imaging: Physical principles and sequence design*. John Wiley & Sons 2014.
2. Scheffler K, Hennig J. Is truefisp a gradient-echo or a spin-echo sequence? *Magnetic Resonance in Medicine*. 2003;49:395-397
3. Huang T-Y, Huang I-J, Chen C-Y, Scheffler K, Chung H-W, Cheng H-C. Are truefisp images t2/t1-weighted? *Magnetic Resonance in Medicine*. 2002;48:684-688
4. Gündüz S, Savić T, Pohmann R, Logothetis NK, Scheffler K, Angelovski G. Ratiometric method for rapid monitoring of biological processes using bioresponsive mri contrast agents. *ACS Sensors*. 2016;1:483-487
5. Wu B, Warnock G, Zaiss M, Lin C, Chen M, Zhou Z, et al. An overview of cest mri for non-mr physicists. *EJNMMI Physics*. 2016;3:19
6. Vinogradov E, Sherry AD, Lenkinski RE. Cest: From basic principles to applications, challenges and opportunities. *Journal of magnetic resonance (San Diego, Calif. : 1997)*. 2013;229:155-172
7. Woods M, Woessner DE, Sherry AD. Paramagnetic lanthanide complexes as paracest agents for medical imaging. *Chemical Society Reviews*. 2006;35:500-511
8. Ward KM, Aletras AH, Balaban RS. A new class of contrast agents for mri based on proton chemical exchange dependent saturation transfer (cest). *Journal of Magnetic Resonance*. 2000;143:79-87
9. Hingorani Dina V, Bernstein Adam S, Pagel Mark D. A review of responsive mri contrast agents: 2005–2014. *Contrast Media & Molecular Imaging*. 2014;10:245-265
10. Gustav JS, Willem JMM, Geralda AFvT, Klaas N. Mri contrast agents: Current status and future perspectives. *Anti-Cancer Agents in Medicinal Chemistry*. 2007;7:291-305
11. A. E. Merbach, Toth E. The chemistry of contrast agents in medical magnetic resonance imaging. 2004
12. Angelovski G. Heading toward macromolecular and nanosized bioresponsive mri probes for successful functional imaging. *Accounts of Chemical Research*. 2017;50:2215-2224
13. Heffern MC, Matosziuk LM, Meade TJ. Lanthanide probes for bioresponsive imaging. *Chemical Reviews*. 2014;114:4496-4539
14. Krause W, Brücher E. *Contrast agents i: Magnetic resonance imaging*. Springer; 2002.
15. Byunghee Yoo MDP. An overview of responsive mri contrast agents for molecular imaging. *Frontiers in Bioscience*. 2008;13:1733-1752
16. Shapiro MG, Westmeyer GG, Romero PA, Szablowski JO, Kuster B, Shah A, et al. Directed evolution of a magnetic resonance imaging contrast agent for noninvasive imaging of dopamine. *Nat Biotech*. 2010;28:264-270
17. Brustad EM, Lelyveld VS, Snow CD, Crook N, Jung ST, Martinez FM, et al. Structure-guided directed evolution of highly selective p450-based magnetic resonance imaging sensors for dopamine and serotonin. *Journal of Molecular Biology*. 2012;422:245-262
18. Hai A, Cai LX, Lee T, Lelyveld VS, Jasanoff A. Molecular fmri of serotonin transport. *Neuron*. 2016;92:754-765
19. M Sayre L, Perry G, Atwood C, Smith MA. *The role of metals in neurodegenerative diseases*. 2000.
20. Tu C, Osborne E, Louie A. Activatable t 1 and t 2 magnetic resonance imaging contrast agents. *Annals of Biomedical Engineering*. 2011;39:1335-1348
21. Bonnet CS, Tóth É. Mri probes for sensing biologically relevant metal ions. *Future Medicinal Chemistry*. 2010;2:367-384
22. Que EL, Chang CJ. Responsive magnetic resonance imaging contrast agents as chemical sensors for metals in biology and medicine. *Chemical Society Reviews*. 2010;39:51-60
23. Bootman Martin D, Rietdorf K, Hardy H, Dautova Y, Corps E, Pierro C, et al. Calcium signalling and regulation of cell function. *eLS*. 2012

24. Taft WC, DeLorenzo RJ. Regulation of calcium channels in brain: Implications for the clinical neurosciences. *The Yale Journal of Biology and Medicine*. 1987;60:99-106
25. Li P-A, Kristián T, Katsura K-I, Shamloo M, Siesjö BK. The influence of insulin-induced hypoglycemia on the calcium transients accompanying reversible forebrain ischemia in the rat. *Experimental Brain Research*. 1990;105:363-369
26. Siemkowicz E, Hansen AJ. Brain extracellular ion composition and eeg activity following 10 minutes ischemia in normo- and hyperglycemic rats. *Stroke*. 1981;12:236
27. Logothetis NK. What we can do and what we cannot do with fmri. *Nature*. 2008;453:869-878
28. Li W-h, Fraser SE, Meade TJ. A calcium-sensitive magnetic resonance imaging contrast agent. *Journal of the American Chemical Society*. 1999;121:1413-1414
29. Grynkiewicz G, Poenie M, Tsien RY. A new generation of ca2+ indicators with greatly improved fluorescence properties. *Journal of Biological Chemistry*. 1985;260:3440-3450
30. Tsien RY. New calcium indicators and buffers with high selectivity against magnesium and protons: Design, synthesis, and properties of prototype structures. *Biochemistry*. 1980;19:2396-2404
31. Angelovski G, Fouskova P, Mamedov I, Canals S, Toth E, Logothetis Nikos K. Smart magnetic resonance imaging agents that sense extracellular calcium fluctuations. *ChemBioChem*. 2008;9:1729-1734
32. Mishra A, Fousková P, Angelovski G, Balogh E, Mishra AK, Logothetis NK, et al. Facile synthesis and relaxation properties of novel bispolyazamacrocyclic gd3+ complexes: An attempt towards calcium-sensitive mri contrast agents. *Inorganic Chemistry*. 2008;47:1370-1381
33. Angelovski G, Gottschalk S, Milošević M, Engelmann J, Hagberg GE, Kadjane P, et al. Investigation of a calcium-responsive contrast agent in cellular model systems: Feasibility for use as a smart molecular probe in functional mri. *ACS Chem. Neurosci.* 2014;5:360-369
34. Dhingra K, Maier ME, Beyerlein M, Angelovski G, Logothetis NK. Synthesis and characterization of a smart contrast agent sensitive to calcium. *Chemical Communications*. 2008:3444-3446
35. Mamedov I, Logothetis NK, Angelovski G. Structure-related variable responses of calcium sensitive mri probes. *Organic & Biomolecular Chemistry*. 2011;9:5816-5824
36. Verma Kirti D, Forgács A, Uh H, Beyerlein M, Maier Martin E, Petoud S, et al. New calcium-selective smart contrast agents for magnetic resonance imaging. *Chemistry – A European Journal*. 2013;19:18011-18026
37. Mishra A, Logothetis Nikos K, Parker D. Critical in vitro evaluation of responsive mri contrast agents for calcium and zinc. *Chemistry – A European Journal*. 2011;17:1529-1537
38. Mamedov I, Canals S, Henig J, Beyerlein M, Murayama Y, Mayer HA, et al. In vivo characterization of a smart mri agent that displays an inverse response to calcium concentration. *ACS Chemical Neuroscience*. 2010;1:819-828
39. Henig J, Mamedov I, Fouskova P, Tóth É, Logothetis NK, Angelovski G, et al. Influence of calcium-induced aggregation on the sensitivity of aminobis(methylenephosphonate)-containing potential mri contrast agents. *Inorganic Chemistry*. 2011;50:6472-6481
40. Hagberg Gisela E, Mamedov I, Power A, Beyerlein M, Merkle H, Kiselev Valerij G, et al. Diffusion properties of conventional and calcium-sensitive mri contrast agents in the rat cerebral cortex. *Contrast Media & Molecular Imaging*. 2014;9:71-82
41. Gunduz S, Nitta N, Vibhute S, Shibata S, Mayer ME, Logothetis NK, et al. Dendrimeric calcium-responsive mri contrast agents with slow in vivo diffusion. *Chemical Communications*. 2015;51:2782-2785
42. Garello F, Vibhute S, Gündüz S, Logothetis NK, Terreno E, Angelovski G. Innovative design of ca-sensitive paramagnetic liposomes results in an unprecedented increase in longitudinal relaxivity. *Biomacromolecules*. 2016;17:1303-1311

43. Moussaron A, Vibhute S, Bianchi A, Gündüz S, Kotb S, Sancey L, et al. Ultrasmall nanoplatforms as calcium-responsive contrast agents for magnetic resonance imaging. *Small*. 2015;11:4900-4909
44. Atanasijevic T, Shusteff M, Fam P, Jasanoff A. Calcium-sensitive mri contrast agents based on superparamagnetic iron oxide nanoparticles and calmodulin. *Proceedings of the National Academy of Sciences*. 2006;103:14707-14712
45. Rodriguez E, Lelyveld VS, Atanasijevic T, Okada S, Jasanoff A. Magnetic nanosensors optimized for rapid and reversible self-assembly. *Chemical Communications*. 2014;50:3595-3598
46. Okada S, Bartelle BB, Li N, Breton-Provencher V, Lee JJ, Rodriguez E, et al. Calcium-dependent molecular fmri using a magnetic nanosensor. *Nature Nanotechnology*. 2018
47. Viswanathan S, Kovacs Z, Green KN, Ratnakar SJ, Sherry AD. Alternatives to gadolinium-based metal chelates for magnetic resonance imaging. *Chemical Reviews*. 2010;110:2960-3018
48. Longo Dario L, Dastrù W, Digilio G, Keupp J, Langereis S, Lanzardo S, et al. Iopamidol as a responsive mri-chemical exchange saturation transfer contrast agent for ph mapping of kidneys: In vivo studies in mice at 7 t. *Magnetic Resonance in Medicine*. 2010;65:202-211
49. Zhang S, Winter P, Wu K, Sherry AD. A novel europium(iii)-based mri contrast agent. *Journal of the American Chemical Society*. 2001;123:1517-1518
50. Zhang S, Merritt M, Woessner DE, Lenkinski RE, Sherry AD. Paracest agents: Modulating mri contrast via water proton exchange. *Accounts of Chemical Research*. 2003;36:783-790
51. Siriwardena-Mahanama BN, Allen MJ. Strategies for optimizing water-exchange rates of lanthanide-based contrast agents for magnetic resonance imaging. *Molecules (Basel, Switzerland)*. 2013;18:9352-9381
52. Micskei K, Helm L, Brucher E, Merbach AE. Oxygen-17 nmr study of water exchange on gadolinium polyaminopolyacetates [gd(dtpa)(h2o)]2- and [gd(dota)(h2o)]- related to nmr imaging. *Inorganic Chemistry*. 1993;32:3844-3850
53. McMahon M, Gilad, A., Bulte, J., van Zijl, P. *Chemical exchange saturation transfer imaging*. New York: Pan Stanford; 2017.
54. Aime S, Botta M, Fasano M, Paoletti S, Anelli PL, Uggeri F, et al. Nmr evidence of a long exchange lifetime for the coordinated water in ln(iii)-bis(methyl amide)-dtpa complexes (ln = gd, dy). *Inorganic Chemistry*. 1994;33:4707-4711
55. Pubanz D, Gonzalez G, Powell DH, Merbach AE. Unexpectedly large change of water exchange rate and mechanism on [ln(dtpa-bma)(h2o)] complexes along the lanthanide(iii) series. *Inorganic Chemistry*. 1995;34:4447-4453
56. Aime S, Barge A, Botta M, De Sousa Alvaro S, Parker D. Direct nmr spectroscopic observation of a lanthanide-coordinated water molecule whose exchange rate is dependent on the conformation of the complexes. *Angewandte Chemie International Edition*. 1998;37:2673-2675
57. Aime S, Barge A, Botta M, Parker D, De Sousa AS. Prototropic vs whole water exchange contributions to the solvent relaxation enhancement in the aqueous solution of a cationic gd3+ macrocyclic complex. *Journal of the American Chemical Society*. 1997;119:4767-4768
58. Zhang S, Kovacs Z, Burgess S, Aime S, Terreno E, Sherry AD. {dota-bis(amide)}lanthanide complexes: Nmr evidence for differences in water-molecule exchange rates for coordination isomers. *Chemistry – A European Journal*. 2001;7:288-296
59. Green KN, Viswanathan S, Rojas-Quijano FA, Kovacs Z, Sherry AD. Europium(iii) dota-derivatives having ketone donor pendant arms display dramatically slower water exchange. *Inorganic Chemistry*. 2011;50:1648-1655
60. Aime S, Delli Castelli D, Terreno E. Supramolecular adducts between poly-l-arginine and [tmiiidotp]: A route to sensitivity-enhanced magnetic resonance imaging–chemical

exchange saturation transfer agents. *Angewandte Chemie International Edition*. 2003;42:4527-4529
61. Pikkemaat JA, Wegh RT, Lamerichs R, van de Molengraaf RA, Langereis S, Burdinski D, et al. Dendritic paracest contrast agents for magnetic resonance imaging. *Contrast Media & Molecular Imaging*. 2007;2:229-239
62. Goffeney N, Bulte JWM, Duyn J, Bryant LH, van Zijl PCM. Sensitive nmr detection of cationic-polymer-based gene delivery systems using saturation transfer via proton exchange. *Journal of the American Chemical Society*. 2001;123:8628-8629
63. Aime S, Delli Castelli D, Terreno E. Highly sensitive mri chemical exchange saturation transfer agents using liposomes. *Angewandte Chemie International Edition*. 2005;44:5513-5515
64. Zhang S, Sherry AD. Physical characteristics of lanthanide complexes that act as magnetization transfer (mt) contrast agents. *Journal of Solid State Chemistry*. 2003;171:38-43
65. Zhang S, Wu K, Sherry AD. Unusually sharp dependence of water exchange rate versus lanthanide ionic radii for a series of tetraamide complexes. *Journal of the American Chemical Society*. 2002;124:4226-4227
66. Helm L, Merbach AE. Inorganic and bioinorganic solvent exchange mechanisms. *Chemical Reviews*. 2005;105:1923-1960
67. Helm L, Merbach AE. Water exchange on metal ions: Experiments and simulations. *Coordination Chemistry Reviews*. 1999;187:151-181
68. Aime S, Carrera C, Delli Castelli D, Geninatti Crich S, Terreno E. Tunable imaging of cells labeled with mri-paracest agents. *Angewandte Chemie International Edition*. 2005;44:1813-1815
69. Sinharay S, Pagel MD. Advances in magnetic resonance imaging contrast agents for biomarker detection. *Annual Review of Analytical Chemistry*. 2016;9:95-115
70. Wu Y, Carney CE, Denton M, Hart E, Zhao P, Streblow DN, et al. Polymeric paracest mri contrast agents as potential reporters for gene therapy. *Organic & Biomolecular Chemistry*. 2010;8:5333-5338
71. Högemann D, Basilion JP. "Seeing inside the body": Mr imaging of gene expression. *European Journal of Nuclear Medicine and Molecular Imaging*. 2002;29:400-408
72. Gillies RJ, Raghunand N, Garcia-Martin ML, Gatenby RA. Ph imaging. *IEEE Engineering in Medicine and Biology Magazine*. 2004;23:57-64
73. Zhang S, Wu K, Sherry AD. A novel ph-sensitive mri contrast agent. *Angewandte Chemie International Edition*. 1999;38:3192-3194
74. Ward KM, Balaban RS. Determination of ph using water protons and chemical exchange dependent saturation transfer (cest). *Magnetic Resonance in Medicine*. 2000;44:799-802
75. Aime S, Barge A, Delli Castelli D, Fedeli F, Mortillaro A, Nielsen Flemming U, et al. Paramagnetic lanthanide(iii) complexes as ph-sensitive chemical exchange saturation transfer (cest) contrast agents for mri applications. *Magnetic Resonance in Medicine*. 2002;47:639-648
76. Aime S, Delli Castelli D, Terreno E. Novel ph-reporter mri contrast agents. *Angewandte Chemie International Edition*. 2002;41:4334-4336
77. Terreno E, Castelli DD, Cravotto G, Milone L, Aime S. Ln(iii)-dotamgly complexes: A versatile series to assess the determinants of the efficacy of paramagnetic chemical exchange saturation transfer agents for magnetic resonance imaging applications. *Investigative Radiology*. 2004;39:235-243
78. Delli Castelli D, Terreno E, Aime S. Ybiii-hpdo3a: A dual ph- and temperature-responsive cest agent. *Angewandte Chemie International Edition*. 2011;50:1798-1800
79. Dorazio SJ, Olatunde AO, Spernyak JA, Morrow JR. Cocest: Cobalt(ii) amide-appended paracest mri contrast agents. *Chemical Communications*. 2013;49:10025-10027
80. Liu G, Li Y, Sheth VR, Pagel MD. Imaging in vivo extracellular ph with a single paramagnetic chemical exchange saturation transfer magnetic resonance imaging contrast agent. *Mol Imaging*. 2012;11:47-57

81. Sheth Vipul R, Li Y, Chen Liu Q, Howison Christine M, Flask Chris A, Pagel Mark D. Measuring in vivo tumor phe with cest-fisp mri. *Magnetic Resonance in Medicine*. 2011;67:760-768
82. Sheth Vipul R, Liu G, Li Y, Pagel Mark D. Improved ph measurements with a single paracest mri contrast agent. *Contrast Media & Molecular Imaging*. 2012;7:26-34
83. McVicar N, Li Alex X, Suchý M, Hudson Robert HE, Menon Ravi S, Bartha R. Simultaneous in vivo ph and temperature mapping using a paracest-mri contrast agent. *Magnetic Resonance in Medicine*. 2012;70:1016-1025
84. Wu Y, Soesbe TC, Kiefer GE, Zhao P, Sherry AD. A responsive europium(iii) chelate that provides a direct readout of ph by mri. *Journal of the American Chemical Society*. 2010;132:14002-14003
85. Tsou Y-H, Zhang X-Q, Zhu H, Syed S, Xu X. Drug delivery to the brain across the blood–brain barrier using nanomaterials. *Small*. 2017;13:1701921
86. Nicholson C, Syková E. Extracellular space structure revealed by diffusion analysis. *Trends in Neurosciences*. 1998;21:207-215
87. Caravan P. Strategies for increasing the sensitivity of gadolinium based mri contrast agents. *Chemical Society Reviews*. 2006;35:512-523
88. Grad J, Bryant RG. Nuclear magnetic cross-relaxation spectroscopy. *Journal of Magnetic Resonance (1969)*. 1990;90:1-8
89. Angelovski G. Biosensitive kontrastmittel für die magnetresonanztomographie – was wir mit ihnen wirklich tun können. *Angewandte Chemie*. 2016;128:7152-7161
90. Ekanger LA, Allen MJ. Overcoming the concentration-dependence of responsive probes for magnetic resonance imaging. *Metallomics*. 2015
91. de Rochefort L, Nguyen T, Brown R, Spincemaille P, Choi G, Weinsaft J, et al. In vivo quantification of contrast agent concentration using the induced magnetic field for time-resolved arterial input function measurement with mri. *Medical Physics*. 2008;35:5328-5339
92. Bokacheva L, Rusinek H, Chen Q, Oesingmann N, Prince C, Kaur M, et al. Quantitative determination of gd-dtpa concentration in t1-weighted mr renography studies. *Magnetic Resonance in Medicine*. 2007;57:1012-1018
93. Herrmann K, Johansen ML, Craig SE, Vincent J, Howell M, Gao Y, et al. Molecular imaging of tumors using a quantitative t(1) mapping technique via magnetic resonance imaging. *Diagnostics*. 2015;5:318-332
94. Johansen ML, Gao Y, Hutnick MA, Craig SEL, Pokorski JK, Flask CA, et al. Quantitative molecular imaging with a single gd-based contrast agent reveals specific tumor binding and retention in vivo. *Analytical Chemistry*. 2017;89:5932-5939
95. Patil V, Johnson G, Jensen JH. Robust quantification of contrast agent (ca) concentration with magnetic field correlation (mfc) imaging. *Magnetic resonance in medicine : official journal of the Society of Magnetic Resonance in Medicine / Society of Magnetic Resonance in Medicine*. 2009;62:1002-1006
96. Bhuiyan M, P Aryal M, Janic B, Karki K, Nadimpalli R, Ewing J, et al. *Concentration‐independent mri of ph with a dendrimer‐based ph‐responsive nanoprobe*. 2015.
97. Aime S, Fedeli F, Sanino A, Terreno E. A r2/r1 ratiometric procedure for a concentration-independent, ph-responsive, gd(iii)-based mri agent. *Journal of the American Chemical Society*. 2006;128:11326-11327
98. Catanzaro V, Gringeri CV, Menchise V, Padovan S, Boffa C, Dastrù W, et al. A r2p/r1p ratiometric procedure to assess matrix metalloproteinase-2 activity by magnetic resonance imaging. *Angewandte Chemie International Edition*. 2013;52:3926-3930
99. Gianolio E, Napolitano R, Fedeli F, Arena F, Aime S. Poly-β-cyclodextrin based platform for ph mapping via a ratiometric 19f/1h mri method. *Chemical Communications*. 2009:6044-6046
100. Ekanger LA, Ali MM, Allen MJ. Oxidation-responsive eu2+/3+-liposomal contrast agent for dual-mode magnetic resonance imaging. *Chemical Communications*. 2014;50:14835-14838

101. Cakić N, Savić T, Stricker-Shaver J, Truffault V, Platas-Iglesias C, Mirkes C, et al. Paramagnetic lanthanide chelates for multicontrast mri. *Chem. Commun.* 2016;52:9224-9227
102. Nwe K, Bryant LH, Brechbiel MW. Poly(amidoamine) dendrimer based mri contrast agents exhibiting enhanced relaxivities derived via metal pre-ligation techniques. *Bioconjugate chemistry*. 2010;21:1014-1017
103. The world health report: 2002: Reducing risks, promoting healthy life. *World Health Organization*. 2002
104. Feigin VL, Lawes CMM, Bennett DA, Anderson CS. Stroke epidemiology: A review of population-based studies of incidence, prevalence, and case-fatality in the late 20th century. *The Lancet Neurology*. 2003;2:43-53
105. Dirnagl U, Iadecola C, Moskowitz MA. Pathobiology of ischaemic stroke: An integrated view. *Trends in Neurosciences*. 1999;22:391-397
106. Coakley FV, Glenn OA, Qayyum A, Barkovich AJ, Goldstein R, Filly RA. Fetal mri: A developing technique for the developing patient. *American Journal of Roentgenology*. 2004;182:243-252
107. Schaefer Pamela W, Barak Elizabeth R, Kamalian S, Gharai Leila R, Schwamm L, Gonzalez Ramon G, et al. Quantitative assessment of core/penumbra mismatch in acute stroke. *Stroke*. 2008;39:2986-2992
108. Moustafa RR, Baron JC. Pathophysiology of ischaemic stroke: Insights from imaging, and implications for therapy and drug discovery. *British Journal of Pharmacology*. 2008;153:S44-S54
109. J. Bogousslavsky GV, F. Regli. The lausanne stroke registry - analysis of 1,000 consecutive patients with first stroke. *Stroke*. 1988;19:1083-1092
110. Olsen TS, Skriver EB, Herning M. Cause of cerebral infarction in the carotid territory. Its relation to the size and the location of the infarct and to the underlying vascular lesion. *Stroke*. 1985;16:459-466
111. Weissleder R, Pittet MJ. Imaging in the era of molecular oncology. *Nature*. 2008;452:580
112. Kobayashi H, Longmire MR, Ogawa M, Choyke PL. Rational chemical design of the next generation of molecular imaging probes based on physics and biology: Mixing modalities, colors and signals. *Chemical Society Reviews*. 2011;40:4626-4648
113. Cherry SR. Multimodality in vivo imaging systems: Twice the power or double the trouble? *Annual Review of Biomedical Engineering*. 2006;8:35-62
114. Louie AY. Multimodality imaging probes: Design and challenges. *Chem. Rev.* 2010;110:3146-3195
115. Leif Schröder CF. In vivo nmr imaging: Methods and protocols. *Methods Mol Biol*. 2011;771:1-753
116. Hingorani DV, Bernstein AS, Pagel MD. A review of responsive mri contrast agents: 2005–2014. *Contrast Media Mol. Imaging*. 2015;10:245-265
117. Chen LQ, Howison CM, Jeffery JJ, Robey IF, Kuo PH, Pagel MD. Evaluations of extracellular ph within in vivo tumors using acidocest mri. *Magnetic Resonance in Medicine*. 2014;72:1408-1417
118. Longo DL, Sun PZ, Consolino L, Michelotti FC, Uggeri F, Aime S. A general mri-cest ratiometric approach for ph imaging: Demonstration of in vivo ph mapping with iobitridol. *Journal of the American Chemical Society*. 2014;136:14333-14336
119. Thorarinsdottir AE, Du K, Collins JHP, Harris TD. Ratiometric ph imaging with a coii2 mri probe via cest effects of opposing ph dependences. *Journal of the American Chemical Society*. 2017;139:15836-15847
120. Helmlinger G, Yuan F, Dellian M, Jain RK. Interstitial ph and po2 gradients in solid tumors in vivo: High-resolution measurements reveal a lack of correlation. *Nature Medicine*. 1997;3:177
121. Nedergaard M, Kraig RP, Tanabe J, Pulsinelli WA. Dynamics of interstitial and intracellular ph in evolving brain infarct. *The American journal of physiology*. 1991;260:R581-R588

Appended papers

Chapter 3.1.

Gündüz, S.; Savić, T.; Pohmann, R.; Logothetis, N. K.; Scheffler, K.; Angelovski, G., Ratiometric Method for Rapid Monitoring of Biological Processes Using Bioresponsive MRI Contrast Agents. *ACS Sensors* **2016,** *1* (5), 483-487.

Chapter 3.2.

Savić, T.; Gambino, G.; Bokharaie, V.; Noori., H.; Logothetis, N. K.; Angelovski, G., Early detection and monitoring of brain ischemia using calcium-responsive MRI probes. *Submitted.*

Chapter 3.3.

Cakić, N.; Savić, T.; Stricker-Shaver, J.; Truffault, V.; Platas-Iglesias, C.; Mirkes, C.; Pohmann, R.; Scheffler, K.; Angelovski, G., Paramagnetic lanthanide chelates for multicontrast MRI. *Chemical Communications* **2016,** *52* (59), 9224-9227.

Chapter 3.4.

Savić, T.; Valencia, L.; Pérez-Lourido, P.; Esteban-Gómez, D.; Zaiss, M.; Platas-Iglesias, C.; Angelovski, G., Paramagnetic Macrocyclic Platform for Efficient pH Mapping via CEST MRI. *In preparation.*

ACS SENSORS

Letter

pubs.acs.org/acssensors

Ratiometric Method for Rapid Monitoring of Biological Processes Using Bioresponsive MRI Contrast Agents

Serhat Gündüz,[†,#] Tanja Savić,[†,#] Rolf Pohmann,[‡] Nikos K. Logothetis,[§,∥] Klaus Scheffler,[‡,⊥] and Goran Angelovski*[,†]

[†]MR Neuroimaging Agents, [‡]High-Field Magnetic Resonance, and [§]Physiology of Cognitive Processes, Max Planck Institute for Biological Cybernetics, 72076 Tübingen, Germany

[∥]Department of Imaging Science and Biomedical Engineering, University of Manchester, Manchester M13 9PT, United Kingdom

[⊥]Department for Biomedical Magnetic Resonance, University of Tübingen, 72076 Tübingen, Germany

Supporting Information

ABSTRACT: Bioresponsive magnetic resonance imaging (MRI) contrast agents hold great potential for noninvasive tracking of essential biological processes. Consequently, a number of MR sensors for several imaging protocols have been developed, attempting to produce the maximal signal difference for a given event. Here we introduce an approach which could substantially improve the detection of physiological events with fast kinetics. We developed a nanosized, calcium-sensitive dendrimeric probe that changes longitudinal and transverse relaxation times with different magnitudes. The change in their ratio is rapidly recorded by means of a balanced steady-state free precession (bSSFP) imaging protocol. The employed methodology results in an almost four times greater signal gain per unit of time as compared to conventional T_1-weighted imaging with small sized contrast agents. Furthermore, it is suitable for high resolution functional MRI at high magnetic fields. This methodology could evolve into a valuable tool for rapid monitoring of various biological events.

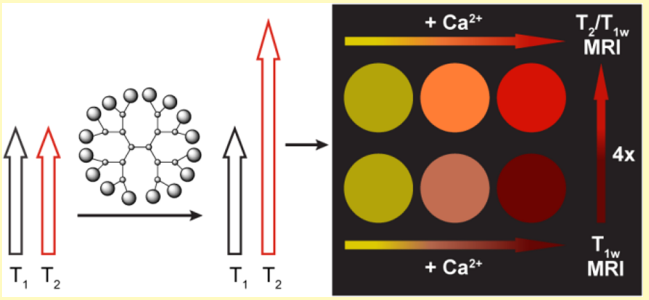

KEYWORDS: *bioresponsive agents, calcium, dendrimers, magnetic resonance imaging*

The ability to monitor biological processes in a functional manner is of crucial importance for all imaging techniques. In particular, magnetic resonance imaging (MRI) is the preferred method due to its high spatial and temporal resolution, and the possibility to study tissue at any depth. Bioresponsive MRI contrast agents further improve the potential of this methodology to follow biological functions by altering the signal as a consequence of specific changes in their microenvironment.[1,2] Thus, far, numerous molecular sensors of this kind have been developed with the capability to affect T_1 or T_2 relaxation times,[3−7] the chemical exchange saturation transfer (CEST) effect,[8,9] or particular resonance frequencies of the investigated probe.[10−12] Nonetheless, several issues still present formidable obstacles for optimal utilization of bioresponsive MRI probes. For example, the amplitude of the MR signal changes under the investigated physiological conditions must be sufficient to be detectable; on the other hand, the altered signal often cannot be unambiguously correlated with the desired stimulus, because it may also be caused by changes in concentration of the probe due to its diffusion. Additionally, most conventional pulse sequences used for T_1, T_2, or CEST agents require acquisition times on the scale of minutes, preventing observation of fast and dynamic processes.

Efforts to overcome these problems are ongoing. A promising line of research is the development of concentration-independent probes.[13] Notably, ratiometric methods dominate this approach because the dependence of two relaxation rates, CEST effects or chemical shifts on a particular event or target concentration negates the need to know or consider the concentration of the bioresponsive contrast agent.[14−17] To date, several studies took advantage of the longitudinal and transverse relaxation rates ratio (R_1/R_2) to prepare a concentration-independent probe, however only suitable for quantitative pH imaging.[14,18,19]

Here, we introduce a novel way to monitor biological processes in a dynamic manner. We employ changes in the ratio of R_1 and R_2 caused by concentration changes of the target, and translate this rapidly into MR contrast images using balanced steady-state free precession (bSSFP) imaging. We demonstrate the principle using a dendrimeric MRI contrast agent whose T_1 (R_1) and T_2 (R_2) are affected with different magnitudes as functions of calcium concentration. In addition, the advantages of this method relative to conventional

Received: January 7, 2016
Accepted: March 2, 2016
Published: March 2, 2016

DOI: 10.1021/acssensors.6b00011
ACS Sens. 2016, 1, 483−487

exploitation of T_1 or T_2 effects, or in more complex environments, are shown. This method has great potential for easy application to other approaches using bioresponsive agents and could resolve many existing problems in functional MRI.

Balanced SSFP is a combination of gradient-echo and spin−echo sequences characterized by very interesting and unique features. Namely, its contrast is approximately T_2/T_1-weighted (it decreases with a reduction in the T_2/T_1 ratio), meaning that shortened or prolonged relaxation times are not of crucial importance to produce the signal changes, but rather the ratio of these factors. Furthermore, it produces the highest signal-to-noise ratio (SNR) per unit time of all imaging sequences.[20] It is well suited to imaging dynamic processes at high temporal resolution and may be the best choice for detecting the activity of bioresponsive agents.

To explore the potential of this approach, we considered adjusting our calcium-sensitive, "smart" contrast agents (SCAs) and optimizing them for this particular purpose. It is well-established that these molecular sensors change their relaxivity due to alteration of the hydration number, whereas approaches to modify the rotational correlation time are slowly being abandoned because they are effective only at low magnetic fields.[21] However, since low molecular weight paramagnetic agents change the T_1 and T_2 relaxation times to roughly the same extent,[21] we sought to generate an effect in addition to altered hydration, that could be only achieved with the nanosized agents. This effect would mainly influence T_2 due to the agent's size, thus changing the T_1/T_2 ratio and could possibly be exploited for applications at high magnetic fields. Hence, we coupled our monomeric SCA (MSCA) to a dendrimer using recently established procedures, resulting in a nanosized SCA, termed DSCA (Scheme 1).[22] The effect of this macromolecule on T_2 time of protons was predicted to be markedly different due to its size, and should rise with increasing field strength.[23] Its interaction with Ca^{2+} will further affect the size of the system or the flexibility of the calcium-chelating part, and consequently the local rotation of the GdDO3A unit (Figure 1).[24,25] The addition of Ca^{2+} will finally result in a common T_1 effect due to the increase in inner-sphere hydration, while the T_2 effect will be more pronounced than for small size SCAs.

Scheme 1. Monomeric (MSCA) and Dendrimeric (DSCA) Bioresponsive Agents Studied in the Work Presented Here, and the Synthetic Route to DSCA[a]

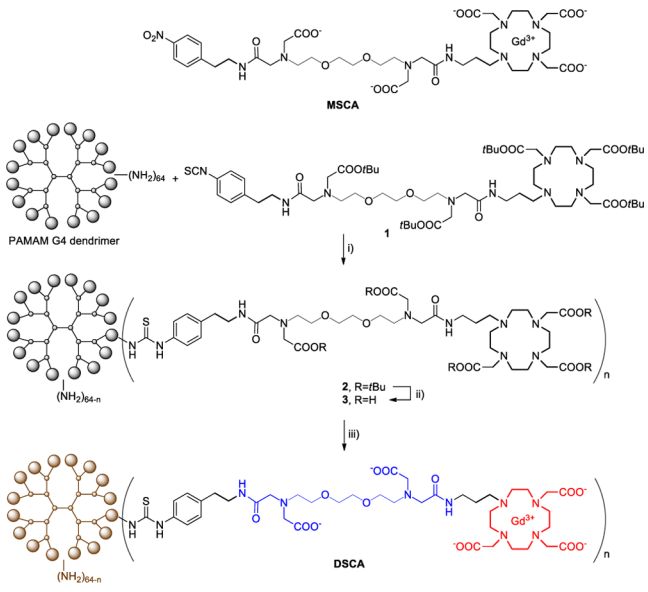

[a]Reagents and conditions: (i) Et_3N, DMF, 45 °C; (ii) formic acid, 60 °C; (iii) $GdCl_3{\cdot}6H_2O$, NaOH, then EDTA, RT.

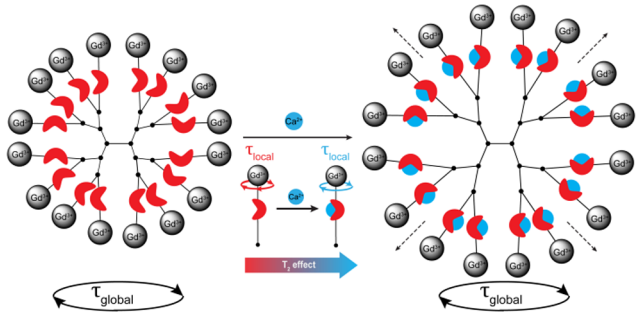

Figure 1. Cartoon image presenting the DSCA complexing with Ca^{2+}, and the effect of this interaction on global and local Gd^{3+} rotation (elliptic arrows), and the size of DSCA (dashed arrows).

DSCA was prepared from a generation 4 (G4) poly(amidoamine) (PAMAM) dendrimer with a cystamine core which allows further synthetic modifications via the sulfhydryl formed after potential reduction of cystamine.[26] The anticipated T_2 effect likely increases with a higher dendrimer generation; additionally, it will result in even slower in vivo diffusion and a stable MRI signal.[22] The synthesis was performed by coupling an amine-reactive SCA derived from the precursor of MSCA to the G4 dendrimer to give DSCA (Scheme 1). The calculated masses correspond to the average of 40 monomeric Gd^{3+} chelated units per dendrimer molecule, which indicates >60% conversion of 64 amino surface groups into the thiourea product with the NCS-derived monomeric ligand unit.

Relaxometric titrations with Ca^{2+} were performed at 7 T (300 MHz) for DSCA and results were compared with those obtained for MSCA. Identical concentrations of DSCA and MSCA (3 mM Gd^{3+}) where prepared, T_1 and T_2 relaxation times were measured upon addition of Ca^{2+}, and respective relaxivity values were calculated. As expected, the longitudinal r_1 relaxivities increased by about 70 and 130% for DSCA and MSCA, respectively, which is in line with previous observations on smaller G0 dendrimers (Figure 2A,B).[22] However, a significant change in r_2 relaxivity (360% increase) was obtained for DSCA only, while the r_2 relaxivity for MSCA increased to almost same extent as the increase in r_1 (we note that absolute r_2 values were always ∼30% higher than respective r_1 for MSCA). When these effects are combined and compared (Figure 2C and Figure S1 in the Supporting Information), one concludes that incorporation of monomeric SCA units in dendrimers results in (a) smaller increase of r_1 for DSCA, this effect is not preferred for functional T_1-weighted (T_{1w}) imaging; (b) much greater increase of r_2 for DSCA, this effect could be useful for functional T_2-weighted (T_{2w}) imaging (despite the signal loss and potentially longer acquisition times); (c) a dramatic change in the R_2/R_1 ratio for DSCA as a function of Ca^{2+} concentration, which is perfectly suitable for functional approaches using bSSFP techniques. In fact, the R_2/R_1 ratio for MSCA appears to be insensitive to the addition of Ca^{2+}, hence MSCA is not suitable for use via the same imaging approach.

DOI: 10.1021/acssensors.6b00011
ACS Sens. 2016, 1, 483−487

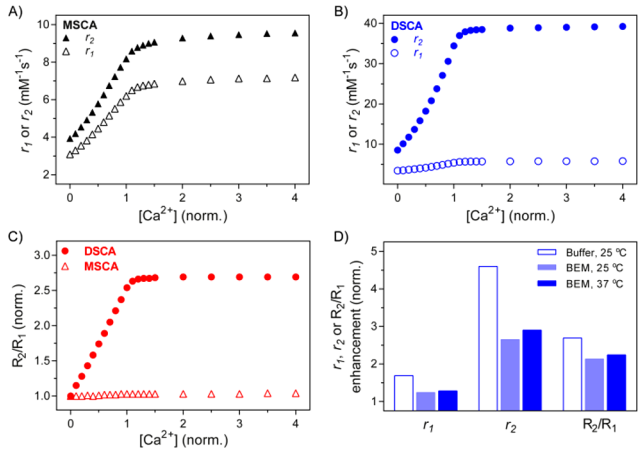

Figure 2. Effect of Ca^{2+} on a ratio of longitudinal and transverse relaxivities at 7 T (pH 7.4). Increase of the r_1 and r_2 for MSCA (A) and DSCA (B) upon saturation with Ca^{2+} (HEPES), or its effect on the R_2/R_1 ratio on MSCA and DSCA, respectively (C). [Ca^{2+}] was normalized with concentration of Gd^{3+} (3 mM). The R_2/R_1 plots show normalized values where the final value (at Ca^{2+} saturation) is divided by the initial value (in absence of Ca^{2+}). (D) Comparison of r_1, r_2, and R_2/R_1 ratio changes for DSCA in buffer (HEPES) or BEM at different temperatures at 7 T ([Gd^{3+}] = 3 mM, pH 7.4). The plots show normalized values where the final r_1, r_2, or R_2/R_1 ratio value (at Ca^{2+} saturation) is divided by the respective initial value (in absence of Ca^{2+}).

The effect observed for DSCA was assessed further for its practicability. The titrations repeated at lower concentrations of Gd^{3+} showed that the increase in the R_2/R_1 ratio is related to the amount of Gd^{3+} (Figure S2 in the Supporting Information). This is expected because the measured T_1 and T_2 values are the sum of paramagnetic and diamagnetic contributions.[27] Consequently, the influence of the paramagnetic component is weaker at lower concentrations of the responsive paramagnetic complex, but the R_2/R_1 ratio is still >2 in the presence of 1 mM Gd^{3+}. This also suggests that the method is not independent of the probe concentration; nevertheless the R_2/R_1 ratio changes are still prominent and can be used even in submillimolar Gd^{3+} concentrations. For these reasons, the method would possibly prevent straightforward quantitative mapping of extracellular Ca^{2+} ([Ca^{2+}]$_e$ ∼ 1−2 mM in brain[28]), but could robustly report on changes in the [Ca^{2+}]$_e$ during the intense neuronal activity (∼1.2 to 0.8 mM),[28] given the high SNR and extremely fast acquisition times of the bSSFP methodology (see below).

On the other hand, the negative influence of anions on this effect is not as high as might have been anticipated; namely, it is known that DO3A-based systems tend to form ternary complexes with bicarbonates, which can reduce their r_1 relaxivity.[29] Here, we repeated titrations in the brain extracellular model (BEM), using medium which resembles brain extracellular fluid, at two different temperatures (Figure 2D). Interestingly, while the total increase in r_1 was below 30%, r_2 increases by more than 160% at both temperatures so that the increase of the R_2/R_1 ratio is still over 100% upon saturation with Ca^{2+} at studied Gd^{3+} concentration (3 mM). This finding is extremely promising, suggesting that this ratiometric approach almost compensates for the undesired effect of endogenous anions on the performance of the SCA.

The results described above clearly indicated the crucial importance of the size of the investigated SCA. To probe this, we investigated the diffusion characteristics of both SCAs by means of dynamic light scattering (DLS) and/or NMR spectroscopy. Experiments were performed on the respective Eu^{3+} analogues, due to the large broadening effect of Gd^{3+} on the NMR signals. Measurements were carried out on identical concentrations of Eu^{3+} complexes, in the presence or absence of 2 equiv of Ca^{2+} (Table 1).

Table 1. Diffusion Coefficients and Sizes Obtained for Eu^{3+} Complexes of DSCA and MSCA

	diffusion coefficient (10^{-11} m^2 s^{-1})		diameter (nm)	
	no Ca^{2+}	+Ca^{2+} (2 equiv)	no Ca^{2+}	+Ca^{2+} (2 equiv)
DSCA	9.2 ± 0.9[a]	6.0 ± 0.2[a]	5.4 ± 0.5[a]	8.3 ± 0.3[a]
	8.2 ± 0.7[b]	7.3 ± 0.2[b]		
MSCA	32.0 ± 0.5[b]	28.3 ± 0.7[b]	1.5 ± 0.1[b]	1.7 ± 0.1[b]

[a]DLS measurement. [b]NMR measurement.

DLS experiments were performed for DSCA only because the size of MSCA is below the DLS measurement limit. The initial diameter of 5.4 ± 0.5 nm in the absence of Ca^{2+} was obtained, in good agreement with previously reported conjugates of this kind with G4 generation PAMAM dendrimers.[30] Upon addition of 2 equiv of Ca^{2+}, the diameter increased to 8.3 ± 0.3 nm, which clearly explains the observed r_2 behavior of DSCA and its dramatic increase with change in size and diffusion.[23] Comparable experiments were also repeated with NMR spectroscopy. Due to the variable number of monomeric units coupled to the dendrimeric core, the dispersed size distribution of DSCA yielded an average diffusion coefficient while analysis with NMR was approximated for monodiffusional systems. Even though the absolute numbers for the obtained diffusion coefficient are uncertain, the results showed the same tendency where the addition of Ca^{2+} to DSCA reduces its diffusion. On the other hand, the NMR experiments with MSCA resulted in diffusion coefficients and sizes which match those obtained for similar types of compounds.[31] Again, the addition of Ca^{2+} reduced the diffusion coefficient of the SCA, this time insufficiently to induce any dramatic changes in r_2 on the already-small SCA. Nevertheless, the interaction of both DSCA and MSCA with Ca^{2+} points toward induction of intramolecular conformational changes which make this Ca-DSCA/Ca-MSCA complex more rigid, causing the change in size and diffusion which affects the r_2 of the system, especially the DSCA.

Lastly, to prove the efficiency of DSCA for dynamic investigations in MRI, a study on tube phantoms was carried out. A series of buffered solutions with DSCA and MSCA (both 1 mM Gd^{3+}) and different concentrations of Ca^{2+} was prepared, which match required concentrations for Gd^{3+} and induced Ca^{2+} concentration changes in the anticipated functional MRI experiments (see above).[32] Typical T_1- (fast low-angle shot, FLASH), T_2- (rapid acquisition with relaxation enhancement, RARE) and T_2/T_1-weighted (bSSFP) MRI experiments were then performed under optimized conditions for the highest contrast-to-noise ratio (CNR) for each set of tubes (DSCA or MSCA). Finally, the results obtained for three different image acquisitions were compared with each other (Figure 3; Figures S3 and S4 and Table S1 in the Supporting Information). We note that direction of the MRI signal changes (increase or decrease of the signal via so-called "turn-on" or "turn-off" mechanisms, respectively) does not play any role in functional

DOI: 10.1021/acssensors.6b00011
ACS Sens. 2016, 1, 483−487

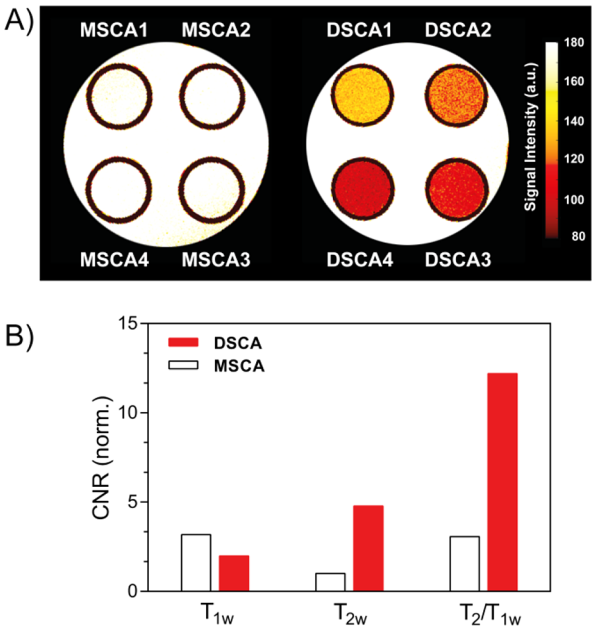

Figure 3. MRI on tube phantoms with MSCA and DSCA in the presence of Ca^{2+}. (A) MR images obtained with bSSFP for different concentrations of Ca^{2+} (MSCA1−4 or DSCA1−4 indicate 0, 0.4, 0.8, and 1.2 mM Ca^{2+}, respectively, $[Gd^{3+}]$ = 1 mM, pH 7.4, HEPES). (B) Comparison of normalized CNRs for MSCA and DSCA, obtained with T_{1w}, T_{2w}, and T_2/T_{1w} imaging sequences. CNR values were obtained by subtracting SNR values (Table S1 in the Supporting Information) and normalizing them by the square root of the respective acquisition time.

MRI as long as it can be unambiguously observed and analyzed.[33] Furthermore, Ca-induced r_1, r_2, and R_2/R_1 ratio changes with this type of SCAs are reversible;[32] hence every "turn-on" event (signal increase) is subsequently followed by the "turn-off" event (signal decrease), and vice versa.

The great advantage of the bSSFP methodology with SCAs can be seen immediately. MR images with SNR ∼ 7−10 were obtained in only 0.8 s using bSSFP with DSCA, providing over 30% signal difference between the contrast agent saturated with Ca^{2+} and without it. Meanwhile, a T_1-weighted FLASH sequence resulted in a signal enhancement of 27% and 14% for MSCA and DSCA, respectively, but this required almost 4 s acquisition time and SNR ∼ 5−6. Finally, a T_2-weighted RARE sequence with DSCA produced the highest SNR values and their changes (SNR ∼ 8−12, almost 40% change), but after longer acquisition times (10 s). For better comparison, we calculated experimentally obtained CNRs between these tubes, and normalized them using the square root of the time needed to acquire these signals. The obtained values indicate the gain of signal per unit of time and can be used for direct comparison of sequences and their performance with SCAs. Consequently, the normalized CNR enhancement obtained with DSCA and the bSSFP sequence is almost twice and half that with the T_2-weighted sequences, and over six times higher than with the T_1-weighted sequence. Furthermore, it is almost four times higher than the normalized CNR obtained for MSCA with the same T_1-weighted sequence, suggesting that the use of DSCA greatly improves the CNR compared to current small sized SCAs and conventional imaging methodologies. Given the high SNRs and SNR differences obtained with acquisition times shorter than a second, DSCA with bSSFP may indeed allow rapid detection of the MRI signal difference with the possibility of dynamic imaging at subsecond temporal resolution. This approach can be very useful for tracking biological processes by means of functional MRI, including brain activity.

In conclusion, the new ratiometric methodology using bioresponsive agents holds great promise for applications where dynamic processes need to be followed on a rapid temporal scale. In this specific case, we demonstrated its potential on tracking the changes in concentrations of calcium ions which can be of tremendous importance for neuroscience. However, this methodology has a much broader outlook: it requires a change in size and local environment of bioresponsive contrast agents. Such approaches have been frequently applied but so far only for MRI at low magnetic fields. In contrast, our approach is well-suited also for use at high magnetic fields and can in fact serve to revive abandoned older approaches. Additionally, its ability to rapidly produce strong SNRs opens new avenues for following the kinetics of different biological events, which can be especially valuable for studying interactions of bioresponsive agents with enzymes and proteins.

■ ASSOCIATED CONTENT

Supporting Information

The Supporting Information is available free of charge on the ACS Publications website at DOI: 10.1021/acssensors.6b00011.

Synthesis of dendrimeric SCA; additional NMR and MRI experiments (PDF)

■ AUTHOR INFORMATION

Corresponding Author

*E-mail: goran.angelovski@tuebingen.mpg.de.

Author Contributions

#S.G. and T.S. contributed equally.

Notes

The authors declare no competing financial interest.

■ ACKNOWLEDGMENTS

The authors thank Prof. Alan Jasanoff and Dr. Vincent Truffault for helpful discussions, and Prof. Thilo Stehle for access to the DLS instrument. The financial support of the Max-Planck Society and European COST TD1004 and CM1006 Actions is gratefully acknowledged.

■ REFERENCES

(1) Hingorani, D. V.; Bernstein, A. S.; Pagel, M. D. A review of responsive MRI contrast agents: 2005−2014. *Contrast Media Mol. Imaging* **2015**, *10*, 245−265.

(2) Heffern, M. C.; Matosziuk, L. M.; Meade, T. J. Lanthanide Probes for Bioresponsive Imaging. *Chem. Rev.* **2014**, *114*, 4496−4539.

(3) Que, E. L.; Chang, C. J. Responsive magnetic resonance imaging contrast agents as chemical sensors for metals in biology and medicine. *Chem. Soc. Rev.* **2010**, *39*, 51−60.

(4) Shapiro, M. G.; Westmeyer, G. G.; Romero, P. A.; Szablowski, J. O.; Kuster, B.; Shah, A.; Otey, C. R.; Langer, R.; Arnold, F. H.; Jasanoff, A. Directed evolution of a magnetic resonance imaging contrast agent for noninvasive imaging of dopamine. *Nat. Biotechnol.* **2010**, *28*, 264−270.

(5) Dommaschk, M.; Peters, M.; Gutzeit, F.; Schütt, C.; Näther, C.; Sönnichsen, F. D.; Tiwari, S.; Riedel, C.; Boretius, S.; Herges, R. Photoswitchable Magnetic Resonance Imaging Contrast by Improved Light-Driven Coordination-Induced Spin State Switch. *J. Am. Chem. Soc.* **2015**, *137*, 7552−7555.

DOI: 10.1021/acssensors.6b00011
ACS Sens. 2016, 1, 483−487

(6) Atanasijevic, T.; Shusteff, M.; Fam, P.; Jasanoff, A. Calcium-sensitive MRI contrast agents based on superparamagnetic iron oxide nanoparticles and calmodulin. *Proc. Natl. Acad. Sci. U. S. A.* **2006**, *103*, 14707−14712.
(7) Loving, G. S.; Caravan, P. Activation and Retention: A Magnetic Resonance Probe for the Detection of Acute Thrombosis. *Angew. Chem., Int. Ed.* **2014**, *53*, 1140−1143.
(8) De Leon-Rodriguez, L. M.; Lubag, A. J. M.; Malloy, C. R.; Martinez, G. V.; Gillies, R. J.; Sherry, A. D. Responsive MRI Agents for Sensing Metabolism in Vivo. *Acc. Chem. Res.* **2009**, *42*, 948−957.
(9) Bar-Shir, A.; Yadav, N. N.; Gilad, A. A.; van Zijl, P. C. M.; McMahon, M. T.; Bulte, J. W. M. Single ^{19}F Probe for Simultaneous Detection of Multiple Metal Ions Using miCEST MRI. *J. Am. Chem. Soc.* **2015**, *137*, 78−81.
(10) Yu, J.-X.; Hallac, R. R.; Chiguru, S.; Mason, R. P. New frontiers and developing applications in ^{19}F NMR. *Prog. Nucl. Magn. Reson. Spectrosc.* **2013**, *70*, 25−49.
(11) Harvey, P.; Blamire, A. M.; Wilson, J. I.; Finney, K. L. N. A.; Funk, A. M.; Senanayake, P. K.; Parker, D. Moving the goal posts: enhancing the sensitivity of PARASHIFT proton magnetic resonance imaging and spectroscopy. *Chem. Sci.* **2013**, *4*, 4251−4258.
(12) Shapiro, M. G.; Ramirez, R. M.; Sperling, L. J.; Sun, G.; Sun, J.; Pines, A.; Schaffer, D. V.; Bajaj, V. S. Genetically encoded reporters for hyperpolarized xenon magnetic resonance imaging. *Nat. Chem.* **2014**, *6*, 629−634.
(13) Ekanger, L. A.; Allen, M. J. Overcoming the concentration-dependence of responsive probes for magnetic resonance imaging. *Metallomics* **2015**, *7*, 405−421.
(14) Aime, S.; Fedeli, F.; Sanino, A.; Terreno, E. A R_2/R_1 ratiometric procedure for a concentration-independent, pH-responsive, Gd(III)-based MRI agent. *J. Am. Chem. Soc.* **2006**, *128*, 11326−11327.
(15) Catanzaro, V.; Gringeri, C. V.; Menchise, V.; Padovan, S.; Boffa, C.; Dastru, W.; Chaabane, L.; Digilio, G.; Aime, S. A R_{2p}/R_{1p} Ratiometric Procedure to Assess Matrix Metalloproteinase-2 Activity by Magnetic Resonance Imaging. *Angew. Chem., Int. Ed.* **2013**, *52*, 3926−3930.
(16) Dorazio, S. J.; Olatunde, A. O.; Spernyak, J. A.; Morrow, J. R. CoCEST: cobalt(II) amide-appended paraCEST MRI contrast agents. *Chem. Commun.* **2013**, *49*, 10025−10027.
(17) Zhang, S. R.; Malloy, C. R.; Sherry, A. D. MRI thermometry based on PARACEST agents. *J. Am. Chem. Soc.* **2005**, *127*, 17572−17573.
(18) Okada, S.; Mizukami, S.; Sakata, T.; Matsumura, Y.; Yoshioka, Y.; Kikuchi, K. Ratiometric MRI Sensors Based on Core-Shell Nanoparticles for Quantitative pH Imaging. *Adv. Mater.* **2014**, *26*, 2989−2992.
(19) Bhuiyan, M. P. I.; Aryal, M. P.; Janic, B.; Karki, K.; Varma, N. R. S.; Ewing, J. R.; Arbab, A. S.; Ali, M. M. Concentration-independent MRI of pH with a dendrimer-based pH-responsive nanoprobe. *Contrast Media Mol. Imaging* **2015**, *10*, 481−486.
(20) Scheffler, K.; Lehnhardt, S. Principles and applications of balanced SSFP techniques. *Eur. Radiol.* **2003**, *13*, 2409−2418.
(21) Tu, C. Q.; Osborne, E. A.; Louie, A. Y. Activatable T_1 and T_2 Magnetic Resonance Imaging Contrast Agents. *Ann. Biomed. Eng.* **2011**, *39*, 1335−1348.
(22) Gündüz, S.; Nitta, N.; Vibhute, S.; Shibata, S.; Maier, M. E.; Logothetis, N. K.; Aoki, I.; Angelovski, G. Dendrimeric calcium-responsive MRI contrast agents with slow *in vivo* diffusion. *Chem. Commun.* **2015**, *51*, 2782−2785.
(23) Norek, M.; Kampert, E.; Zeitler, U.; Peters, J. A. Tuning of the Size of Dy_2O_3 Nanoparticles for Optimal Performance as an MRI Contrast Agent. *J. Am. Chem. Soc.* **2008**, *130*, 5335−5340.
(24) Dhingra Verma, K.; Mishra, A.; Engelmann, J.; Beyerlein, M.; Maier, M. E.; Logothetis, N. K. Magnetic-Field-Dependent ^{1}H Relaxivity Behavior of Biotin/Avidin-Based Magnetic Resonance Imaging Probes. *ChemPlusChem* **2012**, *77*, 758−769.
(25) Botta, M.; Tei, L. Relaxivity Enhancement in Macromolecular and Nanosized Gd^{III}-Based MRI Contrast Agents. *Eur. J. Inorg. Chem.* **2012**, *2012*, 1945−1960.
(26) Gündüz, S.; Power, A.; Maier, M. E.; Logothetis, N. K.; Angelovski, G. Synthesis and Characterization of a Biotinylated Multivalent Targeted Contrast Agent. *ChemPlusChem* **2015**, *80*, 612−622.
(27) Merbach, A. E.; Helm, L.; Tóth, É. *The chemistry of contrast agents in medical magnetic resonance imaging*, 2nd ed.; Wiley: Chichester, 2013.
(28) Somjen, G. G. *Ions in the brain: normal function, seizures, and strokes*; Oxford University Press: New York, Oxford, 2004.
(29) Botta, M.; Aime, S.; Barge, A.; Bobba, G.; Dickins, R. S.; Parker, D.; Terreno, E. Ternary complexes between cationic Gd^{III} chelates and anionic metabolites in aqueous solution: An NMR relaxometric study. *Chem. - Eur. J.* **2003**, *9*, 2102−2109.
(30) Nwe, K.; Bryant, L. H.; Brechbiel, M. W. Poly(amidoamine) Dendrimer Based MRI Contrast Agents Exhibiting Enhanced Relaxivities Derived via Metal Preligation Techniques. *Bioconjugate Chem.* **2010**, *21*, 1014−1017.
(31) Henig, J.; Mamedov, I.; Fouskova, P.; Tóth, E.; Logothetis, N. K.; Angelovski, G.; Mayer, H. A. Influence of Calcium-Induced Aggregation on the Sensitivity of Aminobis(methylenephosphonate)-Containing Potential MRI Contrast Agents. *Inorg. Chem.* **2011**, *50*, 6472−6481.
(32) Angelovski, G.; Gottschalk, S.; Milošević, M.; Engelmann, J.; Hagberg, G. E.; Kadjane, P.; Andjus, P.; Logothetis, N. K. Investigation of a Calcium-Responsive Contrast Agent in Cellular Model Systems: Feasibility for Use as a Smart Molecular Probe in Functional MRI. *ACS Chem. Neurosci.* **2014**, *5*, 360−369.
(33) Lee, T.; Cai, L. X.; Lelyveld, V. S.; Hai, A.; Jasanoff, A. Molecular-Level Functional Magnetic Resonance Imaging of Dopaminergic Signaling. *Science* **2014**, *344*, 533−535.

DOI: 10.1021/acssensors.6b00011
ACS Sens. 2016, 1, 483−487

Supporting Information for

Ratiometric Method for Rapid Monitoring of Biological Processes Using Bioresponsive MRI Contrast Agents

Serhat Gündüz,[1,†] Tanja Savić,[1,†] Rolf Pohmann,[2] Nikos K. Logothetis,[3,4] Klaus Scheffler[2,5] and Goran Angelovski[1,*]

[1] MR Neuroimaging Agents, Max Planck Institute for Biological Cybernetics, Spemannstr. 41, 72076 Tübingen, Germany, E-mail: goran.angelovski@tuebingen.mpg.de

[2] High-Field Magnetic Resonance, Max Planck Institute for Biological Cybernetics, Tübingen, Germany.

[3] Physiology of Cognitive Processes, Max Planck Institute for Biological Cybernetics, Tübingen, Germany.

[4] Department of Imaging Science and Biomedical Engineering, University of Manchester, Manchester, UK.

[5] Department for Biomedical Magnetic Resonance, University of Tübingen, Tübingen, Germany.

[†] Contributed equally to this work.

Table of Contents

General remarks

Commercially available reagents and solvents were used without further purification. **MSCA** and isothiocyanate **1** for synthesis of dendrimeric **DSCA** were synthesized according to a published procedure.[1] G4 Starburst® PAMAM dendrimer with cystamine core was purchased from Dendritic Nanotechnologies, Inc., USA. Dendrimer **2** was purified using lipophilic Sephadex®LH-20 (bead size: 25-100 μm) from Sigma-Aldrich (Germany). Brain extracellular model (BEM) solution was prepared from Ca-free Dulbecco's Modified Eagle's Medium (DMEM, without L-glutamine, sodium pyruvate and calcium chloride), Ham's F-12 Nutrient Mixture (F-12) and N-2 supplement (N-2) from Life Technologies GmbH, Germany. MALDI-TOF-MS analysis was performed by The Scripps Center for Mass Spectrometry, La Jolla, CA. ^{1}H and ^{13}C- NMR spectra, relaxometric experiments and NMR diffusion measurements were performed on a Bruker Avance III 300 MHz spectrometer at 25 ^{o}C using 5 mm NMR tubes. Processing was performed using TopSpin 2.1 (Bruker GmbH) and ACD/SpecManager 9.0 (Advanced Chemistry Development, Inc.). The NMR spectra were obtained either in $CDCl_3$ or D_2O, using the deuterium lock frequency. The concentration of Gd^{3+} in analyzed solutions was determined using the bulk magnetic susceptibility shift (BMS).[2] Diffusion experiments were carried out on samples filtered through 0.20 μm PTFE filters from Carl Roth GmbH + Co. KG, Germany. DLS measurements were done on a Malvern-Nano-ZS (Zetasizer, software ver. 6.2) instrument. MRI measurements were performed on a Bruker BioSpec 70/30 USR magnet (software ver. Paravision 5.1) using Bruker dual frequency volume coil (RF RES 300 1H/19F 075/040 LIN/LIN TR).

Synthesis of DSCA

Dendrimer 2. G4 PAMAM dendrimer (80 mg, 5.6 μmol) and isothiocyanate 1 (650 mg, 539 μmol) were dissolved in dimethylformamide (5 mL) and triethylamine (200 μL, 1.4 mmol) was added to the solution. The reaction mixture was stirred at 45 °C for 24 h. The solvent was evaporated and the unreacted ligand was removed using a lipophilic Sephadex column with methanol as eluent to obtain protected dendrimeric chelator **2** (270 mg, 53%).

^{1}H NMR (300 MHz, $CDCl_3$): δ 7.2 (br, Ar*H*), 7.04 (br, Ar*H*), 4.10–1.70 (overlapping m), 1.55–1.25 (overlapping m, C(C*H*$_3$)$_3$). MALDI-TOF/MS (m/z): $[M+44Na]^{2+}$ calcd. for $C_{3024}H_{5372}N_{610}Na_{44}O_{684}S_{42}^{2+}$, 31790, found 31792.

Dendrimer 3. The protected dendrimeric chelator **2** (150 mg, 2.9 μmol) was dissolved in formic acid (5 mL) and the mixture was stirred at 60 ^oC for 48 h. The residue was purified by centrifugation using 3 KDa molecular weight cut-off filters and freeze-dried to give dendrimeric chelator **3** as a light brown solid (135 mg, 90%).

^{1}H NMR (300 MHz, D_2O): δ 7.24 (br, Ar*H*), 4.25−2.45 (overlapping m), 1.84 (br. s). MALDI-TOF/MS (m/z): $[M+46Na+12H_2O]^{2+}$ calcd. for $C_{2224}H_{3772}N_{610}Na_{46}O_{684}S_{42}(H_2O)_{12}^{2+}$, 26311, found 26308.

Dendrimer DSCA. Dendrimeric chelator **3** (138 mg, 2.4 μmol) was dissolved in water and the pH was adjusted to 7.0 with aqueous sodium hydroxide (0.1 M). A solution of $GdCl_3·6H_2O$ (61 mg, 164 μmol) in water was added and pH was maintained at 7.0. The mixture was stirred at room temperature for 24 h. EDTA (123 mg, 329 μmol) was added into the solution to remove excess Gd^{3+} while maintaining pH at 7.0. Excess GdEDTA and EDTA were removed by centrifugation using 3 KDa molecular weight cut-off filters and the resulting solution was lyophilized to give **DSCA** as a brown solid (151 mg, 85%).

MALDI-TOF/MS (m/z): $[M+53Na+78H_2O]^{2+}$ calcd. for $C_{2224}H_{3652}Gd_{40}N_{610}Na_{53}O_{684}S_{42}(H_2O)_{78}^{2+}$, 30070, found 30066; $[M+36Na+43H_2O]^{2+}$ calcd. for $C_{2145}H_{3534}Eu_{38}N_{592}Na_{36}O_{656}S_{40}(H_2O)_{43}^{2+}$, 28386, found 28385.

NMR relaxometric experiments

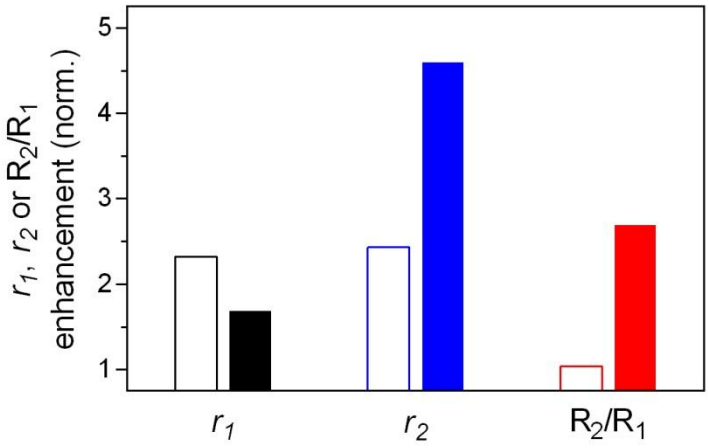

Figure S1. Increase of the r_1, r_2 and the R_2/R_1 ratio for **MSCA** (clear bars) and **DSCA** (color-filled bars) upon saturation with Ca^{2+} (HEPES, pH 7.4).The plots show normalized values where the final r_1, r_2 or R_2/R_1 ratio value (at Ca^{2+} saturation) is divided by the initial value (in absence of Ca^{2+}).

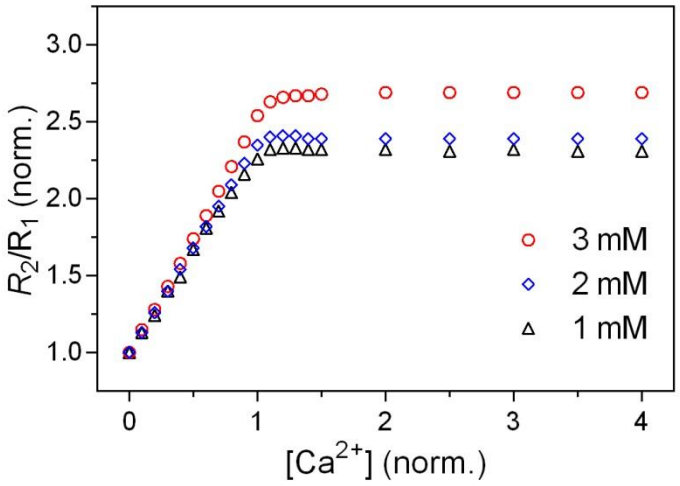

Figure S2. Longitudinal and transverse relaxometric titrations of **DSCA** with Ca^{2+} at 7 T and different Gd^{3+} concentrations (pH 7.4, HEPES). The plots show normalized values where the final r_1, r_2 or R_2/R_1 ratio value (at Ca^{2+} saturation) is divided by the initial value (in absence of Ca^{2+}).

DLS experiments

Measurements were carried out with Eu^{3+} complex of **DSCA** (0.75 mM Eu^{3+}) with and without addition of 2 equiv. of Ca^{2+}. They included 5 repetitions of 15 scans (1 scan = 12 sec, refractive index 1.345, absorption 1 %), without delays in between the scans, and with equilibration of 30 sec prior to recording. For comparison with NMR diffusion experiments, the diffusion coefficient was calculated from the obtained diameter using the Stokes-Einstein equation (Eq. 1) and assuming spherical sample approximation, where k is the Boltzmann constant, T – absolute temperature (298.15 K), r – hydrodynamic radius of a sample, η – viscosity of the water (0.8872 mPa s). The reversed procedure was performed for the diffusion coefficient obtained with NMR measurements of **MSCA** (see below).

$$D = \frac{k\,T}{6\,\pi\,r\,\eta} \qquad \text{[Eq. 1]}$$

NMR diffusion experiments

Determination of diffusion coefficient was performed using 2D – Diffusion Ordered NMR Spectroscopy (DOSY).[3] Experiments included 3 repetitions on Eu^{3+} complex of **MSCA** (15 mM) with and without 2 equiv. of Ca^{2+} (δt= 2 ms, ΔT= 330 ms). Data analysis was done with TopSpin 2.1 using 16 linear points between 5–95 % gradient strength.

MRI phantom experiments

MRI experiments were performed on tubes containing solutions of **DSCA** or **MSCA** (1 mM Gd^{3+}) to which 0, 0.4, 0.8 and 1.2 equiv. of Ca^{2+} were added (DSCA1=MSCA1=0 mM Ca^{2+}, DSCA2=MSCA2=0.4 mM Ca^{2+}, DSCA3=MSCA3=0.8 mM Ca^{2+}, DSCA4=MSCA4=1.2 mM Ca^{2+}). Each set (DSCA1–4 or MSCA1–4) was placed in 4×200 µl plastic tubes and inserted into a 20 mL syringe filled with solution of Dotarem® in water (162 mM) in order to avoid susceptibility artifacts.

Firstly, T_1 and T_2 times were determined from respective T_1 and T_2 maps using rapid acquisition with relaxation enhancement (RARE) with inversion recovery (IR-RARE) and multi-slice multi-

echo (MSME) sequences, respectively. IR-RARE was performed with the following parameters: field-of-view (FOV)=40x40 mm^2, matrix size (MTX)=256x256, 1 slice, slice thickness 1 mm, echo time (TE)=9.725 ms, repetition time (TR)=1500 ms, Rare factor=8, inversion times (TI): 90, 150, 200, 250, 300, 350, 400, 450, 500, 600, 700, 800, 900, 1000, 1150, 1300 ms, number of averages (NA)=1, total acquisition time (TA)=36 s, while MSME with FOV=40x40 mm^2, MTX=128x128, 1 slice, slice thickness 1 mm, TR=1500 ms, TE: 10, 15, 20, 25, 30, 35, 40, 45, 50, 55, 60, 70, 80, 90, 100, 135, 170, 200 ms; NA=1,TA=3 min 12 s. Obtained T_1 and T_2 times were further employed for numerical CNR optimization of acquisition parameters for T_1-, T_2- and T_2/T_1-weighted imaging. Numerical CNR optimization for FLASH, bSSFP and RARE was based on Bloch simulations that optimize the signal difference for different contrast agents. The resulting optimized TR and flip angle were then used for measurements and the signal difference was normalized with the square root of the total measuring time.[4]

MRI was accomplished using T_1-, T_2- and T_2/T_1-weighted sequences: fast low angle shot (FLASH), RARE and balanced steady state free precession (bSSFP) pulse sequence, respectively, with FOV=25x25 mm^2, MTX=256x256, 1 slice and slice thickness 1 mm.

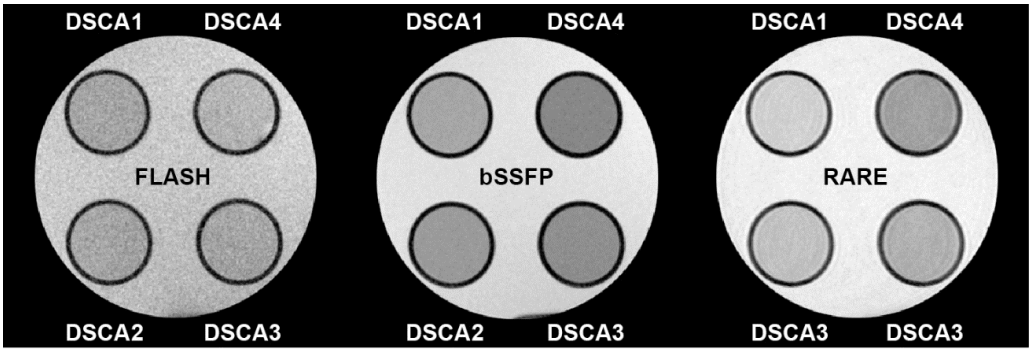

Figure S3. Comparison of MRI sequences with **DSCA** at different Ca^{2+} concentrations ([Gd^{3+}]= 1 mM, 7T, pH 7.4, HEPES). Parameters for FLASH: TR/TE= 3.797/1.494 ms, FA= 19, NA=16, TA= 15.552 s, for bSSFP: TR/TE=3/1.5 ms, FA=81, NA=16, TA=12.288 s, and for RARE: TR/TE= 620/9.284 ms, Rare factor=16, NA=16, TA= 2 m 38 s 720 ms.

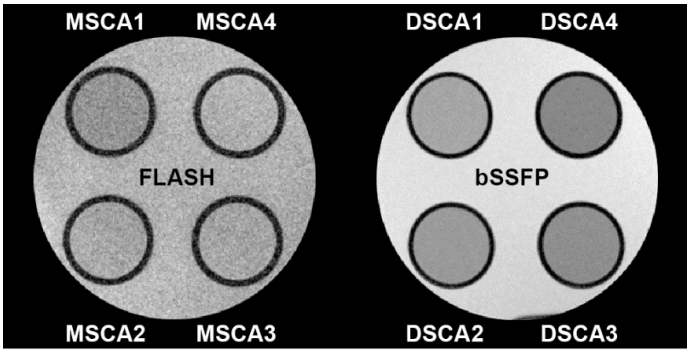

Figure S4. Comparison of FLASH sequence with **MSCA** and bSSFP sequence with **DSCA** at different Ca^{2+} concentrations ([Gd^{3+}]= 1mM, 7T, pH 7.4, HEPES). Parameters for FLASH: TR/TE= 3.4/1.494 ms, FA= 21, NA=16, TA= 13.926 s, and for bSSFP: TR/TE=3/1.5 ms, FA=81, NA=16, TA=12.288 s.

Table S1. SNR values obtained for **DSCA** and **MSCA** in the presence or absence of 1.2 equiv. of Ca^{2+}, using T_1-, T_2- and T_2/T_1-weighted sequences.

Contrast agent	**T_1-weighted (FLASH) [a)]**		**T_2-weighted (RARE) [b)]**		**T_2/T_1-weighted (bSSFP) [c)]**	
	No Ca^{2+}	+ Ca^{2+} (1.2 equiv.)	No Ca^{2+}	+ Ca^{2+} (1.2 equiv.)	No Ca^{2+}	+ Ca^{2+} (1.2 equiv.)
DSCA	5.41	6.27	11.83	8.50	9.75	7.39
MSCA	4.81	6.12	13.44	12.60	10.41	10.95

a) **DSCA**: TA=3888 ms, **MSCA**: TA=3481 ms; b) **DSCA**: TA=9920 ms, **MSCA**: TA=14400 ms; c) TA=767.5 ms.

References

1. Gündüz, S.; Nitta, N.; Vibhute, S.; Shibata, S.; Maier, M. E.; Logothetis, N. K.; Aoki, I.; Angelovski, G., Dendrimeric calcium-responsive MRI contrast agents with slow in vivo diffusion. *Chem. Commun.* **2015,** *51*, 2782-2785.

2. Corsi, D. M.; Platas-Iglesias, C.; van Bekkum, H.; Peters, J. A., Determination of paramagnetic lanthanide(III) concentrations from bulk magnetic susceptibility shifts in NMR spectra. *Magn. Reson. Chem.* **2001,** *39*, 723-726.

3. Macchioni, A.; Ciancaleoni, G.; Zuccaccia, C.; Zuccaccia, D., Determining accurate molecular sizes in solution through NMR diffusion spectroscopy. *Chem. Soc. Rev.* **2008,** *37*, 479-489.

4. Hagberg, G. E.; Scheffler, K., Effect of r_1 and r_2 relaxivity of gadolinium-based contrast agents on the T_1-weighted MR signal at increasing magnetic field strengths. *Contrast Media Mol. Imaging* **2013,** *8*, 456-465.

Early detection and monitoring of cerebral ischemia using calcium-responsive MRI probes

Tanja Savić,[1] Giuseppe Gambino,[1] Vahid Bokharaie,[1] Hamid R. Noori,[1] Nikos K. Logothetis,[1,2] and Goran Angelovski[1*]

[1]Max Planck Institute for Biological Cybernetics, Tuebingen, Germany

[2]Department of Imaging Science and Biomedical Engineering, University of Manchester, Manchester, United Kingdom

*Correspondence to: goran.angelovski@tuebingen.mpg.de

Abstract: Cerebral ischemia is one of the leading causes of mortality and disability in infants and adults and its timely diagnosis is essential for an efficient treatment. We present a methodology for fast detection and real time monitoring of fluctuations of calcium ions associated with focal ischemia using a molecular fMRI (functional magnetic resonance imaging) approach with the paramagnetic bioresponsive probes. Our method sensitively recognizes the onset and spatiotemporal dynamics of ischemic core and penumbra with a high resolution and paves the way for non-invasive monitoring and development of targeted treatment strategies for cerebral ischemia.

Manuscript Text

Cerebrovascular diseases (stroke) rank as the second leading cause of mortality, accounting for 9.6% of all death worldwide [1, 2]. Understanding the complex pathophysiology of focal cerebral ischemia requires the use of reproducible experimental models to characterize the ischemic penumbra [3]. For clinicians, the most relevant aspect is likely the identification of portions of the ischemic tissue that are still potentially reversible [4]. Thus, accurate and timely detection, visualization and monitoring of the spatiotemporal course of ischemia are of great practical relevance in the treatment and recovery of ischemic injuries [5, 6]. The most commonly used imaging techniques for ischemia diagnosis in infants and adults are ultrasonography and computed tomography. However, they often lack the necessary sensitivity to detect ischemia at an early stage [7]. To date, magnetic resonance imaging (MRI) is considered as a more reliable neuroimaging technique, as it allows a better differentiation of the damaged regions at earlier stages of ischemic injury [8]. Nonetheless, the current utilization of MRI-based technologies, characterized by great spectral sensitivity, spatial localization, and potentially quantitative tracking of changes in the concentration of various substances, is only in the beginning of a very promising path. This may lead to the understanding of dynamic, site-specific and temporally differentiated processes, such as that of tissue ischemia. Cerebral ischemia, specifically, results in a reduced blood supply to the brain tissue, causing oxygen-glucose deprivation and adenosine triphosphate (ATP) production failure. The resulting energy crisis can trigger a cascade of detrimental biochemical and physiological events, including strong disturbances in calcium homeostasis, leading to acute or delayed cell death [9]. It has been shown that, upon ischemia, the extracellular calcium concentration ($[Ca^{2+}]_e$) decreases dramatically [10, 11]. Changes in cerebral calcium concentration can therefore provide a marker for monitoring the intensity and duration of ischemic injuries. Traditionally, measurements of $[Ca^{2+}]_e$ have only been

performed locally using calcium-sensitive microprobes [12]. In recent years there has been substantial progress towards the development of molecular markers capable of monitoring changes in calcium concentration using functional MRI (fMRI) [13-15]. Yet, not surprisingly, such early studies have been focusing mostly on technological optimization and advancements, rather than on clinically relevant applications.

Here, we report the development and application of a functional fMRI-biomarker which enables real-time *in vivo* monitoring of fluctuations of calcium concentration associated with cerebral ischemia. This molecular probe is a bismacrocyclic gadolinium(III) complex $\mathbf{Gd_2L^1}$ that bears a common EGTA-derived calcium chelator (EGTA - ethylene glycol tetraacetic acid) acting as a so-called Smart Contrast Agent (SCA), changing the longitudinal relaxivity (r_1) of tissues, as observed in cellular model systems [16]. The advantage of this chelate is the possession of two gadolinium ions along with a single calcium-chelating unit, thus producing double the T_1 effect from two gadolinium ions per unit of calcium. The efficacy and selectivity of $\mathbf{Gd_2L^1}$ was assessed in comparison to a control probe, an analogous chelate $\mathbf{Gd_2L^2}$ (Fig. 1a and Supplementary Fig. S1), which lacked the $[Ca^{2+}]$-dependent variability of r_1, but maintained the same size, charge and calcium-chelating part of $\mathbf{Gd_2L^1}$. *In vitro* experiments in buffered media showed a significant increase of r_1 for $\mathbf{Gd_2L^1}$ upon addition of calcium ions and virtually no change for $\mathbf{Gd_2L^2}$ under the same conditions (Fig. 1b). At ambient temperature, tube phantom with $\mathbf{Gd_2L^1}$ generated lower T_1-weighted MRI signal at low calcium concentrations and higher signal as the calcium concentration increased, whilst the T_1-weighted MRI signal produced by $\mathbf{Gd_2L^2}$ remained insensitive to any changes in calcium concentration (Fig. 1c).

Fig. 1 here

To demonstrate the appropriateness of our molecular fMRI technique for monitoring transient ischemia, we chose a remote transient middle cerebral artery occlusion (tMCAo) protocol (Fig. 1d-g) [17]. Since approximately 70% of human ischemic strokes are caused by an occlusion of the MCA and its branches [18], this approach can be considered to be a representative model to study molecular mechanisms of brain injury. The methodology involved the continuous infusion of the SCA in the somatosensory cortex of adult rats (Fig. 1e-g), while remotely controlling tMCAo inside the scanner. $\mathbf{Gd_2L^1}$ or $\mathbf{Gd_2L^2}$ were infused intracranially using a subcutaneously positioned osmotic pump. A silicone-coated occluder was introduced through the support tubing and connected with the intra-arterial tubing fixated inside the common carotid artery. Preparation was completed when the occluder was advanced through the internal carotid artery, 2 mm after bifurcation with pterygopalatine artery (Fig. 1f left). Once the animal was positioned inside the 7T MRI scanner, an imaging protocol consisting of a series of T_1-weighted MR acquisitions was executed every two minutes. Each experiment was divided into three segments: pre-ischemia, ischemia, and reperfusion period. Transient ischemia was induced by advancing the occluder for 6-8 mm until resistance was felt, while reperfusion was allowed using the reverse action (Fig. 1f right). This procedure was applied for both contrast agents $\mathbf{Gd_2L^1}$ and $\mathbf{Gd_2L^2}$ (n=5 animals/agent). The successful induction of ischemia is confirmed at the end of the experimental procedure by applying a standard diffusion weighted imaging (DWI) protocol (Supplementary Fig. S2 left) [19, 20]. In addition, control experiments with $\mathbf{Gd_2L^1}$ and $\mathbf{Gd_2L^2}$ (n=5 animals/agent) without the transient ischemia induction were conducted to characterize the diffusion profile of the applied contrast agents. K-means clustering on masked normalized T_1-weighted images suggested co-centric patterns of SCA propagation in the brain tissue

(Fig. 2a). Thereby, centroids of clusters closer to the epicenter of injection have higher values on average, which is a reflection of higher local probe concentration. This qualitative behavior can be seen in all experiments and was not affected by variations in the choice of number of clusters (Supplementary Fig. S3-4). Additionally, we used a hierarchical clustering, which resulted in ROIs whose sizes are similar to each other even when the initial masks had widely varying numbers of voxels while maintaining the same behavior of the centroids as previously described (Supplementary Fig. S5-6).

Using an algorithm which comprises a customized detrending scheme, we have shown the differences in responses for the two different molecules during the tMCAo experiment (Supplementary Fig. S7). The results show a clear distinction between signals obtained from $\mathbf{Gd_2L^1}$ and from $\mathbf{Gd_2L^2}$ when tMCAo is induced. In agreement with previous studies documenting a reduction of $[Ca^{2+}]_e$, the intensity of the T_1-weighted MRI signal due to the interaction of $\mathbf{Gd_2L^1}$ with extracellular calcium is reduced during ischemia, and recovered as brain tissue is re-perfused (Fig. 2c left). The selectivity of $\mathbf{Gd_2L^1}$ for calcium *in vivo* is further demonstrated by the T_1-weighted MRI signal in the presence of the control probe $\mathbf{Gd_2L^2}$. The signal intensity remains unperturbed by the onset and recovery of ischemia (Fig. 2c right). Likewise, control experiments performed with both CAs without induction of tMCAo showed similar results (Supplementary Fig. S8). The mean values of detrended signals in the ischemia experiments separated by molecule type and time-segments demonstrate the appropriateness of our method to detect the onset and time-course of ischemic injury (Fig. 2d, Supplementary Tables S1-2). Thus, $\mathbf{Gd_2L^1}$ can be used as a reliable marker for ischemia.

Fig. 2 here

Quantitative estimates of the pace of neural circuitry loss in human ischemic stroke emphasize the time urgency of stroke care [5]. Our method can detect ischemia rapidly, only minutes after the tMCAo onset, which is orders of magnitude faster than the speed of detection of ischemia using DWI and T_2-weighted MRI (Supplementary Fig. S2). In addition, DWI or T_2-weighted MRI could not capture the transient behavior of $[Ca^{2+}]_e$ during ischemia, as we have successfully achieved with our method.

In summary, we introduce here a novel and robust tool to monitor $[Ca^{2+}]_e$ alterations *in vivo* that can enable the early detection and real-time monitoring of brain ischemic injuries. Evidently the potential applications of our method are not limited to ischemia, as changes in $[Ca^{2+}]_e$ are associated with a large number of different biological processes. This novel molecular fMRI technique can thus prove to be an essential supplement to conventional fMRI techniques for the study of brain function and dysfunction, enabling direct visualization and mapping of synaptic neural activity.

Acknowledgments: The work was supported by the German Federal Ministry of Education and Research (BMBF, e:Med program: FKZ: 01ZX1503).

Author contributions: T.S., N.K.L and G.A. designed the research, G.G. synthesized the molecules, T.S. and G.G. performed the in vitro experiments, T.S. performed the in vivo experiments, G.A. supervised experiments, V.B. and H.R.N. performed data analysis, all authors wrote the paper.

Competing interests statement: Authors declare no competing interests.

References:

1. WHO (World Health Organization, Geneva; 2002).
2. Feigin, V.L., Lawes, C.M.M., Bennett, D.A. & Anderson, C.S. Stroke epidemiology: a review of population-based studies of incidence, prevalence, and case-fatality in the late 20th century. *Lancet Neurol.* **2**, 43-53 (2003).
3. Hossmann, K.A. Viability Thresholds and the Penumbra of Focal Ischemia. *Ann. Neurol.* **36**, 557-565 (1994).
4. Fisher, M. The ischemic penumbra: Identification, evolution and treatment concepts. *Cerebrovasc. Dis.* **17**, 1-6 (2004).
5. Saver, J.L. Time is brain - Quantified. *Stroke* **37**, 263-266 (2006).
6. Markus, R. et al. Hypoxic tissue in ischaemic stroke: persistence and clinical consequences of spontaneous survival. *Brain* **127**, 1427-1436 (2004).
7. Schaefer, P.W. et al. Quantitative Assessment of Core/Penumbra Mismatch in Acute Stroke CT and MR Perfusion Imaging Are Strongly Correlated When Sufficient Brain Volume Is Imaged. *Stroke* **39**, 2986-2992 (2008).
8. Moustafa, R.R. & Baron, J.C. Pathophysiology of ischaemic stroke: insights from imaging, and implications for therapy and drug discovery. *Brit. J. Pharmacol.* **153**, S44-S54 (2008).
9. Goldberg, W.J., Kadingo, R.M. & Barrett, J.N. Effects of Ischemia-Like Conditions on Cultured Neurons - Protection by Low Na^+, Low Ca^{2+} Solutions. *J. Neurosci.* **6**, 3144-3151 (1986).
10. Li, P.-A., Kristián, T., Katsura, K.-I., Shamloo, M. & Siesjö, B.K. The influence of insulin-induced hypoglycemia on the calcium transients accompanying reversible forebrain ischemia in the rat. *Exp. Brain. Res.* **105**, 363-369 (1990).
11. Siemkowicz, E. & Hansen, A.J. Brain Extracellular Ion Composition and EEG Activity Following 10 Minutes Ischemia in Normo- and Hyperglycemic Rats. *Stroke* **12**, 236-240 (1981).
12. Nicholson, C., ten Bruggencate, G., Steinberg, R. & Stöckle, H. Calcium modulation in brain extracellular microenvironment demonstrated with ion-selective micropipette. *Proc. Natl. Acad. Sci. U.S.A.* **74**, 1287-1290 (1977).
13. Ghosh, S., Harvey, P., Simon, J.C. & Jasanoff, A. Probing the brain with molecular fMRI. *Curr. Opin. Neurobiol.* **50**, 201-210 (2018).
14. Okada, S. et al. Calcium-dependent molecular fMRI using a magnetic nanosensor. *Nat. Nanotechnol.* **13**, 473-477 (2018).
15. Moussaron, A. et al. Ultrasmall Nanoplatforms as Calcium-Responsive Contrast Agents for Magnetic Resonance Imaging. *Small* **11**, 4900-4909 (2015).
16. Angelovski, G. et al. Investigation of a Calcium-Responsive Contrast Agent in Cellular Model Systems: Feasibility for Use as a Smart Molecular Probe in Functional MRI. *ACS Chem. Neurosci.* **5**, 360-369 (2014).
17. Koizumi, J.-i., Yoshida, Y., Nakazawa, T. & Ooneda, G. Experimental studies of ischemic brain edema. 1. A new experimental model of cerebral embolism in rats in which recirculation can be introduced in the ischemic area. *Jpn. J. Stroke* **8**, 1-8 (1986).

18. Bogousslavsky, J., Vanmelle, G. & Regli, F. The Lausanne Stroke Registry - Analysis of 1,000 Consecutive Patients with First Stroke. *Stroke* **19**, 1083-1092 (1988).
19. Hoehn, M., Nicolay, K., Franke, C. & van der Sanden, B. Application of magnetic resonance to animal models of cerebral ischemia. *J. Magn. Reson. Imaging* **14**, 491-509 (2001).
20. Mintorovitch, J. et al. Comparison of Diffusion-Weighted and T2-Weighted MRI for the Early Detection of Cerebral-Ischemia and Reperfusion in Rats. *Magn. Reson. Med.* **18**, 39-50 (1991).

Fig. 1

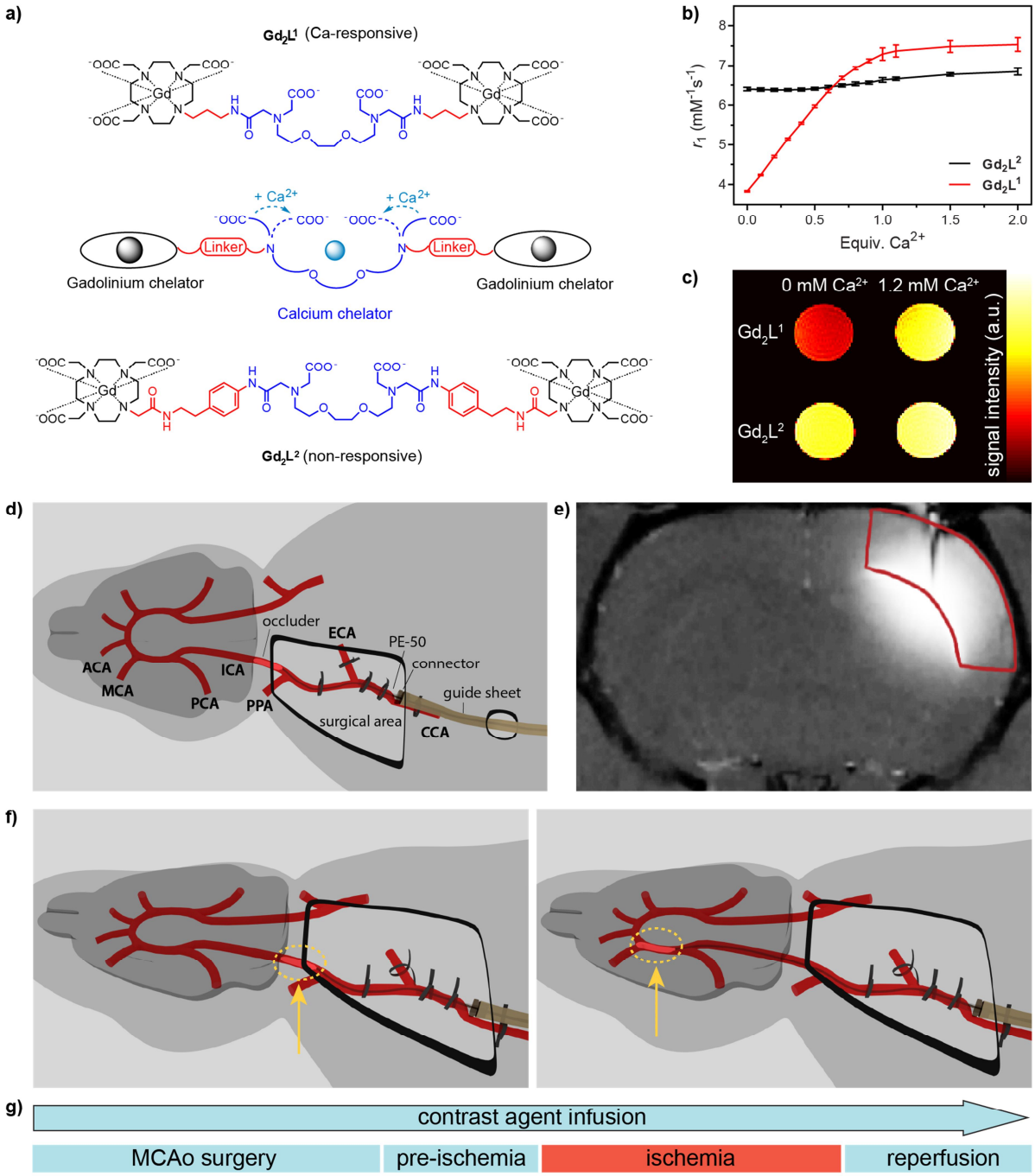
a)
Gd2L1 (Ca-responsive)
+ Ca2+
+ Ca2+
Linker
Linker
Gadolinium chelator
Gadolinium chelator
Calcium chelator
Gd2L2 (non-responsive)
b)
r1 (mM-1s-1)
Equiv. Ca2+
Gd2L2
Gd2L1
c)
0 mM Ca2+
1.2 mM Ca2+
Gd2L1
Gd2L2
signal intensity (a.u.)
d)
occluder
ECA
PE-50
connector
ACA
ICA
MCA
PCA
PPA
guide sheet
surgical area
CCA
e)
f)
g)
contrast agent infusion
MCAo surgery
pre-ischemia
ischemia
reperfusion

Fig. 2

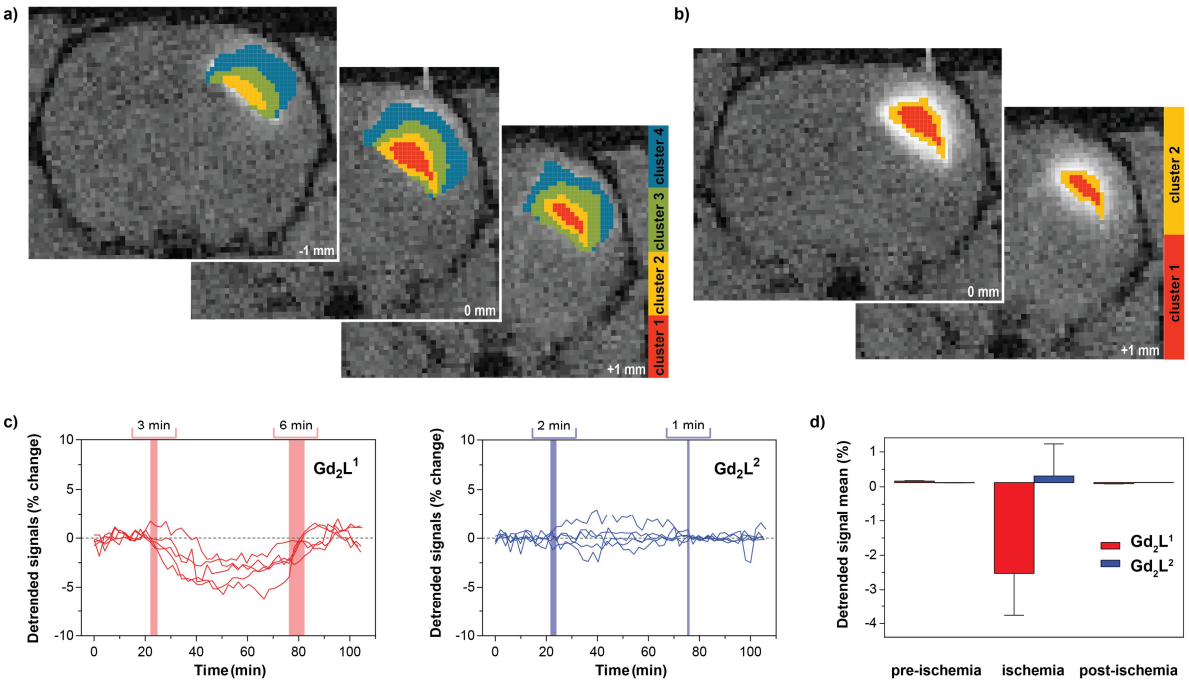
a)
-1 mm
0 mm
+1 mm
cluster 1
cluster 2
cluster 3
cluster 4
b)
0 mm
+1 mm
cluster 1
cluster 2
c)
3 min
6 min
Gd2L1
Detrended signals (% change)
Time (min)
2 min
1 min
Gd2L2
Detrended signals (% change)
Time (min)
d)
Detrended signal mean (%)
Gd2L1
Gd2L2
pre-ischemia
ischemia
post-ischemia

Fig. 1 Caption

Detection and monitoring of tMCAo with Ca-responsive MRI probes. a) Molecular structures of the responsive $\mathbf{Gd_2L^1}$ (top) and the control, non-responsive $\mathbf{Gd_2L^2}$ (bottom) with the interaction mechanism of the SCA (middle); b) Proton relaxation enhancement titration of $\mathbf{Gd_2L^1}$ and $\mathbf{Gd_2L^2}$ measured at 37 ^{0}C and 7T in buffered medium. c) *In vitro* MRI on tube phantoms: $\mathbf{Gd_2L^{1\text{-}2}}$ (2.5 mM Gd^{3+}) without and with 1 equiv. Ca^{2+} (1.2 mM). d) Preparation of the rat for tMCAo. e) Infusion of the SCA in the rat somatosensory cortex (marked red). f) Positioning of the occluder in the pre-ischemia and the reperfusion period (left) or during the ischemia induction (right); the position of occluder is highlighted with a yellow dashed circle. g) Scheme representing the experimental procedure until the end of the reperfusion period.

Fig. 2 Caption.

Molecular fMRI of ischemia with Ca-sensitive MRI probes. a) K-means cluster maps of the responsive $\mathbf{Gd_2L^1}$ infused in the rat somatosensory cortex. b) Hierarchical cluster maps of the responsive $\mathbf{Gd_2L^1}$. c) Detrended signals of the experiments with $\mathbf{Gd_2L^1}$ (left) or $\mathbf{Gd_2L^2}$ (right) with tMCAo induction. d) Average values of detrended signals during the recordings with $\mathbf{Gd_2L^1}$ and $\mathbf{Gd_2L^2}$ with tMCAo induction in the three segments (pre-ischemia, ischemia, post-ischemia).

Supplementary Information for

Early detection and monitoring of cerebral ischemia with calcium-responsive MRI probes

Tanja Savić, Giuseppe Gambino, Vahid Bokharaie, Hamid R. Noori, Nikos K. Logothetis and Goran Angelovski*

Correspondence to: goran.angelovski@tuebingen.mpg.de

Contents

Preparation of Gd_2L^1 and Gd_2L^2

General remarks. Commercially available reagents and solvents were used without further purification. Purification by column chromatography was performed with silica gel 60 (0.03−0.2 mm) from Carl Roth (Germany). ^1H and ^{13}C NMR spectra were recorded on a Bruker Avance III 300 MHz spectrometer at 25 °C. High resolution mass spectra were recorded on a Bruker Daltonics APEX II (FT-ICR-MS) with an electrospray ionization source. The **Gd_2L^1** (Ca-responsive contrast agent) was prepared as previously reported [1]. The synthesis of the **Gd_2L^2 (**non-responsive contrast agent) is illustrated in Scheme 1. Compound **1** was prepared as previously reported [2]. The concentration of Gd^{3+} in analysed solutions was determined using the bulk magnetic susceptibility shift [3].

*Synthesis of **3**.* Compound **2** (0.31 g, 0.82 mmol) was dissolved in acetonitrile (20 mL) in a 50 mL round bottom flask. Potassium carbonate (0.45 g, 3.28 mmol) was then added as a solid to the stirring mixture, followed by a solution of **1** (1.6 g, 1.97 mmol) in acetonitrile (10 mL). The reaction mixture was stirred for 16 hours at 60 °C. The resulting mixture was cooled, the inorganic salts were removed by filtration and the solution was evaporated *in vacuo*. The crude product was purified by column chromatography (silicagel, 0-15% MeOH in CH_2Cl_2) to obtain pure **3** as a yellow oil (530 mg, 35% yield). ^1H NMR ($CDCl_3$, 300 MHz) δ: 1.46 (s, 72H, CH_3), 2.23 (b, 28H, CH_2), 2.86 (b, 26H, CH_2), 3.37-3.71 (b, 30H, CH_2), 7.12-7.18 (b, 4H, CH_{Ar}), 7.56-7.73 (b, 4H, CH_{Ar}); ^{13}C NMR ($CDCl_3$, 125 MHz) δ: 28.0 (CH_3), 35.2 (CH_2Ph), 40.4 (CH_2NH), 48.7 (CH_2N), 51.8 (CH_2N), 55.6 (CH_2COO), 56.3 (CH_2COO), 70.2 (CH_2O), 81.7 (C_qCH_3), 119.7 (CH_{Ar}), 129.3 (CH_{Ar}), 136.0 (C_{Ar}), 169.6 (COO), 171.9 (COO), 172.9 (COO). HRMS-ESI: calculated for $C_{94}H_{161}N_{14}O_{22}Na_2^{3+}$ $[M+H+2Na]^{3+}$: 628.0563, found: 628.0556.

Synthesis of $\boldsymbol{L^2}$. Compound **3** (35 mg, 0.019 mmol) was dissolved in formic acid (5 mL) in a 25 mL round bottom flask and stirred for 16 hours at 55 °C. The reaction mixture was cooled and the solvent was evaporated *in vacuo*. The obtained solid was dissolved in water and the pH adjusted to 7.4. After filtration through a 450 nm PTFE filter, the solution was freeze-dried, providing $\mathbf{L^2}$ as a pale yellow solid in quantitative yield. ^{1}H NMR (D_2O, 300 MHz) δ: 2.74-2.79 (b, 10H, CH_2N), 2.91-3.02 (b, 14H, CH_2N), 3.27 (b, 20H, CH_2), 3.36 (b, 10H, CH_2), 3.47 (b, 10H, CH_2), 3.56-3-73 (b, 12H, CH_2), 7.23-7.26 (b, 4H, CH_{Ar}), 7.38-7.41 (b, 4H, CH_{Ar}); ^{13}C NMR ($CDCl_3$, 125 MHz) δ: 34.1 (CH_2Ph), 39.8 (CH_2NH), 47.9 (CH_2N), 48.3 (CH_2N), 51.1 (CH_2N), 51.7 (CH_2N), 54.6 (CH_2N), 55.2 (CH_2N), 56.2 (CH_2COO), 56.8 (CH_2COO), 59.3 (CH_2COO), 68.3 (CH_2O), 69.4 (CH_2O), 121.5 (CH_{Ar}), 129.8 (CH_{Ar}), 135.0 (C_{Ar}), 136.4 (C_{Ar}), 170.3 (COO), 171.2 (COO), 172.7 (COO), 178.0 (COO), 178.9 (COO). HRMS-ESI: calculated for $C_{62}H_{91}CaK_2N_{14}O_{22}^-$ $[M-5H+Ca+2K]^-$: 1501.5338, found: 1501.5330.

Complexation of $\boldsymbol{L^2}$ *with* Gd^{3+}. Ligand $\mathbf{L^2}$ (26 mg, 0.019 mmol) was dissolved in 5 mL of water in a 10 mL round bottom flask and the pH was adjusted to 7.4. Aqueous $GdCl_3 \cdot 6H_2O$ (14 mg, 0.038 mmol, dissolved in 1 ml of water) was added portion-wise to the stirring mixture, while maintaining the pH at 7.4 with the addition of aqueous NaOH (1 M). The solution was stirred overnight at room temperature. Subsequently, the solution was treated twice with Chelex® to remove any excess Gd^{3+}. The pH was again adjusted to 7.4 and the solution filtered through 0.2 μm filters and freeze dried, obtaining $\mathbf{Gd_2L^2}$ as a white solid in quantitative yield. HRMS-ESI: calculated for $C_{62}H_{88}Gd_2N_{14}O_{22}^{2-}$ $[M-2H]^{2-}$: 848.2345, found: 848.2373.

Relaxometric titrations with Gd_2L^1 and Gd_2L^2

Two solutions of $\mathbf{Gd_2L^{1\text{-}2}}$ with starting [Gd^{3+}] = 1.0 mM ([$\mathbf{Gd_2L^{1\text{-}2}}$] = 0.5 mM) were titrated using a 5 mM $CaCl_2$ solution, measuring longitudinal relaxation T_1 times after every addition with a 7T (300 MHz) Bruker Avance III NMR spectrometer at 37 °C. The T_1 times were obtained using standard inversion recovery with a 1% gradient to eliminate the radiation damping effect. The obtained relaxation times were converted into relaxivities (r_1 values) and plotted as a function of Ca^{2+} concentration normalized to $\mathbf{Gd_2L^{1\text{-}2}}$ concentration (Equiv. Ca^{2+} = [Ca^{2+}] / [$\mathbf{Gd_2L^{1\text{-}2}}$]). The longitudinal relaxivities of $\mathbf{Gd_2L^{1\text{-}2}}$ were determined according to Equation (1), where $T_{1,obs}$ – the determined longitudinal relaxation time, $T_{1,d}$ – the diamagnetic longitudinal relaxation time (T_1 in the absence of complex) and [Gd^{3+}] – the concentration of Gd^{3+} (equal to double the concentration of the complex) used in the experiment.

$$\frac{1}{T_{1,obs}} = \frac{1}{T_{1,d}} + r_1 \times [Gd^{3+}] \qquad (1)$$

Magnetic resonance imaging

MRI measurements were performed on 7T Bruker BioSpec 70/30 USR magnet (software ver. Paravision 5.1), using a Bruker volume coil (RF RES 300 1H 075/040 LIN/LIN TR).

MRI on tube phantoms with $\boldsymbol{Gd_2L^1}$ *and* $\boldsymbol{Gd_2L^2}$. The phantom consisted of 4 capillaries (3 mm diameter, 150 µL volume), containing $\mathbf{Gd_2L^1}$ and $\mathbf{Gd_2L^2}$ (1.25 mM SCA = 2.5 mM Gd^{3+}) with and without [Ca^{2+}] (1.25 mM). MR images where acquired using T_1-weighted imaging (Fast Low Angle Single Shot (FLASH) pulse sequence) with the following parameters: repetition time (TR)=60 ms, echo time (TE)= 2.95 ms, flip angle (FA)= 90 ^{0},

slice thickness 2 mm, field of view (FOV)= 55 x 55 mm^2, matrix size (MTX)= 256 x 256, number of excitations (NEX)= 50, and total acquisition time (TA)= 12 min 48 sec.

MRI with $\boldsymbol{Gd_2L^1}$ *and* $\boldsymbol{Gd_2L^2}$ *in vivo.* MR images were acquired using T_1-weighted (fast low angle shot (FLASH) pulse sequence), diffusion weighted (spin-echo echo-planar pulse sequence) and T_2-weighted imaging (Rapid Acquisition with Refocused Echoes (RARE) pulse sequence).After the localizer scan was performed and region of the $\mathbf{Gd_2L^{1\text{-}2}}$ injection was located, the FLASH pulse sequence was optimized to cover the region of injection. The imaging parameters were: TR/TE=80.95 / 1.56 ms, FA=90 ^{0}, 3 axial slices with 1 mm thickness each, FOV 18 x 20.5 mm^2; MTX 72 x 82, (NEX=3, TA=19s 914 ms. First section of MRI acquisition was divided in three parts: pre-ischemia (~ 21 minutes), ischemia (~ 53 minutes), and reperfusion period (~ 31 minutes) by acquiring T_1-weighted imaging every two minutes. Following that, DWI (TR/TE=2250/43 ms, slice thickness 2 mm, interslice thickness 2.5 mm, FOV=32 x 29.4 mm^2, MTX=128 x 84, δt=4 ms, Δt=17 ms, 3 diffusion directions, b values: 0, 300, 500, 1150, 1400, NEX=10, TA=19 min 30 s) was acquired to confirm the ischemia. Thereafter, the infusion cannula was cut and the diffusion of the agent was monitored for 81 minutes by recording a series of T_1-weighted images as described above. Finally, T_2-weighted images were recorded using: TR/TE= 2386.1 / 38 ms, slice thickness 1mm, FOV=24 x 24 mm^2, MTX 96 x96, NEX 40 and TA 19 min 5 sec.

Animals. The experiments were conducted on male Wistar rats (300 – 340 g, Charles River Laboratories). The animals were housed and maintained in controlled environmental conditions with a 12:12 h light-dark cycle for at least 7 days prior to the experiment, with food and water provided *ad libitum*. In each experiment, the animal was anaesthetized with 2.5 % isoflurane in O_2 (Forene, Abbott, Wiesbaden, Germany) and then kept on 1.5-2.0 % for

maintenance. The body temperature of the animal was maintained at 37.0 ± 0.5 °C with a feedback controlled heat pad (50-7221-F, Harvard Apparatus, MA, US) and was continuously monitored by a rectal probe. All experiments with animals were approved by the local authorities (Regierungspräsidium Tübingen).

Administration of the MRI contrast agents. The animal was placed in the stereotaxic frame (Stoelting Co., IL, US). Craniotomy was performed using a manual drill (ML= 4.7, AP=-0.5) and dura was removed. Anchoring for the infusion cannula of the continuous pump was made with the 2 component dental adhesive (OptiBond™ FL, Kerr) and dental cement (CHARISMA FLOW A1, Heraeus Kulzer GmbH) covering the surface of the skull, except the site of craniotomy. Thereafter, a continuous pump (ALZET® osmotic pump) was placed subcutaneously in the back area and the infusion cannula (3.6 mm depth) was fixed with the dental cement. The excess part of the implanted cannula was cut with a circular drill head.

Preparation of the remote occluding device. The remote occluding device consisted of three main parts: 1) support tubing (PE-160, length 108 cm) with a custom made connector, 2) intra-arterial catheter (PE-50, length 1.5 cm), and 3) occluder (diameter 5-0, length 0.31 mm, 5-6 mm silicone coating, DOCCOL) with its extension (PE-90, length 121 cm). The occluder was fixed with superglue (Loctite 454, Henkel) to the micro tight sleeve (F-183, IDEX Health & Science) that was connected to the extension, and subsequently passed through the support tubing. After the custom made connector and intra-arterial catheter were combined, the occluder was advanced/withdrawn to a desired depth.

Preparation of the remote transient middle cerebral artery occlusion. The rat was repositioned into the MRI bed in supine position. A midline neck incision of approximately 2

cm was made and the right common carotid artery (CCA) bifurcation was exposed. The occipital artery was double ligated (7-0) and dissected. The internal carotid artery (ICA) was isolated rostral until bifurcation with pterygopalatine artery (PPA). CCA and the external carotid artery (ECA) were ligated (7-0) and ICA was temporary clipped. Arteriotomy was carried out on the distal part of CCA and an intra-arterial catheter, filled with heparin, was introduced into the CCA until reaching the ECA/ICA bifurcation, and then fixed with two ligations (4-0). Support tubing was passed through the skin close to neck incision and additionally fixed with tape along the abdomen of the animal. Thereafter, the intra-arterial catheter was connected with support tubing and the occluder was then advanced until the clip positioned on the ICA. After removing the clip, the occluder was quickly advanced until 2 mm after bifurcation with the PPA; subsequently, the ICA was ligated with 7-0 ligature. Lastly, the wound was closed and animal was transferred inside the scanner where the temperature, breathing rate, heart rate and blood oxygen saturation were monitored during the scanning. For the occlusion of the MCA, the end of the occluder extension was remotely advanced for 6-8 mm, until resistance was felt, indicating that the occluder has reached the anterior carotid artery (ACA) and blocked the blood flow from the ACA and posterior carotid artery (PCA) to the MCA. For reperfusion, the occluder was withdrawn by the same length.

Data analysis

Images were scaled and converted to Nifti format. `sinc` interpolation from the `flirt` program in FSL (v 5.0) package was used for motion correction [4]. Motion was estimated from interleaved T_1-weighted images and motion correction was conducted using FSL. The images were reconstructed and analyzed using an in-house software written in python v3.6. In each experiment, T_1-weighted signals were recorded. Only experimental sessions which included corrupted signals caused by technical issues were excluded. The sources of these

technical issues were either malfunction of the scanner or malfunction of the injection apparatus. Subsequently, each set of T_1-weighted signals was normalized to their maximum value. Cluster analyses were performed to define appropriate regions of interest (ROIs). This allows the identification of a representative signal for consistent investigation of spatiotemporal differences among the contrast agents. Thereby, all the voxels in a large neighborhood (up to the size of the whole hemisphere) of the epicenter of injection were considered at first. Subsequently, K-means clustering, as implemented in scikit-learn library, was applied to the normalized signals [5]. K-means algorithm requires the number of clusters as an input. In order to ensure the robustness of the analysis with respect to the choice of parameter *K*, clustering was conducted for *K* ranging from 2 to 10 for all datasets and the results were statistically compared. Thereby, K=2 presented the optimal choice. The regions of interest (ROIs) were then defined using a hierarchical clustering algorithm. The algorithm scheme is as follows:

1. Apply the K-means clustering algorithm with two clusters to all the voxels in the initial mask;
2. Select all the voxels corresponding to the centroid with a larger mean value;
3. Apply K-means with two clusters to the voxels selected in step 2;
4. Choose the voxels corresponding to the centroid with a larger mean value, and use them as our ROI.

The critical advantage of this algorithm is that it identifies ROIs systematically and without *a priori* assumptions on the number of voxels or total mask size. Here, the algorithm leads to ROIs with approximately 66 voxels in all datasets (Mean: 66.3, SD: 23.9). It is noteworthy that in all datasets, the ROI consist of the voxels in connected neighborhood of the epicenter of injection. The average of all the signals in the identified ROI was used as the representative signal for that dataset.

The representative signals obtained from different experiments have slightly different initial slopes. To remove the effects of small differences in the transient behavior of the representative signals while maintaining the possible qualitative differences in the signals during the ischemic period, a detrending algorithm was developed and utilized. The detrending algorithm is comprised by the following steps:

1. Normalization: The representative signals $s(t)$ are normalized to the respective initial values. The new signal $s^*(t)$ represents percentage of changes from the first time-step.
2. Segmentation: The normalized signal ($s^*(t)$) is split along the time-axis into three segments associated with experimental procedures. The first segment $s^*_1(t)$ contains the values corresponding to time-steps from the beginning of the measurement until the onset of ischemia; The second segment $s^*_2(t)$ contains values corresponding to all time-steps during the ischemia; The third segment $s^*_3(t)$ contains all time-steps after the removal of ischemia until the end of measurement.
3. Ignore: Time-series $f(t)$ of identical length as $s^*(t)$ is generated using $s^*_1(t)$ and $s^*_3(t)$, ignoring values from second segment, while keeping the original time-stamps. In other words, $f(t)$ contains data from $s^*(t)$ as if no measurements were done during ischemia while keeping track of time.
4. Interpolation: Cubic splines (i.e. piecewise polynomial functions of degree 3 in variable t) were used to interpolate the non-linear time-series $f(t)$. For this purpose, `splev` function from Scipy library in python [6] was used (smoothing factor of $s=1$) to identify the B-spline representation of all segments of the 1D-curve $f(t)$ including segment 2 ($f_{sp}(t)$). Thereby, the spline function $f_{sp}(t)$ is extrapolated over segment 2 assuming as if it follows the same trend as is inherent in segments 1 and 3.
5. Detrending: The difference $d_s(t)=f_{sp}(t)-s^*(t)$ provides the detrended signal.

For non-ischemic experiments, the detrending procedure is identical to the above algorithm, with the difference that step 3 (ignore) is not performed. The spline function with segment 2 is then based on data from the experiment and not, as in case of ischemia, based on the obtained trends from segments 1 and 3.

References:

1. Angelovski, G. et al. Smart magnetic resonance imaging agents that sense extracellular calcium fluctuations. *ChemBioChem* **9**, 1729-1734 (2008).

2. Connah, L. & Angelovski, G. Synergy of Key Properties Promotes Dendrimer Conjugates as Prospective Ratiometric Bioresponsive Magnetic Resonance Imaging Probes. *Biomacromolecules* **19**, 4668-4676 (2018).

3. Corsi, D.M., Platas-Iglesias, C., van Bekkum, H. & Peters, J.A. Determination of paramagnetic lanthanide(III) concentrations from bulk magnetic susceptibility shifts in NMR spectra. *Magn. Reson. Chem.* **39**, 723-726 (2001).

4. Jenkinson, M., Beckmann, C.F., Behrens, T.E., Woolrich, M.W. & Smith, S.M. FSL. *Neuroimage* **62**, 782-790 (2012).

5. Pedregosa, F. et al. Scikit-learn: Machine Learning in Python. *J. Mach. Learn. Res.* **12**, 2825-2830 (2011).

6. Jones, E., Oliphant, T. & Peterson, P. in http://www.scipy.org/ (2001).

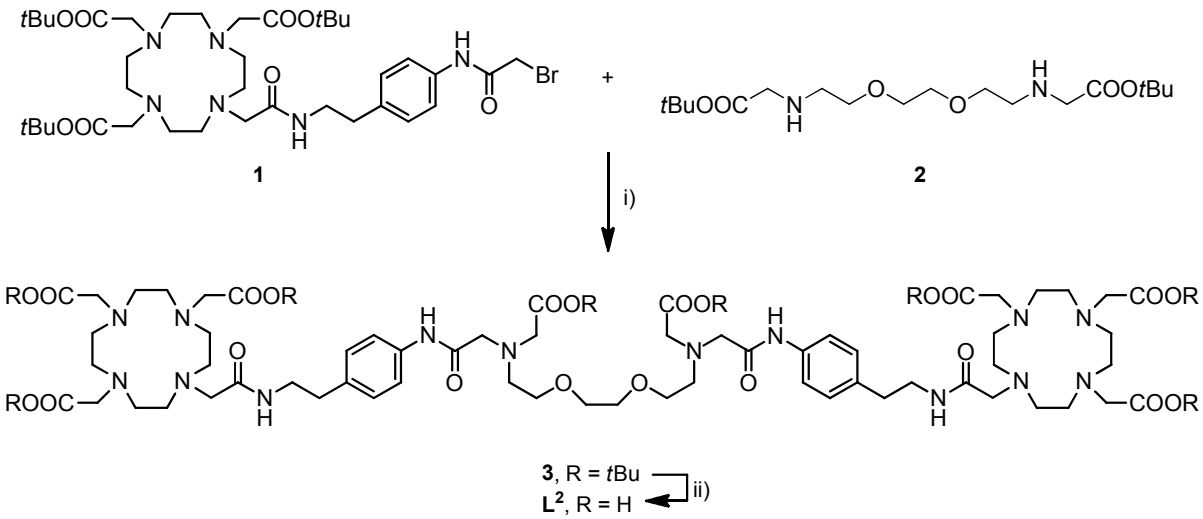

Supplementary Fig. S1.

Synthetic scheme for the preparation of $\mathbf{L^2}$. Reagents and conditions: i) K_2CO_3, MeCN, 60 °C, 16 h; ii) HCOOH, 55 °C, 16 h.

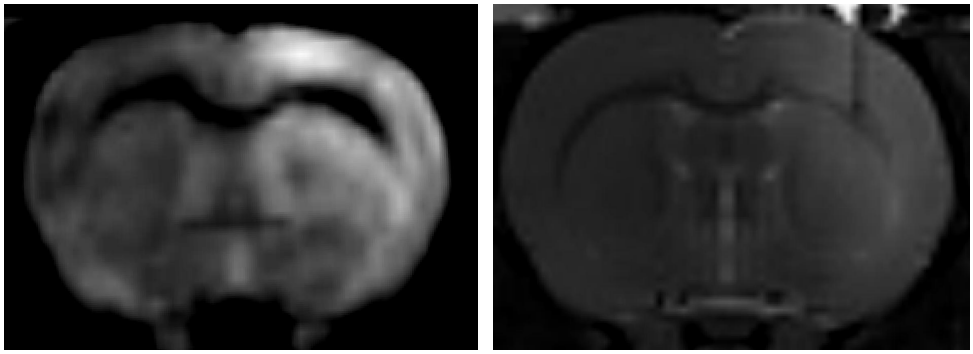

Supplementary Fig. S2.

Confirmation of ischemia. Images acquired after tMCAo performed on the right MCAo. left) Diffusion weighted image right) T_2-weighted image.

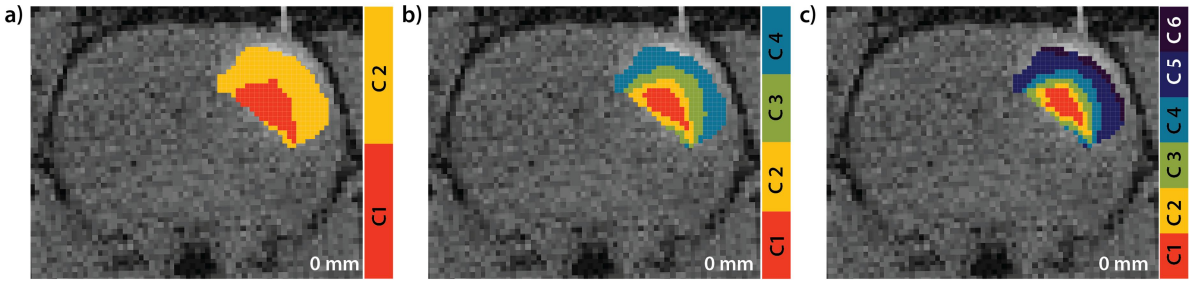

Supplementary Fig. S3.

Comparison of K-means clustering of the responsive $\mathbf{Gd_2L^1}$ infused in the somatosensory cortex. T_1-weighted image overlayed with cluster maps done using cluster numbers of a) 2 b) 4 c) 6.

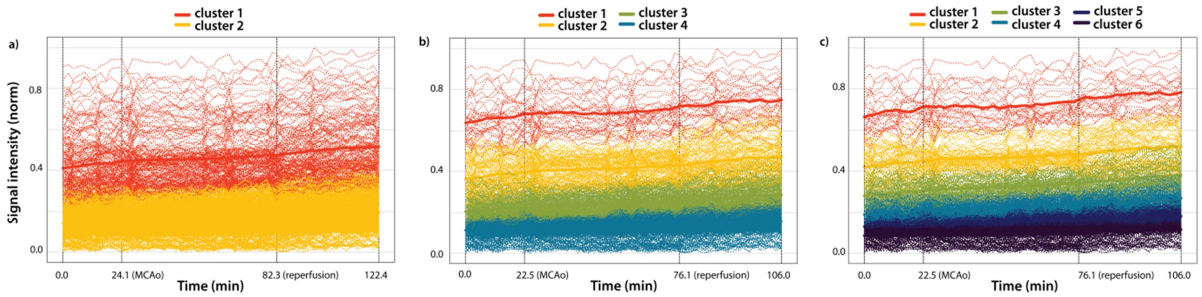

Supplementary Fig. S4.

Centroids and the corresponding signals for cluster maps shown in Figure S3.

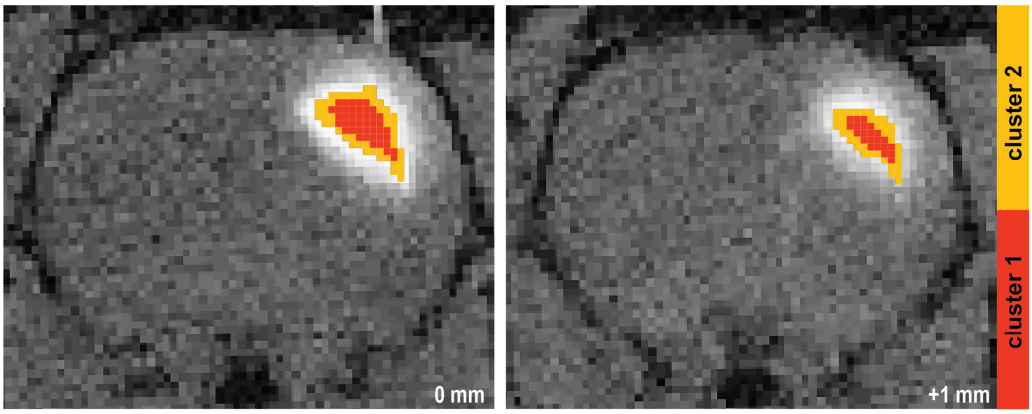

Supplementary Fig. S5.

T_1-weighted image overlayed with hierarchical cluster maps of the responsive $\mathbf{Gd_2L^1}$ infused in the somatosensory cortex. Clustering was performed using two clusters.

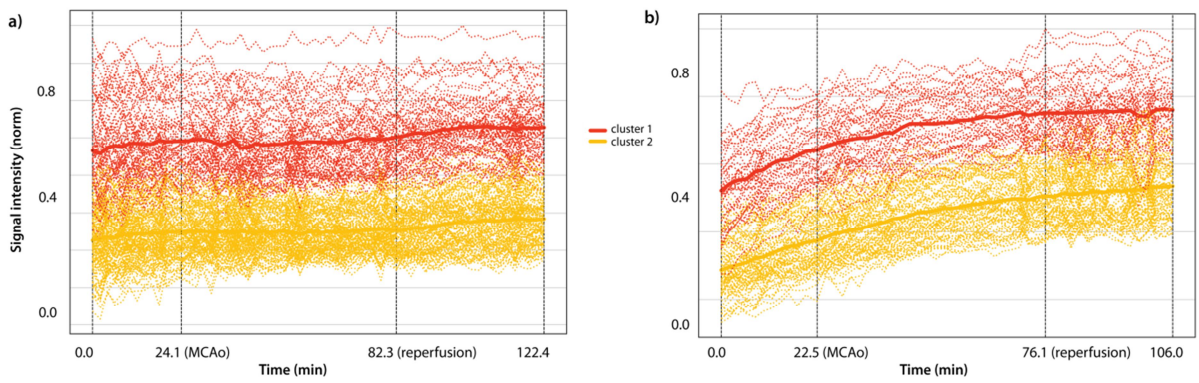

Supplementary Fig. S6.

Centroids and the corresponding signals for cluster maps shown in Figure S5.

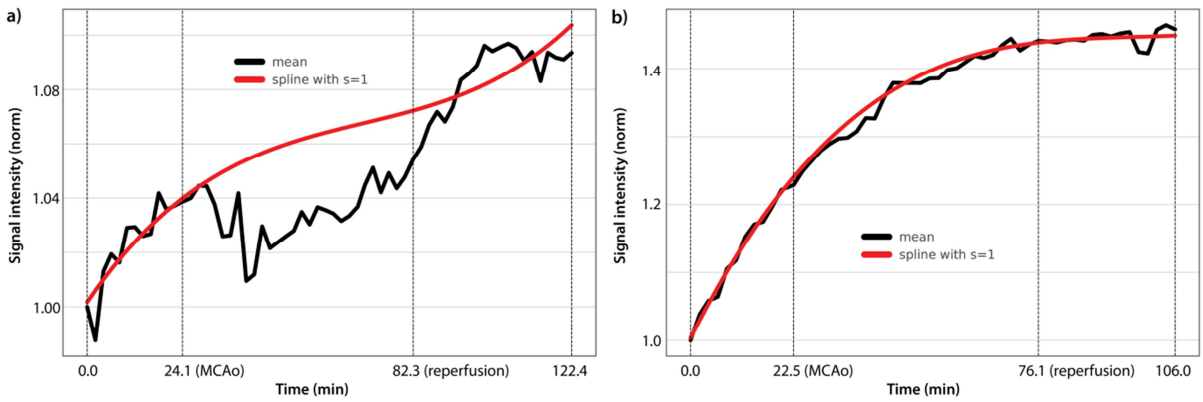

Supplementary Fig. S7.

The procedure of detrending a representative signal. a) $\mathbf{Gd_2L^1}$ b) $\mathbf{Gd_2L^2}$

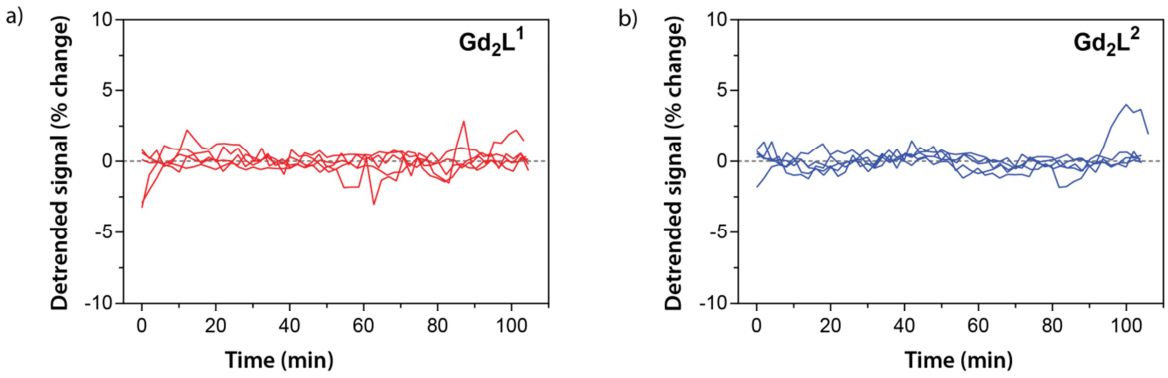

Supplementary Fig. S8.

Detrended signals of selected experiments with **Gd_2L^1** (left) or **Gd_2L^2** (right) without tMCAo induction.

Supplementary Table S1. Gd_2L^1 mean values of detrended signals for experiments with ischemia.

Detrended signal mean **Gd_2L^1**	**Pre-ischemia** (10^{-4})	**Ischemia** (10^{-2})	**Post-ischemia** (10^{-4})
exp 1	4.15	-1.29	-2.18
exp 2	6.17	-2.44	-3.39
exp 3	4.26	-3.29	-3.13
exp 4	4.43	-4.41	-3.55
exp 5	1.98	-1.79	-1.58

Supplementary Table 2. Gd_2L^2 mean values of detrended signals for experiments with ischemia.

Detrended signal mean **Gd_2L^2**	**Pre-ischemia** (10^{-5})	**Ischemia** (10^{-2})	**Post-ischemia** (10^{-5})
exp 1	2.06	-0.10	-1.51
exp 2	-4.21	1.68	3.09
exp 3	-5.39	-0.75	3.95
exp 4	-6.26	-0.23	5.01
exp 5	-5.00	0.34	3.67

ChemComm

COMMUNICATION

View Article Online
View Journal | View Issue

Cite this: *Chem. Commun.*, 2016, 52, 9224

Received 12th May 2016,
Accepted 2nd June 2016

DOI: 10.1039/c6cc04011j

www.rsc.org/chemcomm

Paramagnetic lanthanide chelates for multicontrast MRI†

Nevenka Cakić,[a] Tanja Savić,[a] Janice Stricker-Shaver,[a] Vincent Truffault,[b] Carlos Platas-Iglesias,[c] Christian Mirkes,[d] Rolf Pohmann,[d] Klaus Scheffler*[de] and Goran Angelovski*[a]

The preparation of a paramagnetic chelator that serves as a platform for multicontrast MRI, and can be utilized either as a T_1-weighted, paraCEST or ^{19}F MRI contrast agent is reported. Its europium(III) complex exhibits an extremely slow water exchange rate which is optimal for the use in CEST MRI. The potential of this platform was demonstrated through a series of MRI studies on tube phantoms and animals.

Visualization of various biological processes that take place at cellular and molecular levels is the main goal of modern diagnostic and molecular imaging techniques. Due to different sensitivity, penetration depth, spatial or temporal resolution properties of the available imaging methods, the development of multimodal imaging experienced great advancements in the last decade.[1,2] Nevertheless, a combination of two (or more) techniques is often challenging, requiring integration of different physical phenomena in the common hardware, or careful design of multimodal imaging probes.[3,4]

Today, magnetic resonance imaging (MRI) is one of the most powerful imaging tools capable of displaying an excellent soft tissue contrast and furthermore different types of contrasts. A number of diverse MRI contrast agents can improve the specificity of MRI measurements and, based on their nature, can provide different types of information. The most commonly used ^{1}H-MRI contrast agents are paramagnetic Gd^{3+}-based complexes or superparamagnetic iron-oxide based nanoparticles (T_1- and T_2-shortening agents, respectively).[5] Recently, an entirely different mechanism for altering an MRI contrast, based on chemical exchange saturation transfer (CEST), has been developed. Contrast agents for CEST imaging usually consist of paramagnetic chelates (paraCEST agents) specifically designed to shift the resonances of exchangeable protons (NH, OH or bound water) further away from the bulk water.[6] One of the great advantages of CEST is the detectability of its effect in combination with the presaturation RF pulse; only when this RF is applied at the specific frequency of the exchangeable protons, the MRI contrast will appear. Consequently, this method allows the multi-frequency readout and adjustment of the frequencies (*e.g.* by choice of the group with exchangeable protons or choice of the paramagnetic ion), which can be used for separate detection and visualization of different cellular and tissue environments.[7,8] Finally, MRI can be performed on heteronuclear and hyperpolarized systems.[9] Here, the best choice is ^{19}F NMR because of its high sensitivity, the easy re-tuning of standard MRI instruments from ^{1}H to ^{19}F nuclei, the high natural abundance of the ^{19}F isotope and the absence of background signals from intrinsic biomolecules, thus allowing quantitative studies.[10,11]

With such potential to provide diverse information by employing different frequencies and contrast mechanisms, MRI could be exploited for concurrent studies by means of T_1-weighted, CEST and ^{19}F imaging protocols. To this aim, it is highly desirable to develop multicontrast agents, probes capable of making use of these different types of MR contrast, thus resulting in a set of unique information related to the studied tissue of interest.

We therefore aimed to prepare an agent that is capable of chelating the paramagnetic ion, possesses frequency-shifted protons in slow exchange with bulk water, and finally bears a sufficient number of fluorine atoms to provide a sizeable ^{19}F NMR signal (Fig. 1). We designed ligand **L**, a derivative of DOTA-tetraglycineamide (DOTAM-Gly),[12] which displays CEST properties and ensures good solubility in aqueous solutions, especially after incorporation of fluorine atoms. The fluorinated moieties were introduced in the molecule at *trans* positions of the macrocyclic ring through two CF_3 groups by using a 4-(trifluoromethyl)-L-phenylalanine (*p*-CF_3-Phe) derivative and a convenient six-step

[a] *MR Neuroimaging Agents, Max Planck Institute for Biological Cybernetics, 72076 Tübingen, Germany. E-mail: goran.angelovski@tuebingen.mpg.de*
[b] *Max Planck Institute for Developmental Biology, 72076 Tübingen, Germany*
[c] *Centro de Investigaciones Científicas Avanzadas (CICA) and Departamento de Química Fundamental, Universidade da Coruña, 15008 A Coruña, Spain*
[d] *High-Field Magnetic Resonance, Max Planck Institute for Biological Cybernetics, 72076 Tübingen, Germany. E-mail: klaus.scheffler@tuebingen.mpg.de*
[e] *Department for Biomedical Magnetic Resonance, University of Tübingen, 72076 Tübingen, Germany*

† Electronic supplementary information (ESI) available: Synthetic procedures, descriptions of CEST, ^{19}F NMR, NMR diffusion and MRI experiments. See DOI: 10.1039/c6cc04011j

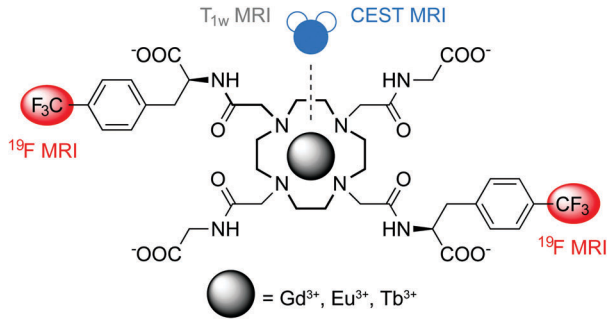

Fig. 1 The chemical structure of chelator **L** described in this work: paramagnetic ion makes it suitable for T_1-weighted or paraCEST MRI, while nearby CF_3 groups enable ^{19}F NMR, concurrently taking advantage of the paramagnetic enhancement effect.

synthetic procedure (ESI†). The resulting molecule **L** underwent complex formation with the Gd^{3+}, Eu^{3+} and Tb^{3+} ions and the properties of **GdL**, **EuL** and **TbL** were further investigated (ESI†). Their overall charge should be advantageous (negative) due to the presence of four carboxylate groups, while appropriate complex stability necessary for *in vivo* experiments is ensured by the kinetic inertness provided by the tetraamide moieties.[13] Finally, rigid benzyl moieties may establish, compared to *e.g.* aliphatic spacers, a well-defined distance of ^{19}F nuclei from the paramagnetic center, thus providing advantageous relaxation properties at the frequency of these nuclei.[14]

The longitudinal relaxivity of **GdL** was calculated by obtaining T_1 values of a series of buffered solutions at different complex concentrations. The resulting value of 3.1 mM^{-1} s^{-1} is expected for monohydrated tetraamide complexes with a slow water exchange rate.[15] CEST measurements were performed by selective presaturation of the **EuL** and **TbL** samples in incremental steps over a range of frequencies followed by plotting the remaining steady-state bulk water signal, M_z/M_0, as a function of saturation frequency (Fig. 2). The resulting Z-spectra of **EuL** exhibited a strong CEST effect (~50% at 25 °C, 15 mM, B_1 = 25.0 μT) centred at 50 ppm relative to bulk water, which is commonly associated with the water molecule directly coordinated to Eu^{3+}. The CEST effect remains strong at 37 °C along with slight broadening and shifting of the CEST signal (5 ppm) towards the bulk water resonance due to the hyperfine shift effect of Eu^{3+} (Fig. 2, top).[16]

Water exchange rates at both temperatures were determined using a concentration-independent method previously developed by Sherry and colleagues,[16] and were confirmed by quantification of the exchange rates as a function of saturation time or saturation power (QUEST and QUESP experiments, respectively).[17] The values obtained from these experiments revealed extremely slow exchange rates of around 1 and 2 kHz or bound-water lifetimes (τ_M) of around 1 ms and 500 μs at 25 and 37 °C, respectively (Table 1). These residence times are as long as those reported very recently for the phosphonate esters of DOTAM-Gly at 25 °C,[18] likely due to the presence of hydrophobic *p*-CF_3-Phe moieties. Consequently, **EuL** displays an almost optimal τ_M which lies in the range of 10^{-4}–10^{-2} s, allowing CEST experiments using weaker B_1 fields. On the other hand, **TbL** displayed a weak CEST effect for both the inner-sphere water molecule and amide

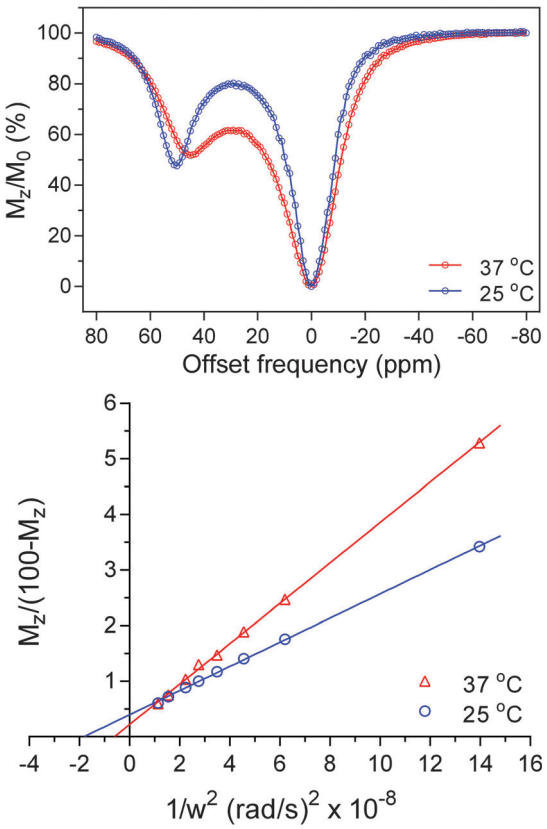

Fig. 2 CEST experiments with **EuL** (15 mM). (top) Z-spectra of **EuL** at B_1 = 25.0 μT and irradiation time = 5 s; (bottom) determination of water exchange rates at 25 °C (blue) and 37 °C (red) at B_1 = 35.0, 30.0, 25.0, 22.5, 20.0, 17.5, 15.0 and 10.0 μT, and irradiation time = 10 s.

Table 1 Water exchange rates (in Hz) obtained for **EuL** using the two independent methods

Temperature	Omega plots	QUEST/QUESP
25 °C	1176 ± 22	930 ± 11
37 °C	2036 ± 110	2000 ± 138

protons (ESI†), probably for the same reasons related to slow water exchange as in **EuL**.[19,20]

^{19}F NMR spectra of **GdL**, **EuL** and **TbL** were recorded and ^{19}F relaxation rates were determined to estimate the potential of these agents for ^{19}F MRI. **GdL** displayed a single broad ^{19}F NMR resonance, indicating substantial shortening of the relaxation times, while **EuL** and **TbL** revealed the existence of at least three paramagnetic species in the solution with different ^{19}F chemical shifts (ESI†). While the two peaks with higher intensities can be assigned to the common monocapped square-antiprismatic and monocapped twisted square-antiprismatic (SAP and TSAP, respectively) isomers of this type of compound,[21] the appearance of the third resonance with very weak intensity can be explained by racemization of the starting amino acid or racemization of alkylating arms prior to or during alkylation of cyclen, as previously observed for similar systems under comparable experimental conditions.[22] Consequently, ^{19}F relaxation rates were determined only for the most abundant peaks (Table 2).

Table 2 ^{19}F relaxation rates of **GdL**, **EuL** and **TbL** (300 MHz, 25 °C)

Temperature	^{19}F R_1 (Hz)	^{19}F R_2 (Hz)
GdL	182	385
EuL	1.4[a,b]	18[a] 19[b]
TbL	32[a] 12[b]	48[a] 28[b]

[a] More abundant isomer. [b] Less abundant isomer.

As expected, **GdL** dramatically affected both ^{19}F R_1 and R_2, while still keeping a favorable R_1/R_2 ratio to obtain a good signal-to-noise ratio (SNR), when using ultrafast sequences.[23] **EuL** and **TbL** also enhanced ^{19}F R_1 and R_2, however the reduction in the R_1/R_2 ratio (in the case of **EuL**) or larger signal splitting (in the case of **TbL**) suggests **GdL** as a better candidate for ^{19}F MRI studies, with the current DOTA-type chelator.

The potential of these systems to serve as multicontrast agents was demonstrated using *in vitro* MRI on tube phantoms (Fig. 3a–d). Four tubes containing **GdL**, **EuL**, **TbL** and water as controls were imaged using a 7T MRI scanner by different imaging protocols and frequencies. The greatest effect on relaxation times and hence the signal enhancement in T_1-weighted MRI experiments was observed for **GdL** (Fig. 3a), as would be expected; this effect was also confirmed by T_2-weighted MRI experiments (Fig. 3b). All three complexes displayed very good ^{19}F MRI contrasts using the sequence parameters adjusted to assume different ^{19}F relaxation rates due to influence of different paramagnetic ions (Fig. 3c). Lastly, only **EuL** exhibited a strong contrast in the CEST MRI experiment (Fig. 3d), as already indicated above in the NMR CEST experiments.

To confirm this platform as a multicontrast MRI agent in a complex environment, we have carried out an MRI study on animals using **GdL** and **EuL**. The contrast agent was injected intracranially into the somatosensory cortex of the anesthetized rats outside the scanner. For **GdL**, the animal was transferred into the scanner, and a very strong T_1-weighted MRI signal was recorded *in vivo* (Fig. 3e). Slow reduction in the MRI signal over a period of a few hours indicated very slow diffusion of **GdL** and its potential interaction with brain tissues. Although a similar behavior was previously observed with aminobisphosphonate-containing contrast agents,[24] it is hard to rationalize this effect with the current chelating platform since its diffusion properties in solution did not indicate any aggregation, *i.e.* the diffusion coefficient corresponded to other monomeric agents of similar size (ESI†).

Additionally, the effect of **EuL** was assessed by means of MRI *ex vivo*. A weak T_1-weigthed MRI contrast was obtained as expected after the animal was euthanized and transferred into the scanner (Fig. 3f). In parallel, a strong CEST contrast (~10% signal change) was successfully obtained at the frequency of the inner-sphere water molecule bound to Eu^{3+} (Fig. 3g), confirming the great potential of **EuL** for further paraCEST studies due to its long τ_M (*vide supra*). In regard to ^{19}F MRI, several imaging sequences were tested on both **GdL** and **EuL**, using non-fluorine containing anesthesia to avoid possible interferences at the fluorine frequency. However, only a slight change in signal intensity could

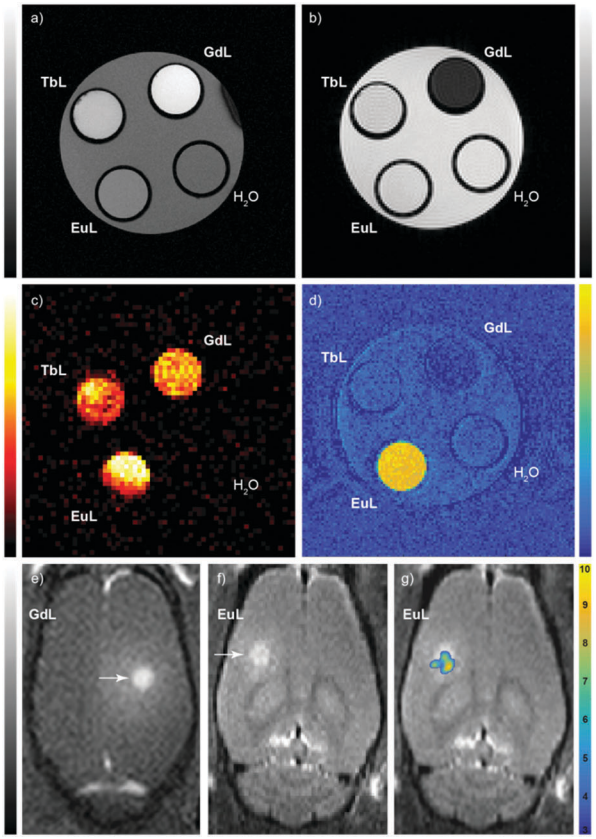

Fig. 3 MRI experiments with the multicontrast agent. *In vitro* MRI on tube phantoms with 5 mM of complexes (pH 7.3, HEPES, 25 °C): (a) T_1-weighted MRI; (b) T_2-weighted MRI; (c) ^{19}F MRI; (d) paraCEST MRI. *In vivo* (**GdL**) and *ex vivo* (**EuL**) MRI in rat cortex: (e) T_1-weighted MRI with **GdL**; (f) T_1-weighted MRI with **EuL**; (g) merged CEST and T_1-weighted MRI with **EuL**. Arrows indicate the region where the contrast agent was injected; bars show signal intensity in arbitrary units except %CEST in (g).

be detected after 2.3 hours of monitoring. As already discussed above, the lack of signals could indicate an interaction of the agent with surrounding tissues, which significantly reduces ^{19}F T_2 relaxation times and leads to signal disappearance (a notable broadening of the ^{19}F signal in the measured 1D spectrum was observed for **GdL**). However, this effect can likely be avoided with another experimental design where the tissue density is lower (*e.g.* in the blood stream or kidneys), or by combining this platform to a nanosized system that will prevent any interaction with the tissue and improve the agent's biocompatibility.[25]

In conclusion, we report a promising platform for the development of multicontrast agents for MRI. A small size molecule accommodates different paramagnetic ions and subsequently enhances ^{1}H T_1-weighted, ^{1}H CEST, and ^{19}F MRI contrasts. The **GdL** and **EuL** complexes can concurrently serve as ^{1}H T_1-weighted and ^{19}F MRI, or as ^{1}H CEST and ^{19}F MRI agents, respectively. As these two complexes are expected to have essentially the same biodistribution, the three different contrast mechanisms could be exploited using the same molecular platform, even if **GdL** and **EuL** have to be administered separately.[26] Furthermore, the installation of the aromatic fluorinated units likely caused extremely advantageous exchange rates in **EuL** for CEST experiments,[20]

while possibly deteriorating the agent's biocompatibility for ^{19}F MRI. Nevertheless, further improvements should easily be envisaged to provide the optimized multicontrast agent. Structural optimizations towards adjustment of the chelator's coordination properties may lead to a single isomer species that will be beneficial for ^{19}F MRI. Synthetic modifications can lead to a higher number of fluorine atoms per molecule to increase the signal intensity, while a combination with various nanocarriers can improve the delivery, biokinetics and potentiality also the T_2 contrast of this multicontrast agent. The ability to collect different types of information from a single imaging probe just by using different imaging protocols brings new quality to MRI and can be a great asset for current molecular imaging to study various biological phenomena.

The authors thank Dr Kai Buckenmaier and Dr Dávid Balla for help in establishing appropriate anesthesia and MRI protocols and the Institute for Organic Chemistry, Faculty of Science, University of Tübingen, for the support in performing MS and elemental analyses. The financial support of the Max-Planck Society, the German Academic Exchange Service (DAAD, PhD fellowship to T.S.) and Ministerio de Economía y Competitividad (CTQ2013-43243-P and CTQ2015-71211-REDT, support to C. P.-I.) is gratefully acknowledged.

The animal experiments were approved by the local authorities (Regierungspraesidium), and were in compliance with the guidelines of the European directive (2010/63/EU) for the care and protection of animals used for scientific purposes.

Notes and references

1 R. Weissleder and M. J. Pittet, *Nature*, 2008, **452**, 580–589.
2 H. Kobayashi, M. R. Longmire, M. Ogawa and P. L. Choyke, *Chem. Soc. Rev.*, 2011, **40**, 4626–4648.
3 S. R. Cherry, *Annu. Rev. Biomed. Eng.*, 2006, **8**, 35–62.
4 A. Y. Louie, *Chem. Rev.*, 2010, **110**, 3146–3195.
5 P. Caravan, in *Molecular and cellular MR imaging*, ed. M. M. J. Modo and J. W. M. Bulte, CRC Press, Taylor & Francis Group, Boca Raton, London, New York, 2007, pp. 13–36.
6 A. D. Sherry and M. Woods, *Annu. Rev. Biomed. Eng.*, 2008, **10**, 391–411.
7 S. Aime, C. Carrera, D. D. Castelli, S. G. Crich and E. Terreno, *Angew. Chem., Int. Ed.*, 2005, **44**, 1813–1815.
8 S. Viswanathan, S. J. Ratnakar, K. N. Green, Z. Kovacs, L. M. De Leon-Rodriguez and A. D. Sherry, *Angew. Chem., Int. Ed.*, 2009, **48**, 9330–9333.
9 E. Terreno, D. D. Castelli, A. Viale and S. Aime, *Chem. Rev.*, 2010, **110**, 3019–3042.
10 I. Tirotta, V. Dichiarante, C. Pigliacelli, G. Cavallo, G. Terraneo, F. B. Bombelli, P. Metrangolo and G. Resnati, *Chem. Rev.*, 2015, **115**, 1106–1129.
11 M. Srinivas, A. Heerschap, E. T. Ahrens, C. G. Figdor and I. J. M. d. Vries, *Trends Biotechnol.*, 2010, **28**, 363–370.
12 S. Aime, A. Barge, D. Delli Castelli, F. Fedeli, A. Mortillaro, F. U. Nielsen and E. Terreno, *Magn. Reson. Med.*, 2002, **47**, 639–648.
13 E. Brücher, G. Tircsó, Z. Baranyai, Z. Kovács and A. D. Sherry, *The Chemistry of Contrast Agents in Medical Magnetic Resonance Imaging*, John Wiley & Sons, Ltd, 2013, pp. 157–208.
14 P. Harvey, I. Kuprov and D. Parker, *Eur. J. Inorg. Chem.*, 2012, 2015–2022.
15 S. Aime, A. Barge, J. I. Bruce, M. Botta, J. A. K. Howard, J. M. Moloney, D. Parker, A. S. de Sousa and M. Woods, *J. Am. Chem. Soc.*, 1999, **121**, 5762–5771.
16 W. T. Dixon, J. M. Ren, A. J. M. Lubag, J. Ratnakar, E. Vinogradov, I. Hancu, R. E. Lenkinski and A. D. Sherry, *Magn. Reson. Med.*, 2010, **63**, 625–632.
17 M. T. McMahon, A. A. Gilad, J. Y. Zhou, P. Z. Sun, J. W. M. Bulte and P. C. M. van Zijl, *Magn. Reson. Med.*, 2006, **55**, 836–847.
18 W. S. Fernando, A. F. Martins, P. Zhao, Y. Wu, G. E. Kiefer, C. Platas-Iglesias and A. D. Sherry, *Inorg. Chem.*, 2016, **55**, 3007–3014.
19 X. J. Wang, Y. K. Wu, T. C. Soesbe, J. Yu, P. Y. Zhao, G. E. Kiefer and A. D. Sherry, *Angew. Chem., Int. Ed.*, 2015, **54**, 8662–8664.
20 A. D. Sherry and Y. K. Wu, *Curr. Opin. Chem. Biol.*, 2013, **17**, 167–174.
21 J. A. Peters, K. Djanashvili, C. F. G. C. Geraldes and C. Platas-iglesias, *The Chemistry of Contrast Agents in Medical Magnetic Resonance Imaging*, John Wiley & Sons, Ltd, 2013, pp. 209–276.
22 T. Mani, A. C. L. Opina, P. Y. Zhao, O. M. Evbuomwan, N. Milburn, G. Tircso, C. Kumas and A. D. Sherry, *JBIC, J. Biol. Inorg. Chem.*, 2014, **19**, 161–171.
23 F. Schmid, C. Höltke, D. Parker and C. Faber, *Magn. Reson. Med.*, 2013, **69**, 1056–1062.
24 I. Mamedov, S. Canals, J. Henig, M. Beyerlein, Y. Murayama, H. A. Mayer, N. K. Logothetis and G. Angelovski, *ACS Chem. Neurosci.*, 2010, **1**, 819–828.
25 K. J. Thurecht, I. Blakey, H. Peng, O. Squires, S. Hsu, C. Alexander and A. K. Whittaker, *J. Am. Chem. Soc.*, 2010, **132**, 5336–5337.
26 A. M. Funk, V. Clavijo Jordan, A. D. Sherry, S. J. Ratnakar and Z. Kovacs, *Angew. Chem., Int. Ed.*, 2016, **55**, 5024–5027.

Electronic Supplementary Information

Paramagnetic lanthanide chelates for multicontrast MRI

Nevenka Cakić,[a] Tanja Savić,[a] Janice Stricker-Shaver,[a] Vincent Truffault,[b] Carlos Platas-Iglesias,[c] Christian Mirkes,[d] Rolf Pohmann,[d] Klaus Scheffler[d,e,*] and Goran Angelovski[a,*]

[a] MR Neuroimaging Agents, Max Planck Institute for Biological Cybernetics, Tübingen, Germany
[b] Max Planck Institute for Developmental Biology, Tübingen, Germany.
[c] Departamento de Química Fundamental, Universidade da Coruña, A Coruña, Spain.
[d] High-Field Magnetic Resonance, Max Planck Institute for Biological Cybernetics, Tübingen, Germany
[e] Department for Biomedical Magnetic Resonance, University of Tübingen, Tübingen, Germany

* Corresponding authors: klaus.scheffler@tuebingen.mpg.de, goran.angelovski@tuebingen.mpg.de

Contents

1. Synthetic procedures

General remarks. Commercially available reagents and solvents were used without further purification. 4-(trifluoromethyl)-L-phenylalanine (*p*-CF_3-Phe) was purchased from PepTech Corporation (Bedford, USA, Cat. No. AL224), while 1,7-bis(benzyloxycarbonyl)-1,4,7,10-tetraazacyclododecane (**3**) was prepared according to previously reported procedure.[1] Purification of the synthesized compounds was performed using silica gel 60 (0.03–0.2 mm) from Carl Roth (Germany). All NMR spectra were acquired on a Bruker Avance III 300 MHz, processed using TopSpin 2.1 (Bruker GmbH), and analyzed with TopSpin 2.1 or ACD/SpecManager 9.0 (Advanced Chemistry Development, Inc.). The concentration of the complexes was determined using the bulk magnetic susceptibility shift (BMS).[2] Elemental analyses were performed on EuroEA 3000 Elemental Analyser (EuroVector SpA, Italy).

Optical rotations were performed on a Jasco P-1020 polarimeter. ESI-HRMS were performed on a Bruker BioApex II ESI-FT-ICR, equipped with an Agilent ESI-Source, measured via flow injection analysis. ESI-LRMS were performed on an ion trap SL 1100 system (Agilent, Germany). The synthetic procedure to obtain **L** is shown in the Scheme S1 with chemical structures of only the predominant macrocyclic S,S-stereoisomer.

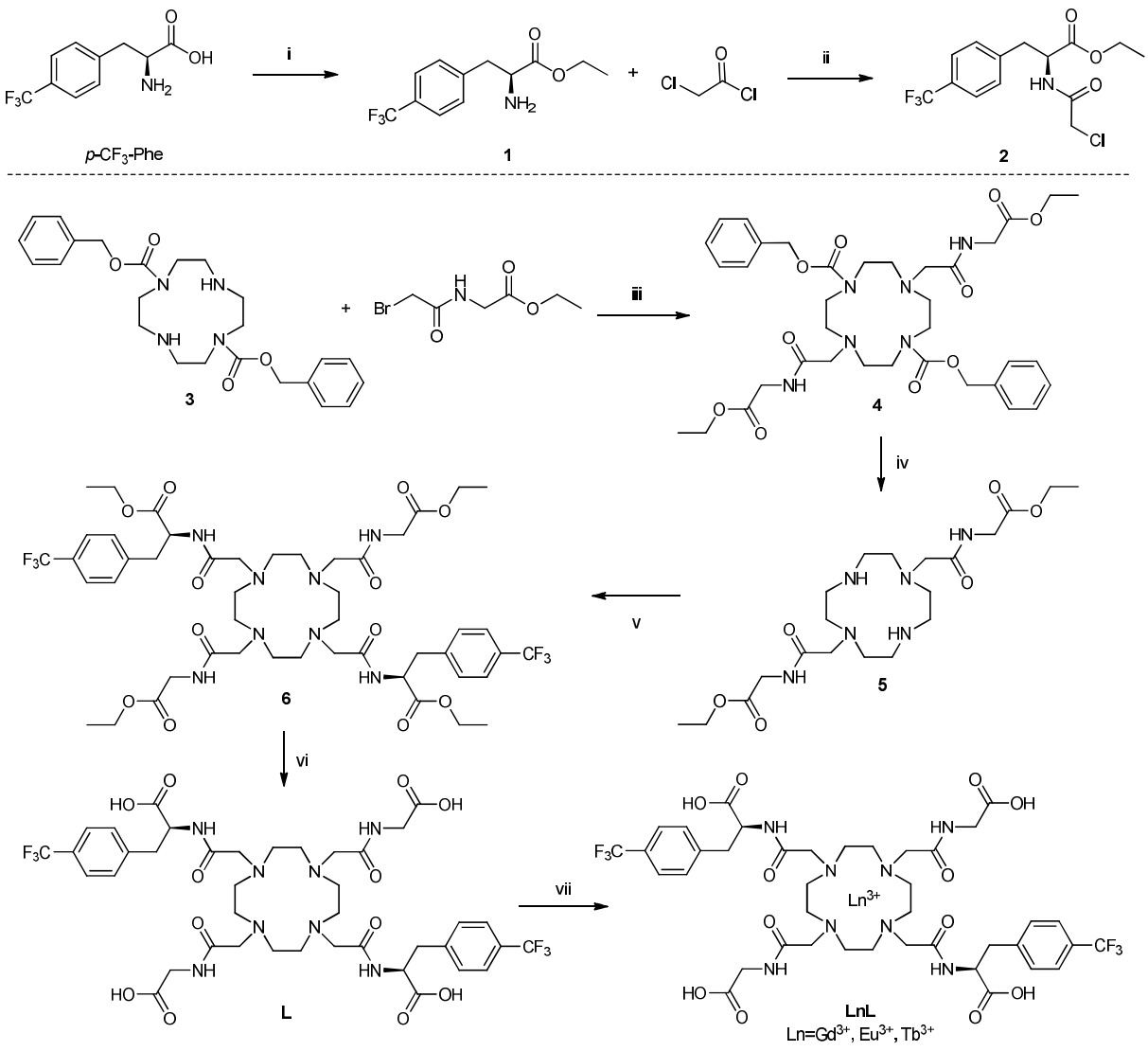

Scheme S1. Synthesis of the ligand **L** and complexes **LnL**. Reagents and conditions: i) $SOCl_2$, EtOH, 5-70 °C, 89 %. ii) Na_2CO_3, DMF, RT, 91 %. iii) K_2CO_3, CH_3CN, 70 °C, 67 %. iv) H_2, Pd/C, EtOH, RT, 91%. v) **2**, K_2CO_3, KI, 70 °C, 59 %. vi) NaOH, THF, RT, 94 %. vii) $LnCl_3$, NaOH, RT, 48 h.

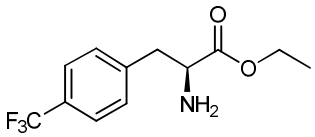

(S)-2-Amino-3-(4-trifluoromethyl-phenyl)-propionic acid ethyl ester (1). The (S)-2-amino-3-(4-(trifluoromethyl)phenyl)propanoic acid (1.70 g, 7.29 mmol) was suspended in ethanol (10 ml), and cooled to 5 °C. Thionyl chloride (3 ml) was added slowly to the suspension over a period of 20 min, and the reaction mixture was then heated on the oil bath at 70 ^{o}C for 5 hours. After cooling of the reaction mixture, the excess of thionyl chloride and ethanol were removed by rotary evaporation. The product was recrystallized from the ethanol-ether mixture to provide the hydrochloride salt of **1** (1.94 g, 89 %) as a colorless solid.

^{1}H NMR (300 MHz, D_2O): δ (ppm) 7.66 (d, *J*=7.7 Hz, 2 H), 7.40 (d, *J*=7.9 Hz, 2 H), 4.39 (t, *J*=6.8 Hz, 1 H), 4.20 (q, *J*=7.2 Hz, 2 H), 3.30 (d, *J*=7.0 Hz, 2 H), 1.15 (t, *J*=7.2 Hz, 3 H). **^{13}C{^{1}H} NMR (75 MHz, D_2O)**: δ (ppm) 169.3, 138.2, 130.0 129.4 (q, *J*=32.5 Hz), 125.9 (q, *J*=3.5 Hz), 124.2 (q, *J*=271.6 Hz), 63.6, 53.8, 39.5, 13.1. **^{19}F{^{1}H} NMR (282 MHz, D_2O)**: δ (ppm) -62.3. **EA**: for $C_{12}H_{14}F_3NO_2$·HCl (297.7 g/mol), calcd: C: 48.4%, H: 5.1%, N: 4.7%, found: C: 48.4%, H: 5.0%, N: 4.6%. $[\alpha]_D^{25}$ +4.102 (c 1.00, H_2O). **MP**: 209-211 ^{o}C. **ESI-LRMS**: for $C_{12}H_{15}F_3NO_2^+$ $[M+H]^+$: *m/z* calcd. 262.1, found 262.1.

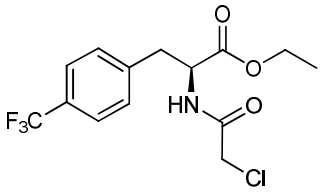

(S)-2-(2-Chloro-acetylamino)-3-(4-trifluoromethyl-phenyl)-propionic acid ethyl ester (2). Sodium carbonate (380 mg, 3.59 mmol) was added to a suspension of (S)-ethyl 2-amino-3-(4-(trifluoromethyl)phenyl)propanoate hydrochloride (534 mg, 1.79 mmol) in dry DMF (2 mL). The mixture was stirred for 30 min at room temperature followed by dropwise addition (over a 1 min period) of chloroacetyl chloride (0157 ml, 223 mg, 1.97 mmol). The mixture was then further stirred for 1 h at room temperature after which time it was diluted with brine (50 mL) and extracted with EtOAc (2· 30 mL). The combined organic extracts were washed with brine (2×50 mL), dried, and concentrated. The crude product was purified by column chromatography (silicagel, EtOAc/hexane from 1:9 to 3:7) to give ethyl 2-(2-

chloroacetamido)-3-(4-(trifluoromethyl)phenyl)propanoate (550 mg, 91 %) as a colorless solid. The analytical sample was prepared after recrystallization from CH_2Cl_2: *n*-hexane.

^{1}H NMR (300 MHz, $CDCl_3$), δ (ppm): 7.56 (d, *J*=8.1 Hz, 2 H), 7.27 (d, *J*=7.9 Hz, 2 H), 7.07 (d, 1 H), 4.88 (dt, *J*=7.7, 6.0 Hz, 1 H), 4.19 (q, *J*=7.2 Hz, 2 H), 4.03 (s, 2 H), 3.25 (dt, *J*=7.7, 6.0 Hz, 1 H), 3.18 (dt, *J*=7.7, 6.0 Hz, 1 H), 1.24 (t, *J*=7.2 Hz, 3 H). **^{13}C{^{1}H} NMR (75 MHz, $CDCl_3$)**: δ (ppm) 170.5, 165.7, 139.8, 129.7, 129.5 (q, *J*=32.5 Hz), 125.5 (q, *J*=3.5 Hz), 124.1 (q, *J*=271.8 Hz), 62.0, 53.3, 42.3, 37.7, 14.0. **^{19}F{^{1}H} NMR (282 MHz, $CDCl_3$)**: δ (ppm) -62.5. **EA**: for $C_{14}H_{15}ClF_3NO_3$ (337.72 g/mol), calcd: C: 49.8%, H: 4.5%, N: 4.1%, found: C: 49.5%, H: 4.5%, N: 4.0%. $[\alpha]_D^{25}$ +37.151 (c=1.00, CH_2Cl_2). **MP**: 74-76 °C. **ESI-LRMS**: for $C_{14}H_{16}ClF_3NO_3^+$ $[M+H]^+$: *m/z* calcd. 338.1, found 338.1.

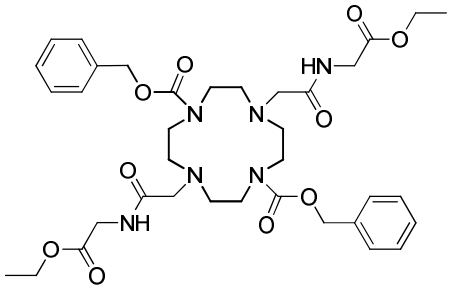

4,10-Bis-[(ethoxycarbonylmethyl-carbamoyl)-methyl]-1,4,7,10tetraaza-cyclododecane-1,7-dicarboxylic acid dibenzyl ester (4). Macrocycle **3** (2.52 g, 5.72 mmol) was dissolved in acetonotrile (40 ml) and K_2CO_3 (3.79 g, 27.5 mmol) was added. The suspension was stirred for 15 min and then ethyl 2-(2-bromoacetamido)acetate (3.08 g, 13.73 mmol) in acetonotrile (10 ml) was added dropwise. The reaction mixture was heated at 70 °C for 18 hours. After cooling, the mixture was filtered, the solvent removed by rotary evaporation and the crude product was purified by column chromatography (silicagel, 4% MeOH in CH_2Cl_2) to give the desired product (2.785 g, 67%) as a yellow oil.

^{1}H NMR (300 MHz, $CDCl_3$): δ (ppm) 7.25 (s, 10 H), 5.02 (s, 4 H), 4.07 (q, *J*=7.1 Hz, 4 H), 3.84 (br. s., 4 H), 3.51-3.28 (br., 8 H), 3.14 (br. s., 4 H), 2.88-2.64 (br., 8 H), 1.17 (t, *J*=7.2 Hz, 6 H). **^{13}C{^{1}H} NMR (75 MHz, $CDCl_3$)**: δ (ppm) 171.3, 169.7, 156.9, 136.5, 128.6, 128.3, 128.2, 67.4, 61.2, 58.3, 55.2, 55.0, 48.5, 48.0, 40.9, 14.2. **ESI-HRMS**: for $C_{36}H_{51}N_6O_{10}^+$ $[M+H]^+$: *m/z* calcd. 727.3661, found 727.3661.

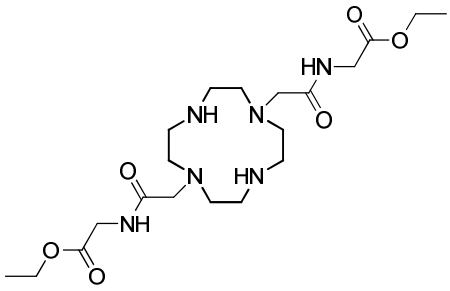

(2-{7-[(Ethoxycarbonylmethyl-carbamoyl)-methyl]-1,4,7,10tetraaza-cyclododec-1-yl}-acetylamino)-acetic acid ethyl ester (5). The macrocycle GA401 (2.414 g, 3.32 mmol) was dissolved in EtOH (50 ml) and 10% $Pd(OH)_2$ on carbon (500 mg) was added. The mixture was shaken for 18 hours under a hydrogen atmosphere (2.5 bar) in a Parr hydrogenator apparatus. The catalyst was removed by filtration through the cake of celite and the filtrate was concentrated to obtain the amine product (1.39 g, 91%) as a yellow oil.

^{1}H NMR (300 MHz, $CDCl_3$): δ (ppm) 8.06 (br. s., 2 H), 4.93 (br. s., 2 H), 4.17 (q, *J*=7.2 Hz, 4 H), 4.02 (br. s., 4 H), 3.29 (s, 4 H), 2.93-2.69 (m, 16 H), 1.27 (t, *J*=7.2 Hz, 6 H). **^{13}C{^{1}H} NMR (75 MHz, $CDCl_3$)**: δ (ppm) 171.8, 170.5, 61.3, 60.3, 52.8, 46.5, 40.9, 14.1. **ESI-HRMS**: for $C_{20}H_{39}N_6O_6^+$ $[M+H]^+$: *m/z* calcd. 459.2926, found 459.2929.

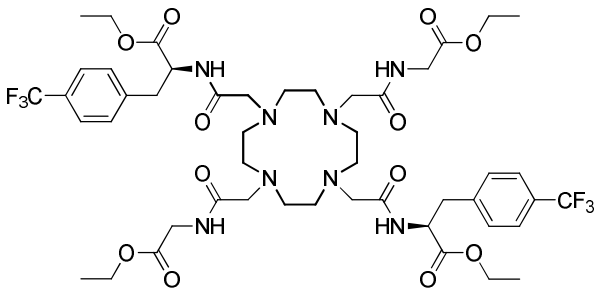

(S,S)-2-[2-(4,10-Bis-[(ethoxycarbonylmethyl-carbamoyl)-methyl]-7-{[1-ethoxycarbonyl-2-(4-trifluoromethyl-phenyl)-ethylcarbamoyl]-methyl}-1,4,7,10tetraaza-cyclododec-1-yl)-acetylamino]-3-(4-trifluoromethyl-phenyl)-propionic acid ethyl ester (6).

The macrocyclic secondary amine (409 mg, 0.892 mmol) was dissolved in acetonitrile (30 ml). K_2CO_3 (542 mg, 3.92 mmol) and KI (99 mg, 0.596 mmol) were added and the reaction mixture was stirred for 30 min. The solution of (S)-ethyl 2-(2-chloroacetamido)-3-(4-(trifluoromethyl)phenyl)propanoate in acetonitrile (10 ml) was added dropwise and the mixture was heated at 70 °C for 18 hours under a nitrogen atmosphere. Upon reaction completion, the solids were removed by filtration, the solvent was evaporated by rotary

evaporation and the residue was purified by column chromatography (silicagel, 3-5% gradient of MeOH in CH_2Cl_2) to give the product (555 mg, 59%) as an off-white amorphous solid.

^{1}H NMR (300 MHz, $CDCl_3$): δ (ppm) 7.56 (d, *J*=8.1 Hz, 4 H), 7.42 (d, *J*=7.9 Hz, 4 H), 7.33 (d, *J*=8.3 Hz, 2 H), 7.29 (t, *J*=4.8 Hz, 2 H), 4.82 (dt, *J*=7.2, 7.1 Hz, 2 H), 4.11 (q, *J*=7.1 Hz, 8 H), 3.95 (d, *J*=3.6 Hz, 4 H), 3.19 (br. s., 8 H), 3.13-2.87 (broad, 4 H), 2.11 - 2.70 (broad, 16 H), 1.22 (t, *J*=7.2 Hz, 6 H), 1.20 (t, *J*=7.2 Hz, 6 H). **^{13}C{^{1}H} NMR (75 MHz, $CDCl_3$)**: δ (ppm) 172.0, 171.4, 171.1, 170.0, 141.3, 130.1, 129.0 (q, *J*=32.2 Hz), 125.3 (q, *J*=3.5 Hz), 124.2 (q, *J*=271.8 Hz), 61.6, 61.5, 57.6, 56.5, 53.4, 50.7 (br), 41.0, 37.4, 14.1. **^{19}F{^{1}H} NMR (282 MHz, $CDCl_3$)**: δ (ppm) -62.1. $[\alpha]_D^{25}$ +8.366 (c=1.00, CH_2Cl_2). **ESI-HRMS**: for $C_{48}H_{66}F_6N_8NaO_{12}^+$ $[M+Na]^+$: *m/z* calcd. 1083.4597, found 1083.4606.

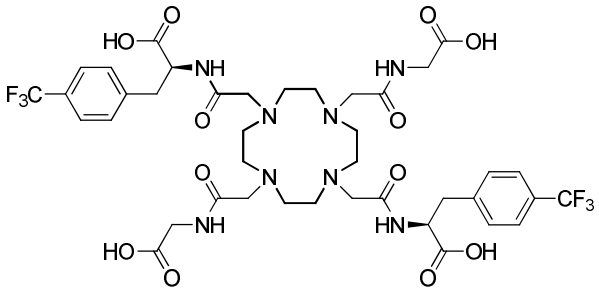

(S,S)-2-[2-(4,10-Bis-[(carboxymethyl-carbamoyl)-methyl]-7-{[1-carboxy-2-(4-trifluoromethyl-phenyl)-ethylcarbamoyl]-methyl}-1,4,7,10tetraaza-cyclododec-1-yl)-acetylamino]-3-(4-trifluoromethyl-phenyl)-propionic acid (L).

A solution of NaOH (2.0 M, ~ 1 ml) was added to a solution of tetraehtyl ester (450 mg, 0.424 mmol) in THF (1 ml) until pH 12 was reached. The mixture was vigorously stirred for 4 h at room temperature while adding NaOH to maintain pH. After reaction completion, THF was removed by rotary evaporation and the pH of the remaining aqueous solution was adjusted to 2 with HCl (1 M). The water was removed by rotary evaporation and the solid residue was triturated with EtOH to dissolve the product. The remaining solid (NaCl) was removed by filtration and the filtrate was evaporated to give the pure product (380 mg, 94%) as yellow amorphous solid.

^{1}H NMR (300 MHz, CD_3OD): δ (ppm) 7.65 (d, *J*=7.9 Hz, 4 H), 7.51 (d, *J*=7.7 Hz, 4 H), 4.84 (br. s., 2 H), 4.07-3.83 (broad, 8 H), 3.73-2.98 (broad, 24 H). **^{13}C{^{1}H} NMR (75 MHz, CD_3OD)**: δ (ppm) 173.7, 172.9, 143.1, 131.3, 130.1 (q, *J*=32.2 Hz), 126.4 (q, *J*=3.5 Hz),

125.8 (q, *J*=271.8 Hz), 56.8, 56.0, 55.0, 42.1, 38.2. **$^{19}F\{^{1}H\}$ NMR (282 MHz, $CDCl_3$)**: δ (ppm) -63.6. $[\alpha]_D^{25}$ +10.547 (c 1.00, CH_3OH). **ESI-HRMS**: for $C_{40}H_{49}F_6N_8O_{12}^-$ [M-H]$^-$: *m/z* calcd. 947.3380, found 947.3396.

General procedure for the preparation of Ln^{3+} complexes: The Ln^{3+} complexes of **L** were prepared by mixing the ligand with the respective $LnCl_3$ salt in slight excess. The solution was stirred at RT for 48 h. The pH value was adjusted to 7.0–7.5 using NaOH (1 M). After 48 h, the mixture was stirred for 24 h at RT in presence of Chelex 100, maintaining the pH at 7.0-7.5, using HCl (1 M). The absence of free Ln^{3+} was verified by colorimetric assay using xylenol orange.[3]

Gadolinium complex, **GdL**: Obtained from **L** (30 mg, 0.032 mmol) and $GdCl_3 \cdot 6H_2O$ (1.2 equiv.) in quantitative yield. ESI-LRMS: for $C_{40}H_{46}F_6N_8O_{12}Gd^-$ [M-4H]$^-$: calc. 1102.2, found 1102.3.

Europium complex, **EuL**: Obtained from **L** (30 mg, 0.032 mmol) and $EuCl_3 \cdot 6H_2O$ (1.2 equiv.) in quantitative yield. ESI-LRMS: for $C_{40}H_{46}F_6N_8O_{12}Eu^-$ [M-4H]$^-$: calc. 1097.2, found 1097.2.

Terbium complex, **TbL**: Obtained from **L** (30 mg, 0.032 mmol) and $TbCl_3 \cdot 6H_2O$ (1.2 equiv.) in quantitative yield. ESI-LRMS: for $C_{40}H_{46}F_6N_8O_{12}Tb^-$ [M-4H]$^-$: calc. 1103.2, found 1103.3.

2. CEST NMR experiments

All CEST NMR experiments were recorded on a Bruker Avance III 300 MHz NMR spectrometer. The saturation transfer experiments were carried out at 25 ^oC or 37 ^oC by irradiating the sample at increments of 1 ppm, with 10% D_2O in H_2O to lock the deuterium frequency. Spectra were measured by recording the bulk water signal intensity as a function of the presaturation frequency.

For the concentration-independent (‘omega plots') and QUESP methods, data was collected by varying the saturation power whilst the saturation time remained constant (10 s and 3 s for

the omega plots and QUESP, respectively). The saturation field strengths varied between 425 and 1490 Hz, for the omega plots: 10, 12.5, 15, 17.5, 20, 22.5, 25, 30 and 35 μT; for QUESP: 10, 15, 17.5, 20, 22.5, 25, 27.5, 30 and 35 μT. For the QUEST experiments, data was collected by varying the saturation time and keeping the power constant (25 μT). The saturation times were 0.25, 0.5, 0.75, 1, 1.5, 2, 3, 4, 5, 7.5 and 10 s. The QUEST and QUESP data were both fitted analytically with Scientist® 3.0 (Micromath, USA) using the previously published method (Eqs. 1 - 4), where χ_{CA} – the fractional concentration of the exchangeable protons of the contrast agent, t_{sat} the saturation time, α – the saturation efficiency, k_{ex} – the rate of proton exchange, $R_{1,2s}$ – the longitudinal and transverse relaxation rates during saturation of the solute, $R_{1,2w}$ – the longitudinal and transverse relaxation rates during saturation of the bulk water, ω_1 – the saturation power, M_s – the MR signal of bulk water after applying RF saturation pulse at the resonance frequency of exchangeable protons of contrast agent (ν_{CEST}) and M_o – the reference MR signal ($-\nu_{CEST}$).[4] The plots in the Figure S1 show the experimental points from QUEST and QUESP experiments and fitted curves with the following fixed parameters at 25/37 °C: R_{1w}=0.299/0.228 s^{-1}, R_{2w}=0.495/0.354 s^{-1}, obtained in independent experiments (inversion recovery and Car-Purcell-Meiboom-Gill experiment for R_{1w} and R_{2w}, respectively).

$$1-\frac{M_s}{M_o}=\frac{k_{ex}\times\alpha\times\chi_{CA}}{R_{1w}+k_{ex}\times\chi_{CA}}\times\left[1-e^{-(R_{1w}+k_{ex}\times\chi_{CA})\times t_{sat}}\right] \qquad (1)$$

$$\alpha=\frac{\omega_1^2}{\omega_1^2+p\,q} \qquad (2)$$

$$p=R_{2s}+k_{ex}-\frac{k_{ex}^2\times\chi_{CA}}{R_{2w}+k_{ex}\times\chi_{CA}} \qquad (3)$$

$$q=R_{1s}+k_{ex}-\frac{k_{ex}^2\times\chi_{CA}}{R_{1w}+k_{ex}\times\chi_{CA}} \qquad (4)$$

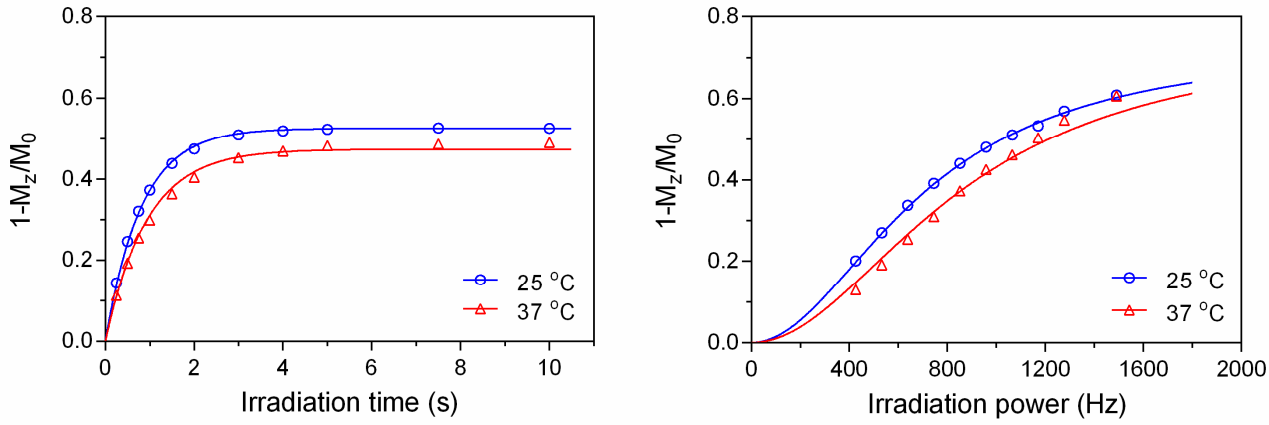

Figure S1. QUEST (left) and QUESP (right) results with **EuL** (15 mM) at 7 T and 25 or 37 °C. Values for the used saturation times, saturation power and performed fits are provided in the description above.

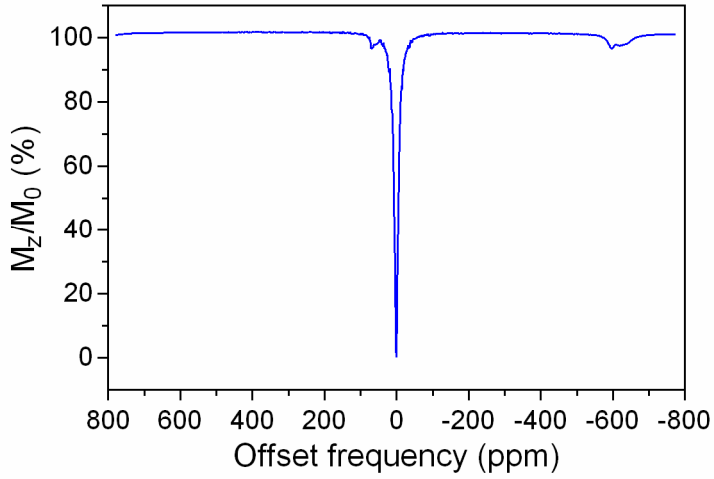

Figure S2. Z-spectrum of **TbL** (15 mM) obtained with following parameters B_1=25.0 µT, irradiation time = 3 s, 1 ppm resolution, 7 T. A weak CEST effect can be observed for the inner-sphere water molecule (-598 ppm) and amide protons (69 ppm).

3. ^{19}F NMR spectra

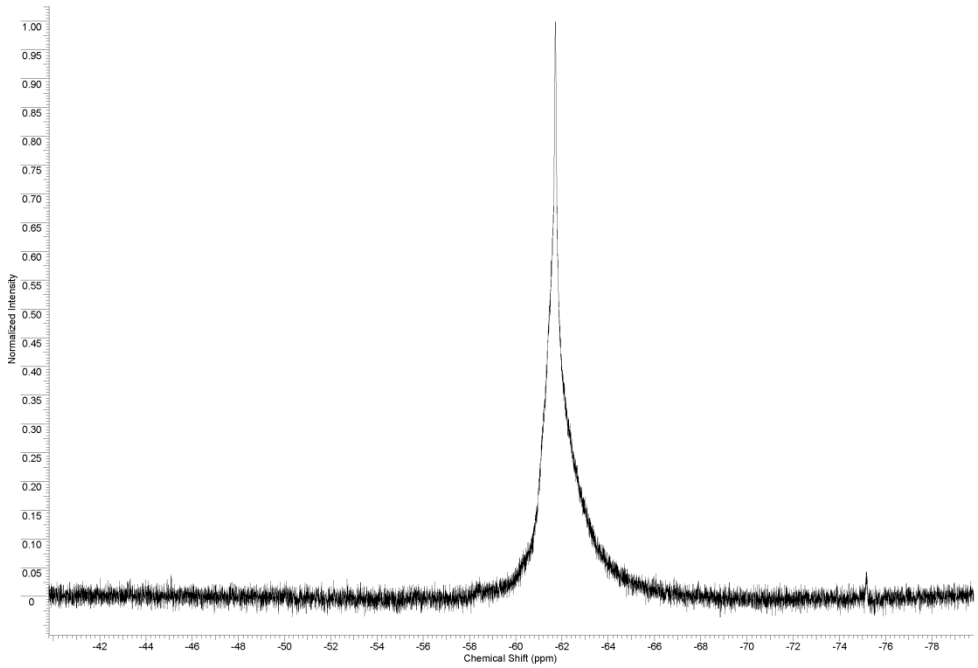

Figure S3. ^{19}F NMR spectrum of **GdL** in D_2O (282 MHz, 298 K).

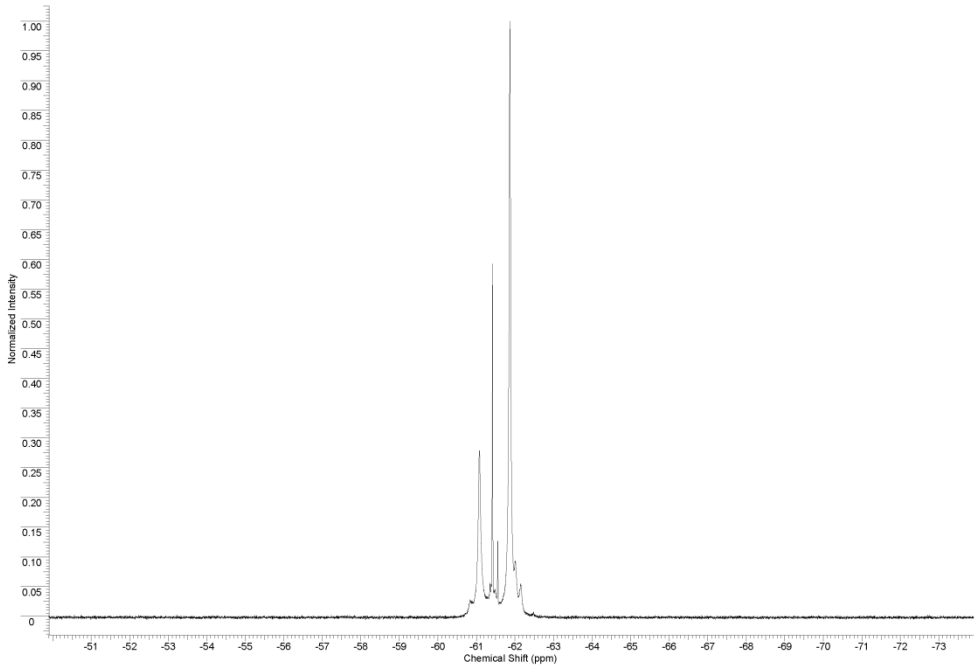

Figure S4. ^{19}F NMR spectrum of **EuL** in D_2O (282 MHz, 298 K).

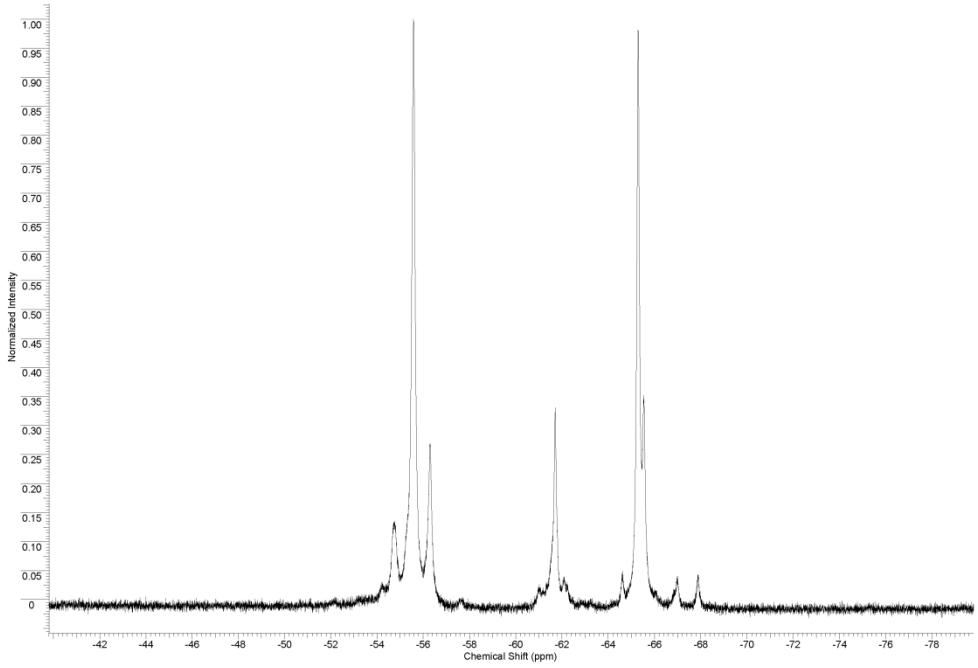

Figure S5. ^{19}F NMR spectrum of **TbL** in D_2O (282 MHz, 298 K).

4. NMR diffusion experiments

The determination of the diffusion coefficient *D* was performed using 2D – Diffusion Ordered NMR Spectroscopy (DOSY).[5] Experiments included 3 repetitions on **EuL** (15 mM, pH 7.3, 25 ^{o}C, δt= 2 ms, ΔT= 330 ms). Data analysis was done with TopSpin 2.1 using 16 linear points between 5–95 % gradient strength. The obtained value D=4.5±0.4 × 10^{-10} m^2s^{-1} is within the range of values previously reported by us on different monomacrocyclic systems.[6, 7]

5. MRI experiments

MRI experiments were performed on a Bruker 7T BioSpec 70/30 USR. A Bruker $^{1}H/^{19}F$ dual frequency volume coil was used for all (^{1}H and ^{19}F) *in vitro* experiments as well as for the ^{1}H *ex vivo*/*in vivo* measurements. The ^{19}F *ex vivo/in vivo* experiments were performed also using a Bruker surface coil and a custom-made micro coil.

MRI *in vitro*. Four vials were filled with: 1) **GdL**, 2) **EuL**, 3) **TbL** and 4) H_2O (all complexes 15 mM per Ln^{3+}), respectively and placed in a syringe containing saline solution. The ^1H scan protocol comprised a fast low angle shot (FLASH) imaging and a rapid acquisition with relaxation enhancement (RARE). The imaging parameters for the FLASH images were: echo time (TE) = 6.3 ms, repetition time (TR) = 100 ms, flip angle (FA) = 30°, resolution (RES) = 100x100 μm^2, slice thickness = 1.5 mm, total acquisition time (TA) = 5 min. The RARE images were acquired with a RARE factor = 8, TE = 40 ms, TR = 6000 ms, RES = 250×250 μm^2, TA = 1.5 min. The RARE sequence was also used to perform CEST imaging by adding a Gaussian presaturation pulse (B_1 = 18 μT, duration = 3 s) with an off-resonance frequency ranging from -30 kHz to +30 kHz. The pronounced shortening of T_1 and T_2 induced by **GdL** can clearly be seen in the T_1-weighted FLASH (Figure 3a) and T_2-weighted RARE images (Figure 3b). Only **EuL** exhibits a CEST effect, which can be observed by subtracting two RARE images which were presaturated at ±52 ppm with respect to the water resonance frequency.

The ^{19}F images were acquired using balanced steady state free precession (bSSFP) imaging. The scan parameters were: TE = 1.1 ms, TR = 2.2 ms, FA = 40°, number of excitations (NEX) = 15145, RES = 468x468 μm^2, slice thickness = 5 mm, TA=1 h. The three contrast agents are visible in the acquired images and exhibit a signal-to-noise ratio of about 8.

MRI *ex vivo* and *in vivo*. For these experiments, male Sprague-Dawley rats (150– 250 g, Charles River Laboratories) were used. The experiments were approved by the local authorities (Regierungspraesidium), and were in compliance with the guidelines of the European directive (2010/63/EU) for the care and protection of animals used for scientific purposes. Animals were housed individually prior to the experimental procedures with controlled light-dark cycle, temperature and humidity, with food and water provided ad libitum.

In each ^1H MRI experiment, the animal was initially anaesthetized with 5 % isoflurane (Forene, Abbott, Wiesbaden, Germany) and placed in a stereotactic frame (Stoelting Co., IL, US). Anaesthesia was then reduced to 1.5-2.0 % for maintenance. For ^{19}F MRI experiments, a mixture of medetomidine (0.4 mg/kg) and ketamine (60 mg/kg) (1:10) i.p. with robinul (0.05 mg/kg) s.c. as premedication was used. The depth of anesthesia was checked by the lack of withdrawal to a firmly pinched hind toe. The body temperature of the animal was maintained at 37.0 ± 1.0 °C by a rectal probe with a feedback controlled heat pad (50-7221-F,

Harvard Apparatus, MA, US). The eyes were protected with bepanthen eye ointment to keep the cornea from drying. Bregma and lambda were used for alignments and for locating the injection site. To target the somatosensory cortex, a position 3.4 mm right for **GdL** and left for **EuL** of midline, 0.2 mm anterior to bregma, and 1.5 mm below the pial surface was chosen as the site of injection. A burr hole was drilled at the skull directly above the injection site, and the contrast agent was delivered with a Hamilton syringe by a precision pump (70-4507, Harvard Apparatus) over the period of 20 min. The needle was retracted stepwise 10 min post-injection to avoid leakage of the contrast agent. In the case of *in vivo* experiments, the animal was sutured and transferred to the scanner where breathing rate, heart rate and blood oxygen saturation were also monitored during the scan. For *ex vivo* experiments, the animal was euthanized post-injection and transferred to the scanner for image acquisition.

MR images were acquired from 0.5-3.3 hours after intracranial injection of contrast agent using FLASH and RARE sequences with or without inversion recovery. Image analysis was performed in MATLAB (MathWorks, USA).

T_1-weighted ^{1}H and ^{19}F MRI experiments were performed with **GdL** (15 mM). T_1-weighted ^{1}H MRI was performed using the FLASH sequence with the following parameters: field-of-view (FOV) = 37.66×49.12 mm^2, matrix size (MTX) = 96×96, 1 slice, 1.29 mm thickness, TR = 25 ms, TE = 1.5 ms, FA = 20°, NEX = 48, TA = 1 min 55 s. ^{19}F MRI was performed using non-fluorine containing anesthesia (see above). In all experiments a reference tube containing a solution of NaF (192 mM) and Dotarem® (20 mM) was placed between the animal's head and the RF coil in order to have comparable T_1 and T_2 relaxation times as the contrast agent. Imaging was performed using the following sequences: FLASH, balanced steady state free precession (bSSFP), 2D, 3D ultrashort TE (UTE), zero TE (ZTE) and chemical shift imaging (CSI) with the scans lasting up to 3.3 hrs.

T_1-weighted and CEST MRI experiments were performed with **EuL** (15 mM). Following intracranial injection under constant anesthesia, the animal was euthanized and positioned in the scanner. Firstly, the anatomical scan was performed (IR-RARE): FOV = 60×60 mm^2, MTX=256×192, 5 slices, 0.5 mm thickness. TR/TE = 10000/9.7 ms, Rare factor = 8, inversion time = 8000 ms, NEX = 1, TA = 4 min. Thereafter, pairs of CEST images at frequencies with and without water saturation were acquired (RARE) with the following parameters: FOV = 60×60 mm^2, MTX = 120×120, 1 slice, 0.5 mm thickness, TR/TE = 5095.3/10 ms, Rare factor = 8, saturation pulse t_{sat} = 5 s, B_1=11.9 μT. The saturation offsets

were initially screened with 5 ppm, thereafter with 1 and 0.5 ppm resolution, respectively. The experiments at optimized saturation offset were performed with NEX = 12, TA = 15 min 17 s. CEST image analysis comprised firstly defining a region of interest (ROI), centered at the injection point with addition of surrounding pixels using the T_1-weighted image. Thereafter, the CEST contrast image was quantified using the asymmetric magnetization transfer ratio, $MTR_{asym} = (S_b-S_{CEST})/S_b \times 100$, where S represents the signal intensity of a given ROI at resonance of CEST (S_{CEST}) or background (S_b) signals, respectively.

5. References

1. Z. Kovacs and A. D. Sherry, *Synthesis*, 1997, 759-763.
2. D. M. Corsi, C. Platas-Iglesias, H. van Bekkum and J. A. Peters, *Magn. Reson. Chem.*, 2001, **39**, 723-726.
3. A. Barge, G. Cravotto, E. Gianolio and F. Fedeli, *Contrast Media Mol. Imaging*, 2006, **1**, 184-188.
4. M. T. McMahon, A. A. Gilad, J. Y. Zhou, P. Z. Sun, J. W. M. Bulte and P. C. M. van Zijl, *Magn. Reson. Med.*, 2006, **55**, 836-847.
5. A. Macchioni, G. Ciancaleoni, C. Zuccaccia and D. Zuccaccia, *Chem. Soc. Rev.*, 2008, **37**, 479-489.
6. J. Henig, I. Mamedov, P. Fouskova, E. Tóth, N. K. Logothetis, G. Angelovski and H. A. Mayer, *Inorg. Chem.*, 2011, **50**, 6472-6481.
7. S. Gündüz, T. Savić, R. Pohmann, N. K. Logothetis, K. Scheffler and G. Angelovski, *ACS Sensors*, 2016, **1**, 483-487.

Paramagnetic Macrocyclic Platform for Efficient pH-Mapping via CEST MRI

Tanja Savić,[a] Laura Valencia,[b] Paulo Pérez-Lourido,[b] David Esteban-Gómez,[c] Moritz Zaiss,[d] Carlos Platas-Iglesias*,[c] Goran Angelovski,*,[a]

We report on a macrocyclic platform that forms kinetically highly inert paramagnetic complexes and possesses an excellent outlook for the development of bioresponsive paraCEST (paramagnetic chemical exchange saturation transfer) contrast agents. The investigated europium(III) chelate is non-hydrated and contains four amide groups, each possessing two highly shifted proton resonances distant from the bulk water. The amide protons are in slow-to-intermediate exchange with bulk water, which gives rise to the generation of a strong CEST effect at low probe concentration and saturation powers. We demonstrate the potential of this platform for mapping pH in its microenvironment and foresee perspectives for the development of diverse paraCEST sensors.

Efficient detection and monitoring of pathological processes is a key step in ensuring the timely diagnosis of numerous diseases. Various molecular imaging techniques aim for developing reliable protocols to visualize such biological events, with magnetic resonance imaging (MRI) being at the forefront of this progress. In addition to the ability to cover larger volumes or enable investigations of tissues at any depth, MRI possesses outstanding potential and versatility to study functional processes with an unprecedented specificity. To this end, different nuclei, MRI protocols or bioresponsive probes have been employed in attempts to assess the functional state of tissues, especially the environmental pH as one of the best physiological markers.

Chemical exchange saturation transfer (CEST) is an emerging MRI methodology appreciated due to a few advantageous features that circumvent the current shortcomings of other existing methods.[1] CEST takes advantage of the magnetization transfer between the exchanging species operating at two different frequencies (most frequently a pool of protons from the CEST probe and bulk water), thus reducing the magnetization of the latter once the former species is irradiated with a radiofrequency (RF) pulse of defined energy. The great advantage of this strategy is the ability of providing signal response at will: the CEST effect or image will be generated only with the application of desired saturation pulses. Moreover, the existence of at least two separate exchange processes (e.g. two separate pools of protons in exchange with protons from bulk water) paves the way for highly specific, multifrequency and consequently multicolor CEST measurements. Finally, since the exchange rates are intrinsically tied to the resulting intensity of CEST, any alteration on the exchange rates will ultimately modulate the recorded CEST effect. For instance, pH changes in the microenvironment of the CEST pair(s) affect the saturation transfer process and thus the CEST MR image.

Several useful approaches have been reported in attempts to develop CEST probes and methods enabling pH mapping in tissue.[2-9] Irrespective if they are comprised of diamagnetic molecules or those with paramagnetically shifted protons (diaCEST or paraCEST probes, respectively), their common feature is the presence of the CEST-active pool sufficiently distant from bulk water frequency. This ensures effective magnetization transfer (MTR) and adjustment of the exchange rates in the slow exchange regime, thus allowing low energy saturation pulses to produce detectable CEST effects. The majority of the recent findings clearly favor ratiometric approaches, i.e. exploitation of two separate pools of protons that exchange with bulk water where pH changes influence their rates to different extents.

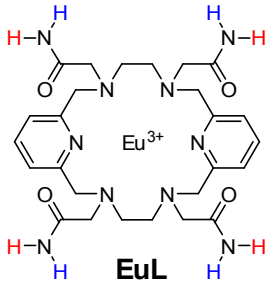

Figure 1. Chemical structure of the complex studied in this work. NMR-equivalent protons on amides were deliberately marked with same color.

Taking these demands into consideration, we developed a paramagnetic platform that encompasses the majority of the parameters necessary for the execution of convenient and efficient pH-mapping of the microenvironment by means of ratiometric CEST measurements. We built upon the previous work on the 18-membered macrocyclic molecule that provides

[a] T. Savić, Priv.-Doz. Dr. G. Angelovski
MR Neuroimaging Agents, MPI for Biological Cybernetics, Tuebingen (Germany)
Email: goran.angelovski@tuebingen.mpg.de
[b] Prof. Dr. D. Esteban-Gómez, Prof. Dr. C. Platas-Iglesias
Centro de Investigacións Científicas Avanzadas (CICA) and Departamento de Química, Facultade de Ciencias, Universidade da Coruña, 15071 A Coruña (Spain)
E-mail: carlos.platas.iglesias@udc.es
[c] Prof. P. Pérez-Lourido, Prof. L. Valencia
Departamento de Química Inorgánica, Facultad de Ciencias, Universidade de Vigo, As Lagoas, Marcosende, 36310 Pontevedra, (Spain)
[d] Dr. M. Zaiss
High-Field Magnetic Resonance, MPI for Biological Cybernetics, Tuebingen (Germany).

Supporting information for this article is on the WWW under doi:xxx.

exceptionally inert Pr^{3+}, Eu^{3+} or Yb^{3+} complexes and exhibits the paraCEST effect.[10] We improved the previous system by incorporating amide instead of hydroxyl groups (Figure 1), thus obtaining 8 instead of 4 exchanging protons. Furthermore, being geometrically oriented in a different manner, we anticipated their grouping into two pairs of protons. This opened the possibility of getting two CEST effects at two different frequencies.

The ligand **L** was obtained in good yield by alkylation of the 3,6,10,13-tetraaza-1,8(2,6)-dipyridinecyclotetradecaphane precursor with bromoacetamide in acetonitrile using Na_2CO_3 as a base.[11] The paramagnetic Eu^{3+} complex was obtained in good yield (60%) by direct reaction of the ligand with the appropriate hydrated lanthanide nitrate in methanol. The mass spectrum (ESI^+) shows intense peaks due to the $[Eu(L\text{-}H)(NO_3)]^+$ and $[Eu(L\text{-}2H)]^+$ entities that confirm the formation of the complexes. Crystals of formula **[EuL]**$(NO_3)_3 \cdot 3H_2O$ were obtained by slow evaporation of aqueous solutions of the complex. They contain the $[\mathbf{EuL}]^{3+}$ cations, highly disordered nitrate anions and water molecules. While the quality of the crystallographic data of the Eu^{3+} complex is not very high, the overall structure of the $[\mathbf{EuL}]^{3+}$ complex and the bond distances and angles of the metal coordination environment are reasonably accurate (Figure 2). Furthermore, we obtained single crystals of the Y^{3+} analogue (Figure S1, Supporting Information), which presents a very similar structure.

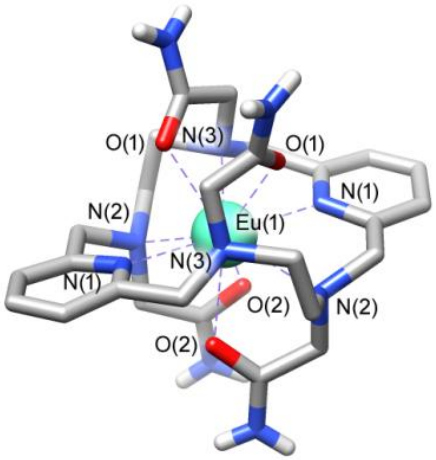

Figure 2. View of the structure of the $[\mathbf{EuL}]^{3+}$ cation present in crystals of $[EuL](NO_3)_3 \cdot 3H_2O$. Hydrogen atoms (except those of amide groups) are omitted for simplicity. Bond distances [Å]: Eu-N(1), 2.593(15); Eu-N(2), 2.63(2); Eu-N(3), 2.644(19); Eu-O(1), 2.525(16); Eu-O(2), 2.511(15).

The $[\mathbf{EuL}]^{3+}$ cations present ten-coordinate metal ions that are directly bonded to the six donor atoms of the macrocyclic skeleton and the four oxygen atoms of the acetamide pendants (Figure 2). The ligand **L** adopts a twist-wrap conformation in which the angles involving the two pyridyl nitrogen atoms and the metal ion are nearly linear (<179º). The two pyridyl units are twisted with respect to each other, so that the least-squares planes intersect at angles of ca. 19-20º.

The ^1H NMR spectrum of **EuL** recorded in a H_2O solution presents 10 paramagnetically shifted signals in the range ~20 to -20 ppm, which is in line with the D_2 symmetry observed in the solid state. The spectrum recorded in 1 M HCl remains unchanged over a period of at least 25 days (Figure S2, Supporting Information), with no signals due to the free ligand being observed. This experiment evidences that the complex presents an astonishing inertness under very harsh conditions. For instance, the commercially available contrast agent $[Gd(DOTA)]^-$ dissociates with a half-live of ~30 hours under these conditions.[12]

The UV absorption and luminescence emission experiments on **EuL** complex gave further insights on its coordination and photophysical properties in solution (Figures S3 in Supporting Information). The absorption spectrum presents a maximum at 268 nm (ε = 11000 M^{-1} cm^{-1}) characteristic of the pyridyl group,[13] and this band can be used for the sensitized Eu^{3+} luminescence emission. The luminescence emission spectrum consists of the $^5D_0 \rightarrow {}^7F_J$ bands typical for Eu^{3+}. The emission pattern is characteristic of a rather symmetric crystal field around the metal coordination environment, which is attributed to the D_2 symmetry observed both in the solid state and in solution. The emission spectrum exhibits unusually intense ΔJ = 5 and ΔJ = 6 transitions, a feature that is characteristic of this type of coordination.[14] Further investigations indicated the monoexponential decay with a lifetime of 0.914 ms and a modest luminescence quantum yield of ϕ_{Eu} = 0.11, which can be attributed to the presence of amide NH oscillators that provide a rather efficient vibrational deactivation of the Eu^{3+} $^5D_0$ excited state.[15]

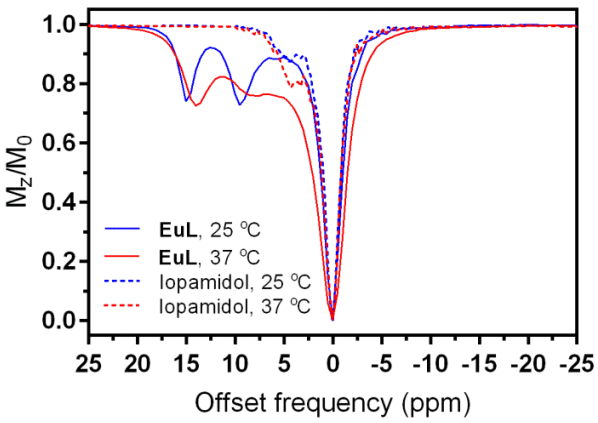

Figure 3. Z-spectra of **EuL** (lines) and iopamidol (dashes) at 25 °C (blue) and 37 °C (red) at 5 mM concentration, B_1=5 μT and saturation time 5 s (PBS, pH 7.4).

The favorable kinetic inertness and the coordination properties of this non-hydrated paramagnetic complex indicated its prospected outlook for potential CEST applications; hence the CEST features were investigated in more detail at 7 T magnetic field (300 MHz). The Z-spectra of **EuL** were recorded at 25 and 37 °C (Figure 3). Already at the chelate concentration of 5 mM and low saturation pulse power (5 μT), the advantageous CEST properties of this complex became obvious. Namely, two paramagnetically shifted and well resolved resonances at 15 and 9.5 ppm from bulk water exhibited CEST effect of ~25% at 25 °C, which corresponds to the proton transfer enhancement (PTE) of 5550.[16] Upon heating to 37 °C, the intensity of CEST

effect remained similar, while the shift of resonances decreased by ~1 ppm along with a broadening of the peak closer to bulk water, suggesting an increase in the exchange rates due to higher temperature. For comparison, we recorded the Z-spectra of iopamidol (Isovue™ or Solutrast™) under the same conditions (5 mM, pH 7.4, 25 and 37 °C). In addition to the existence of diamagnetic CEST peaks closer to the resonance of bulk water, their intensity was weaker than in **EuL**, reaching a maximum CEST effect of 20% (Figure 3).

We have applied quantitative CEST (qCEST) analysis to determine exchange rate values (k_{ex}),[17] using the Bloch-McConnell (BM) equations and assuming a 3-pool model (bulk water and two paramagnetically-shifted exchanging pools). The qCEST procedure employing data of 7 different saturation powers resulted in k_{ex} values of 1029±63 Hz and 1914±78 Hz for 25 °C and 2652±132 Hz and 4699±229 Hz at 37 °C, with the strongly shifted peak (14-15 ppm) having an exchange rate which was roughly twice as slow as that of the peak with smaller paramagnetic shift. These k_{ex} values are just slightly higher than those reported for iopamidol also at the physiological pH;[18-19] hence, we proceeded with the characterization of the **EuL** complex as a prospective pH-sensitive paraCEST agent. Namely, the exchange rates are expected to change significantly with variations in pH, which would give rise to different CEST effects. We therefore recorded a series of Z-spectra at variable pH values from 6.0 to 8.0, using pulses with different saturation powers ranging from 1 to 15 μT (Figure S4 in Supporting Information); subsequently, we performed the qCEST as well as the inverse difference of opposite frequencies (asymmetry analysis) to obtain the k_{ex} values and the inverse MTR difference (MTR_{ind}), respectively.[20]

Table 1. Exchange rates (in Hz) determined with qCEST method for **EuL** (5 mM) at variable pH (PBS, 37 °C).[17]

pH	Peak at 8 ppm	Peak at 14 ppm
6.0	138±19	66±23
6.4	321±30	162±31
6.8	941±75	487±69
7.2	2631±130	1364±101
7.6	5631±225	2977±150
8.0	15481±1792	7368±1002

The multi-B_1 experiments at variable pH values revealed advantageous exchange properties of **EuL** for pH sensing. The exchange rates remained roughly in 2:1 ratio throughout the studies for the peak with smaller shift (Table 1). CEST effects of at least 5 % were recorded already using B_1=2.5 μT at all pH values above 6.4; we note that this lies within the saturation power limits permitted for use at clinical settings. Moreover, the increase of exchange rates along with the increase in pH additionally affected the CEST effects. When MTR_{ind} were plotted as a function of pH, the CEST signals exhibited pH dependency until pH~7.4 (Figure S5, Supporting Information). Above this pH the MTR_{ind} dropped, due to a decreased labeling efficiency at the given B_1 level and the faster exchange.

The concentration independent ratio of different MTR_{ind} was calculated either by comparing the effects at different frequencies and same saturation power, or using the so-called ratio of RF power mismatch method.[4] When the obtained ratios were plotted as a function of pH, the pH-dependent effect became even more obvious (Figure 4 and Figure S6, Supporting Information). The ratio of MTR_{ind} at B_1 = 7.5 μT and 2.5 μT at either frequencies exhibited significant changes in the region from slightly acidic to physiological pH (6.4-7.4, Figure 4a), as previously observed in the analysis and behavior of iobitrol.[4] Similar results were obtained when the ratio of MTR_{ind} at B_1 = 7.5 μT and 14 ppm versus the signal ratio at B_1 = 2.5 μT and 8.5 ppm was calculated, or when just the ratios of signals of two peaks at B_1 = 5 μT was used (Figure 4b), as previously demonstrated for the behavior of iopamidol.[21] We stress these are very advantageous properties, highly desirable in the application of responsive probes: all results reported here were achieved with **EuL** at low saturation powers and probe concentrations. Next, the ratiometric analysis yields results that are independent of probe concentration.[22] Finally, the existence of CEST effects at two frequencies that – for a fixed power – changes proportionally with pH due to a virtually constant ratio of k_{ex} values (Table 1 and Figure S7) allows for a simplified analysis in which the results obtained with one experiment can be cross-checked with those at the other frequency, i.e. one CEST signal can serve as an internal reference to another one.

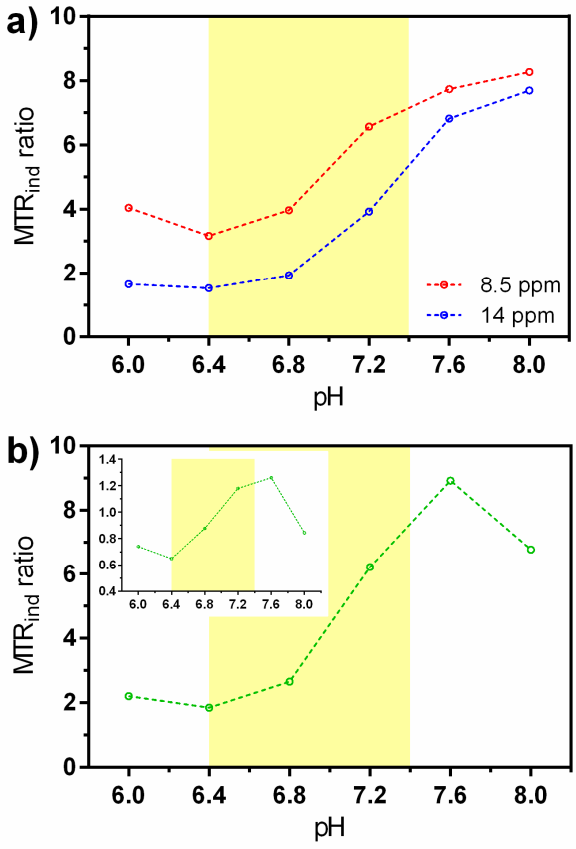

Figure 4. Ratio of MTR_{ind} for **EuL** (5 mM in PBS, 37 °C) at varying pH values. a) Ratio of signals at 7.5 μT and 2.5 μT at 8.5 ppm (red) and 14 ppm (blue). b) Ratio of signal obtained with 7.5 μT at 14 ppm with the signal obtained with 2.5 μT at 8.5 ppm; inset: the ratio of signals at 14 and 8.5 ppm and B_1 = 5 μT. The pH region 6.4-7.4 is highlighted with yellow color.

An additional set of experiments were performed on tube phantoms in the MRI scanner. Six tubes with identical concentrations of **EuL** (3 mM) were prepared in PBS at different pH (6.0, 6.4, 6.8, 7.2, 7.6 and 8.0). The images were recorded at room temperature and varying saturation powers (3.0, 4.0, 5.0, 6.0 and 7.5 μT). The lower temperature and hence the exchange rates reflected on the lower intensity of CEST effect. Nevertheless, the obtained signals were analyzed in the same fashion as the former NMR experiments at 37 °C (Figure S8, Supporting Information). Consequently, the MTR_{ind} ratio of different frequencies and saturation powers could be used to obtain a set of pH maps, even for given experimental parameters (Figure 5 and Figure S9, Supporting Information).[4] Due to low k_{ex} and therefore low MTR_{ind} intensity at only 3 mM **EuL**, the MRI contrast at pH 6.0 was insufficient to extract the correct pH value (Figure 5); such signals can in principle even be filtered by a pixelwise threshold for the MTR. However, the pH region typically detected in solid tumors (6.5-7.0)[23] or ischemia[24] was well covered and reliably determined by the MRI phantom experiment with **EuL**.

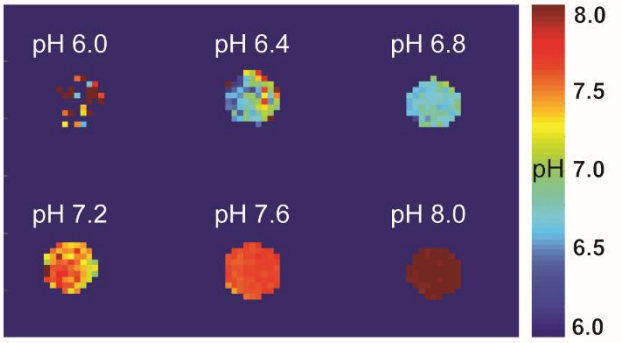

Figure 5. CEST MRI on tube phantoms with **EuL** (3 mM in PBS, RT). pH maps were generated from the ratio of experiments done at B_1=7.5 and 4 μT, saturation time 5 s and with the peak at 9.7 ppm.

In summary, we have reported on the paramagnetic platform that forms kinetically highly inert complexes and has an excellent outlook for the development of pH sensitive paraCEST probes. The investigated Eu^{3+} chelate displays very affirmative CEST features due to two highly shifted protons that are in slow to intermediate exchange with bulk water. The variations in pH reflect on the intensity of the obtained CEST effect, which exhibits pH-dependent behavior either at a single resonance or from the ratio of applied saturation powers and different resonance peaks. Moreover, the high intensity of the CEST effect allows for applications of small quantities of this paraCEST probe, as well as low saturation powers that match clinically approved protocols. Finally, the chemical nature of this platform envisions an immense number of potential chemical transformations and the development of a great variety of structures that can further improve on the already excellent features. Ultimately, this macrocyclic platform could pave the way to many exciting advances in the field of responsive paraCEST agents with high potential for clinical applications.

Acknowledgements

The authors thank Dr. Rolf Pohmann and Dr. Dario Longo for helpful discussions. T.S. thanks the German Academic Exchange Service (DAAD) for the Ph.D. fellowship. D. E.-G. and C. P.-I. thank Ministerio de Economía y Competitividad (CTQ2016-76756-P) and Xunta de Galicia (ED431B 2017/59 and ED431D 2017/01) for generous financial support. M. Z. thanks the research support of the German Research Foundation (DFG, grant ZA 814/2-1) and European Union's Horizon 2020 research and innovation programme (Grant Agreement No. 667510).

Keywords: CEST• MRI • Macrocycles • pH mapping • lanthanides

References

[1] M. T. McMahon, A. A. Gilad, J. W. M. Bulte, P. C. M. van Zijl, *Chemical Exchange Saturation Transfer Imaging : Advances and Applications*, Pan Stanford Publishing Pte. Ltd., Singapore, **2017**.

[2] D. V. Hingorani, A. S. Bernstein, M. D. Pagel, *Contrast Media Mol. Imaging* **2015**, *10*, 245-265.

[3] L. Q. Chen, C. M. Howison, J. J. Jeffery, I. F. Robey, P. H. Kuo, M. D. Pagel, *Magn. Reson. Med.* **2014**, *72*, 1408-1417.

[4] D. L. Longo, P. Z. Sun, L. Consolino, F. C. Michelotti, F. Uggeri, S. Aime, *J. Am. Chem. Soc.* **2014**, *136*, 14333-14336.

[5] Y. K. Wu, T. C. Soesbe, G. E. Kiefer, P. Y. Zhao, A. D. Sherry, *J. Am. Chem. Soc.* **2010**, *132*, 14002-14003.

[6] D. Delli Castelli, E. Terreno, S. Aime, *Angew. Chem. Int. Ed.* **2011**, *50*, 1798-1800.

[7] S. J. Dorazio, A. O. Olatunde, J. A. Spernyak, J. R. Morrow, *Chem. Commun.* **2013**, *49*, 10025-10027.

[8] A. E. Thorarinsdottir, K. Du, J. H. P. Collins, T. D. Harris, *J. Am. Chem. Soc.* **2017**, *139*, 15836-15847.

[9] A. Bar-Shir, J. W. M. Bulte, A. A. Gilad, *ACS Chemical Biology* **2015**, *10*, 1160-1170.

[10] G. Castro, M. Regueiro-Figueroa, D. Esteban-Gomez, R. Bastida, A. Macias, P. Perez-Lourido, C. Platas-Iglesias, L. Valencia, *Chem. Eur. J.* **2015**, *21*, 18662-18670.

[11] G. L. Rothermel, L. Miao, A. L. Hill, S. C. Jackels, *Inorg. Chem.* **1992**, *31*, 4854-4859.

[12] E. Toth, E. Brucher, I. Lazar, I. Toth, *Inorg. Chem.* **1994**, *33*, 4070-4076.

[13] G. Castro, R. Bastida, A. Macias, P. Perez-Lourido, C. Platas-Iglesias, L. Valencia, *Inorg. Chem.* **2015**, *54*, 1671-1683.

[14] A. Nonat, D. Esteban-Gomez, L. Valencia, P. Perez-Lourido, J. L. Barriada, L. Charbonniere, C. Platas-Iglesias, *Dalton Trans.*, *Submitted*.

[15] A. Beeby, I. M. Clarkson, R. S. Dickins, S. Faulkner, D. Parker, L. Royle, A. S. de Sousa, J. A. G. Williams, M. Woods, *J. Chem. Soc., Perkin Trans. 2* **1999**, 493-503.

[16] J. Y. Zhou, P. C. M. van Zijl, *Prog. Nucl. Magn. Reson. Spectrosc.* **2006**, *48*, 109-136.

[17] M. Zaiss, G. Angelovski, E. Demetriou, M. T. McMahon, X. Golay, K. Scheffler, *Magn. Reson. Med.* **2018**, *79*, 1708-1721.

[18] S. Aime, L. Calabi, L. Biondi, M. De Miranda, S. Ghelli, L. Paleari, C. Rebaudengo, E. Terreno, *Magn. Reson. Med.* **2005**, *53*, 830-834.

[19] P. Z. Sun, D. L. Longo, W. Hu, G. Xiao, R. H. Wu, *Phys. Med. Biol.* **2014**, *59*, 4493-4504.

[20] M. Zaiss, J. Z. Xu, S. Goerke, I. S. Khan, R. J. Singer, J. C. Gore, D. F. Gochberg, P. Bachert, *NMR Biomed.* **2014**, *27*, 240-252.

[21] D. L. Longo, W. Dastru, G. Digilio, J. Keupp, S. Langereis, S. Lanzardo, S. Prestigio, O. Steinbach, E. Terreno, F. Uggeri, S. Aime, *Magn. Reson. Med.* **2011**, *65*, 202-211.
[22] L. A. Ekanger, M. J. Allen, *Metallomics* **2015**, *7*, 405-421.
[23] G. Helmlinger, F. Yuan, M. Dellian, R. K. Jain, *Nat. Med.* **1997**, *3*, 177-182.
[24] P. Z. Sun, E. F. Wang, J. S. Cheung, *Neuroimage* **2012**, *60*, 1-6.

COMMUNICATION

A paramagnetic and highly kinetically inert complex produces strong chemical exchange saturation transfer (CEST) effect. These advantageous features were utilized to produce pH maps in the corresponding CEST MRI experiment, using the studied paramagnetic complex as an MRI contrast agent.

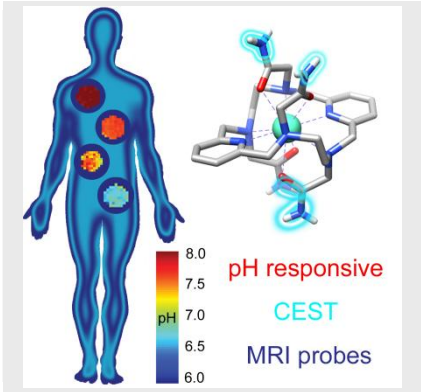

T. Savić, L. Valencia, P. Pérez-Lourido, D. Esteban-Gómez, M. Zaiss, C. Platas-Iglesias G. Angelovski**

Page No. – Page No.

Paramagnetic Macrocyclic Platform for Efficient pH-Mapping via CEST MRI

Supporting Information

Paramagnetic Macrocyclic Platform for Efficient pH-Mapping via CEST MRI

Tanja Savić,[a] Laura Valencia,[b] Paulo Pérez-Lourido,[b] David Esteban-Gómez,[c] Moritz Zaiss,[d] Carlos Platas-Iglesias*,[c] and Goran Angelovski,*,[a]

[a] MR Neuroimaging Agents, MPI for Biological Cybernetics, Max-Planck-Ring 11, 72076 Tübingen, Germany, E-mail: goran.angelovski@tuebingen.mpg.de

[b] Departamento de Química Inorgánica, Facultad de Ciencias, Universidade de Vigo, As Lagoas, Marcosende, 36310 Pontevedra, Spain

[c] Centro de Investigacións Científicas Avanzadas (CICA) and Departamento de Química, Facultade de Ciencias, Universidade da Coruña, 15071 A Coruña, Spain

[d] High-Field Magnetic Resonance, MPI for Biological Cybernetics, Tuebingen, Germany

Table of Contents

Measurements

^{1}H NMR spectra of the ligand and complexes were recorded on a Bruker ARX400 spectrometer, while the CEST experiments were performed on a Bruker Avance III NMR spectrometer (Bruker, Ettlingen, Germany). Chemical shifts were referenced by using the residual solvent proton signals.[1] Elemental analysis was performed in a Carlo-Erba EA 1108 microanalyzer. Infrared(IR) spectra were recorded as KBr discs on a Bruker VECTOR 22 spectrometer. ESI experiments were performed on an microTOF(focus) mass spectrometer (Bruker Daltonics, Bremen, Germany). Ions were generated using an ApolloII (ESI) source and ionization was achieved by electrospray.

UV-Vis absorption spectra were recorded on a Jasco V-650 spectrometer using 1 cm quartz cells. The excitation and emission spectra in the UV-Vis region were obtained with a Horiba FluoroMax Plus-P spectrofluorometer equipped with a 150 W ozone-free xenon arc lamp and a R928P photon counting emission detector. A photodiode reference detector for monitoring lamp output. All spectra were corrected for the instrumental response provided by the manufacturer. An integration time of 0.1 s was used in all steady state measurements. Luminescence decays were measured on the same instrument working in the phosphorescence mode using a xenon flash lamp. Emission lifetimes were obtained by least-squares fits of the decay data using monoexponential decay functions. The emission quantum yield of **EuL** was obtained with optically diluted solutions using the trisdipicolinate complex $Cs_3[Eu(pic)_3]$ (Φ=13.5% in TRIS buffer, pH 7.4) as reference.[2-3]

Synthesis

2,2',2'',2'''-(3,6,10,13-Tetraaza-1,8(2,6)-dipyridinacyclotetradecaphane-3,6,10,13-tetrayl)tetraacetamide (L). The macrocyclic precursor 3,6,10,13-tetraaza-1,8(2,6)-dipyridinecyclotetradecaphane[4] (1.50 g, 4.60 mmol) and Na_2CO_3 (2.968 g, 28 mmol) were refluxed in acetonitrile (50 mL). A solution of 2-bromoacetamide (3.379 g, 24 mmol) in acetonitrile (30 mL) was added dropwise to the reaction mixture, which was refluxed for 24 hours. The mixture was allowed to cool and the solid obtained was isolatred by filtration, washed with water and recrystallized from methanol to give a white crystalline solid, which was collected by filtration and dried providing 1.240 g of $L{\cdot}H_2O$ (Yield 51%). $C_{26}H_{40}N_{10}O_5$ (572.32): calcd. C 54.5, H 7.0, N 24.5; found C 54.2, H 7.3, N 24.7. IR (ATR, cm^{-1}): 1594 (s), 1456 (s) [ν(C=C) and $\nu(C=N)_{py}$], 1676 (s) [ν(C=O)], 3165 (m) [ν(NH)]. MS (ESI-MS,

m/z, found (calculated)): 555.3 (555.3) $[L+H]^+$. ^1H NMR (CD_3OD, δ, ppm): H1 7.70 (t, 2H), H2 7.25 (d, 4H, ^3J = 7.7 Hz), H4 3.37 (b, 8H), H5 2.75 (b, 8H), H6 3.14 (b, 8H).

General procedure for the preparation of the complexes. A solution of $Ln(NO_3)_3 \cdot xH_2O$ (0.04 mmol) in methanol (5 mL) was added to a stirred solution of **L**$\cdot H_2O$ (0.023 g, 0.04 mmol) in the same solvent (10 mL) and the mixture was slightly heated. Slow concentration of the methanolic solutions gave crystalline products that were isolated by filtration and dried.

[EuL](NO$_3$)$_3$·3H$_2$O. The complex was prepared using **L**$\cdot H_2O$ (0.023 g, 0.04 mmol) and $Eu(NO_3)_3 \cdot 5H_2O$ (0.017 g, 0.04 mmol). Yield: 0.022 g, 60%. Anal. Calcd for $C_{26}H_{44}N_{13}O_{16}Eu$: C, 33.0; H, 4.7; N, 19.2%. Found: C, 33.1; H, 4.9; N, 19.1%. ESI-MS (*m/z*, found (calculated)): 768.2 (768.2) $[Eu(L-H)(NO_3)]^+$; 705.2 (705.2) $[Eu(L-2H)]^+$. IR (ATR): 1592 (s), 1454 (s) [ν(C=C) and $\nu(C=N)_{py}$], 1651 (s) [ν(C=O)], 3262 (m), 3162 (m) $\nu(NH_2)$, 1314 (s), 829 (m) [$\nu(NO_3^-)$] cm^{-1}. Crystals suitable for X-ray diffraction were obtained by slow evaporation of an aqueous solution of the complex.

[YL](NO$_3$)$_3$·3H$_2$O. The complex was prepared using **L**$\cdot H_2O$ (0,023 g, 0.04 mmol) and $Y(NO_3)_3.6H_2O$ (0.015 g, 0.04 mmol). Yield: 0.028 g, 79%. Anal. Calcd for $C_{26}H_{44}N_{13}O_{16}Y$: C, 35.3; H, 5.0; N, 20.6%. Found: C, 35.7; H, 5.5; N, 20.3%. ESI-MS (*m/z*, found (calculated)): 704.2 (704.2) $[Y(L-H)(NO_3)]^+$; 641.2 (641.2) $[Y(L-2H)]^+$. IR (ATR): 1604 (s), 1459 (s) [ν(C=C) and $\nu(C=N)_{py}$], 1661 (s) [ν(C=O)], 3169 (m) $\nu(NH_2)$, 1321 (s), 888 (m), 747 (m) [$\nu(NO_3^-)$] cm^{-1}. Crystals with formula **[YL](NO$_3$)$_3$·3H$_2$O** suitable for X-ray diffraction were obtained by slow evaporation of an aqueous solution of the complex.

Crystal structure determinations

Crystallographic data of [**EuL**]$(NO_3)_3 \cdot 3H_2O$ were collected at 293(2) K on a BRUKER Smart-CCD-1000 diffractometer using Graphite monochromated Mo-Kα radiation. All data were corrected by Lorentz and polarization effects. For [**YL**]$(NO_3)_3 \cdot 3H_2O$, crystallographic data were measured at room temperature using a Bruker Smart 6000 CCD detector and Cu-K α radiation (λ= 1.54178 Å) generated by an Incoatec microfocus source equipped with Incoatec Quazar MX optics. The software APEX2 was used for collecting frames of data, indexing reflections, and the determination of lattice parameters, while SAINT was used for integration of the intensity of reflections.[5] The software SADABS was used in all cases for

scaling and empirical absorption correction.[6] All structures were solved by using the SHELXT program and refined by a full- matrix least-squares based on F^2.[7] The Squeeze program was used to correct the reflection data for the diffuse scattering due to the disordered nitrate ions and water molecules present in the unit cell of [**EuL**]$(NO_3)_3 \cdot 3H_2O$.[8] Non-hydrogen atoms were refined with anisotropic displacement parameters. Hydrogen atoms were included in idealized positions and refined with isotropic displacement parameters. CCDC 1886847 and 1886848 contain the supplementary crystallographic data for this paper. Molecular graphics were generated using ORTEP-3.[9]

CEST experiments

The saturation transfer experiments were carried out at 25 or 37 ^oC by irradiating the **EuL** sample at increments of 0.5 ppm in the frequency range ±20 ppm, then at increments of 1 ppm in the frequency range ±20-50 ppm followed by an FID readout; for iopamidol, we irradiated the sample at increments of 0.25 ppm in the frequency range ±10 ppm, then at increments of 5 ppm in the frequency range ±10-50 ppm. Spectra were measured by recording the bulk water signal intensity as a function of the presaturation frequency. Saturation offsets are reported relative to the resonance frequency of bulk water.

For each temperature, data was collected by varying the saturation power whilst the saturation time remained constant (5 s for experiments reported in the Figure 3, or 15 s for the experiments reported in Figures 4, S4-7 and Table 1). The saturation field strengths used were: 2.5, 3, 5, 6, 7.5, 10 and 15 μT for experiments reported in the Figure 3, or 1, 2.5, 5, 7.5, 10, 12.5 and 15 μT for the experiments reported in Figures 4, S4-7 and Table 1. Longitudinal relaxation times were obtained in an independent experiment using the standard inversion recovery with 1% gradient to eliminate the radiation damping effect. The CEST experiments at variable pH (experiments reported in Figures 4, S4-7 and Table 1) were performed using a 5 mm NMR tube with **EuL** dissolved in 9:1 mixture H_2O:D_2O (v/v). The CEST experiments with shorter saturation (5 s) were performed using a 5 mm NMR tube filled with aqueous solution of **EuL** or iopamidol and a smaller 2 mm NMR tube (1.6 mm inner diameter) filled with D_2O. For data evaluation, Z-spectra were normalized by an unsaturated fully relaxed water signal M_0. The CEST effect was calculated employing the inverse asymmetry analysis of the normalized Z-magnetization. The inverse difference of the magnetization transfer, MTR_{ind}, was calculated according to Eq. 1, where M_0 is the unsaturated water magnetization,

while M_{z+} and M_{z-} are magnetizations of the on-resonance at the frequency +Δω and of the off-resonance at the frequency -Δω relative to bulk water, respectively.[10]

$$MTR_{ind} = \frac{M_0}{M_{z+}} - \frac{M_0}{M_{z-}} \quad (1)$$

Simultaneous multi-B_1 *Z*-spectra fitting was performed as described in previous work,[11] using the tool published online.[12]

MRI experiments

MRI measurements on tube phantoms were performed on Bruker BioSpec 70/30 USR magnet (software version Paravision 5.1) using Bruker volume coil (RF RES 300 1H 075/040 QSN TR). The MRI phantom consisted of 6 vials filled with **EuL** solution in PBS (3 mM) and the pH ranging from 6.0 to 8.0.

Z-spectra were acquired at 25 ^{o}C with 139 irradiation offsets ranging from 20 to -20 ppm, saturation pulse duration of 5 s, and five different radiofrequency field strengths, B_1= 3, 4, 5, 6 and 7.5 μT.

Presaturated MR images were acquired using rapid acquisition with relaxation enhancement (RARE) imaging protocol with the following parameters: repetition time (TR) / echo time (TE) =15316.18 / 3.26 ms, field of view (FOV)=48 x 48 mm^2, matrix size (MTX)=96 x 96, slice thickness 2 mm, Rare factor=96, number of excitation (NEX)=1, acquisition time (TA)=35 min 28 s 948 ms.

Image analysis was performed in MATLAB (MathWorks, USA). Z-spectrum images were interpolated by splines and shifted to the centre frequency in order to remove B_0 inhomogeneity artefacts.

pH evaluation using ratiometric method was done using the inverse matrix approach, as described above in Eq. 1. For generating pH maps, the pH values were plotted as a function of the corresponding MTR_{ind} ratio values. The obtained values were fitted using an exponential function according to Eq. 2, yielding a monotonic function pH(MTR_{ind} ratio). This function was then applied pixel-wise to MTR_{ind} ratio maps to generate the pH maps.

$$pH = c - a \times e^{-b \times MTR_{ind}\, ratio} \quad (2)$$

Figures and Tables

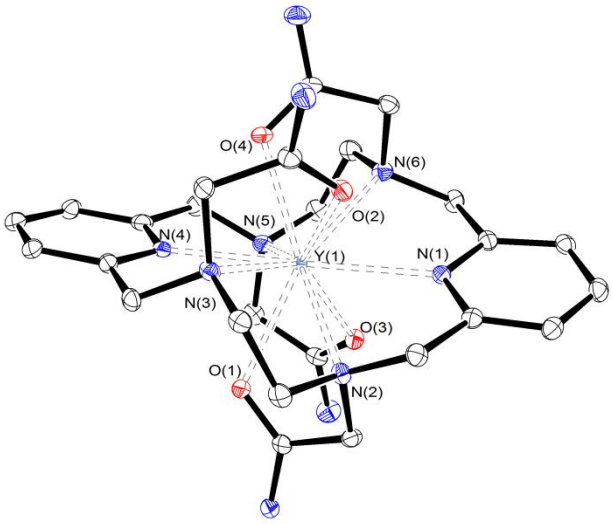

Figure S1. View of the structure of the $[\mathbf{YL}]^{3+}$ cation present in crystals of $[\mathbf{YL}](NO_3)_3 \cdot 3H_2O$. Hydrogen atoms are omitted for simplicity.

Table S1. Bond distances (Å) of the metal-coordination environments observed in the X-ray structures of $[LnL]^{3+}$ complexes (Ln=Eu or Y).

Eu(1)-N(1)	2.594(15)	Y(1)-N(1)	2.568(4)
Eu(1)-N(2)	2.63(2)	Y(1)-N(2)	2.640(5)
Eu(1)-N(3)	2.644(19)	Y(1)-N(3)	2.641(5)
Eu(1)-O(1)	2.525(16)	Y(1)-N(4)	2.555(4)
Eu(1)-O(2)	2.511(15)	Y(1)-N(5)	2.652(5)
		Y(1)-N(6)	2.643(5)
		Y(1)-O(1)	2.527(4)
		Y(1)-O(2)	2.481(4)
		Y(1)-O(3)	2.445(4)
		Y(1)-O(4)	2.413(4)

Table S2. Crystal Data and Structure Refinement for the complexes.

	[EuL](NO$_3$)$_3$·3H$_2$O	**[YL](NO$_3$)$_3$·3H$_2$O**
formula	C_{26} H_{38} N_{10} O_4 Eu	C_{26} H_{44} N_{13} O_{16} Y
mol wt	706.63	883.65
cryst syst	Monoclinic	Monoclinic
space group	C2	C2
a (Å) α (deg)	24.258(13)	25.049(5)
b (Å) β (deg)	12.124(7) 133.831(4)	11.926(5) 91.946(5)
c (Å) γ (deg)	17.312(9)	23.702(5)
V(Å^3)	3673(3)	7077(4)
Z	4	8
D(calc) (Mg/m^3)	1.278	1.659
μ (mm^{-1})	1.748	1.741
Flack param.	0.10(3)	0.243(6)
R_{int}	0.1215	0.0559
R_1[a]	0.0834	0.0569
wR_2 (all data)[b]	0.2291	0.1524

[a] $R_1 = \Sigma||F_o|-|F_c||/\Sigma|F_o|$. [b] $wR_2 = \{\Sigma[w(||F_o|^2-|F_c|^2|)^2]/\Sigma[w(F_o^4|)]\}^{1/2}$

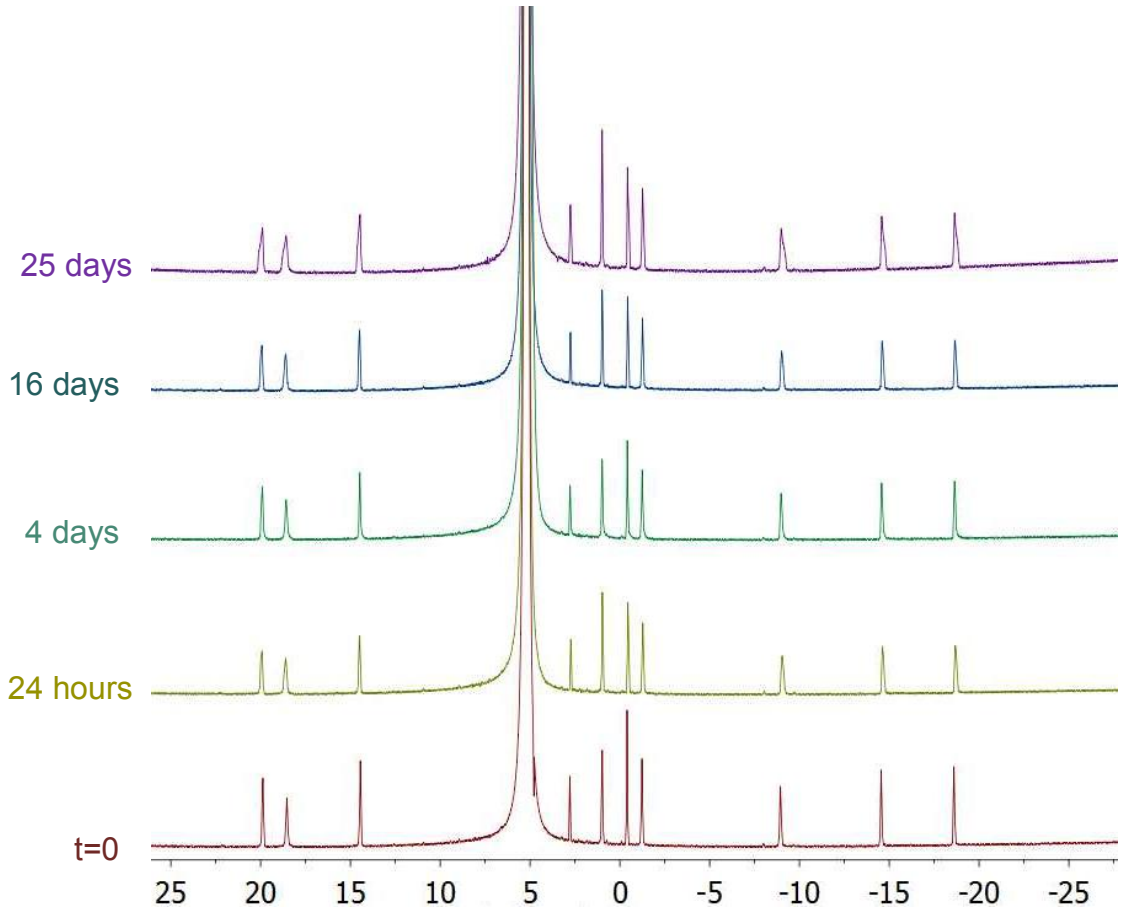

Figure S2. ^{1}H NMR spectra (400 MHz) of **EuL** recorded in 1 M HCl at 25 ºC over time.

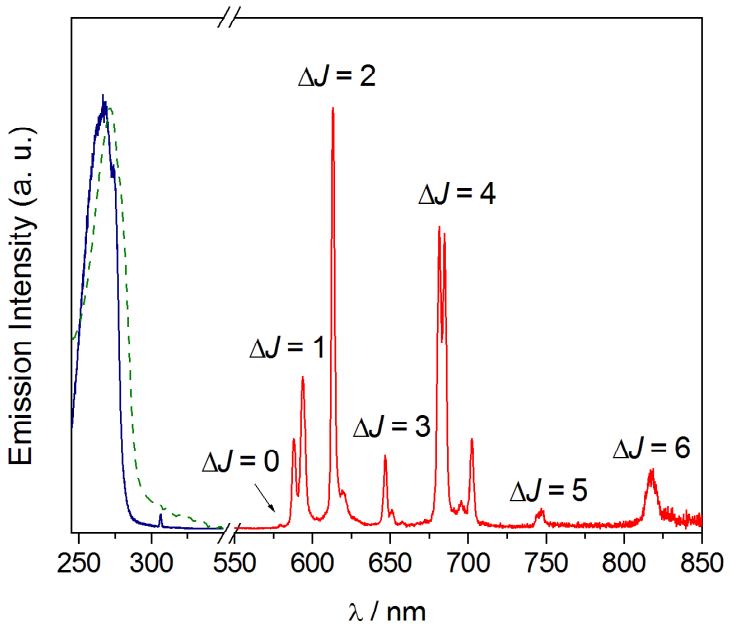

Figure S3. UV-Vis absorption (dashed green line), excitation (solid blue line) and emission (solid red line) spectra of **EuL** recorded in water (10^{-5} M). λ_{exc} = 268 nm, λ_{em} = 613 nm.

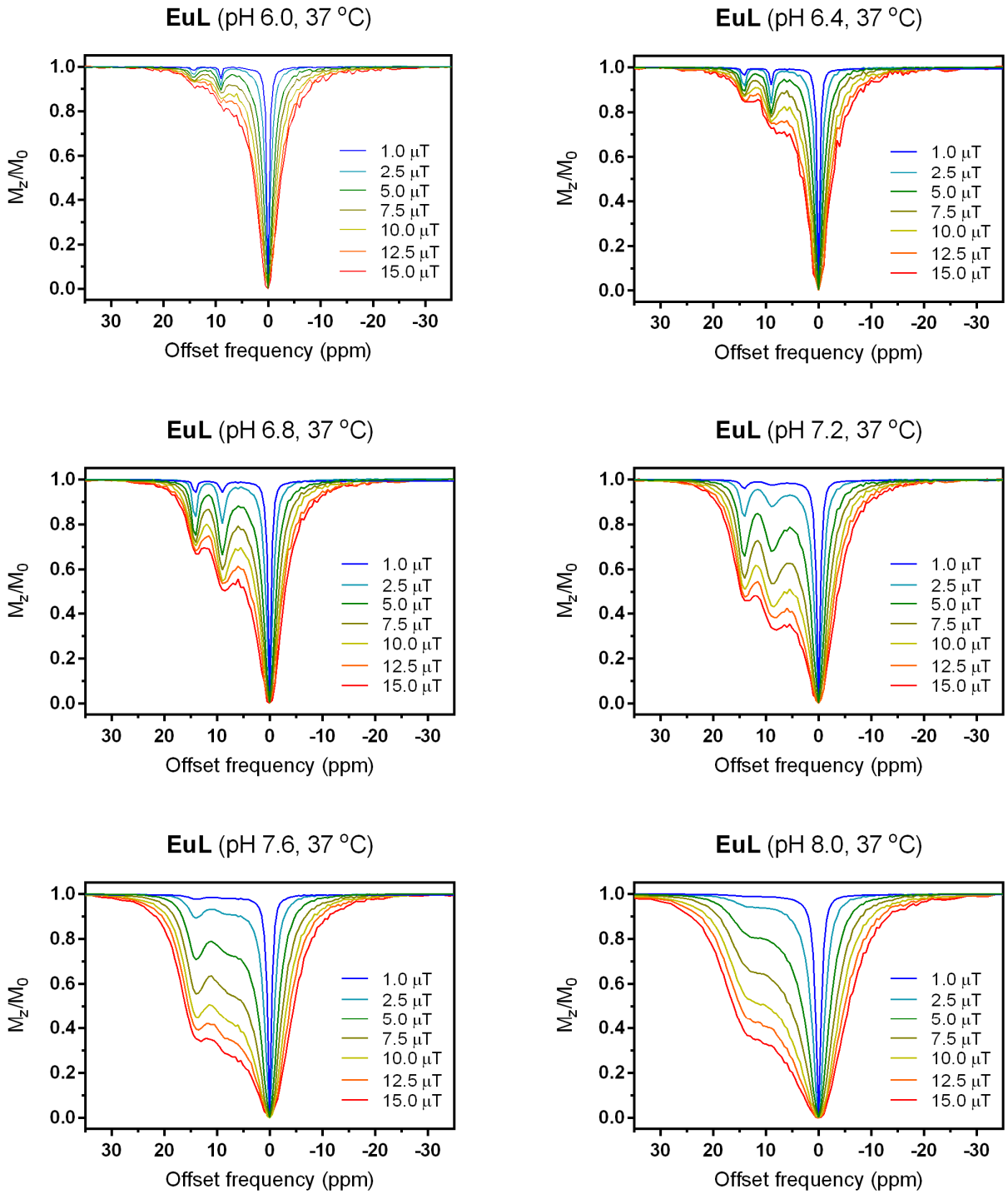

Figure S4. Z-spectra of **EuL** (5 mM in PBS) at variable pH and B_1 fields, irradiation time of 15 s and 37 °C.

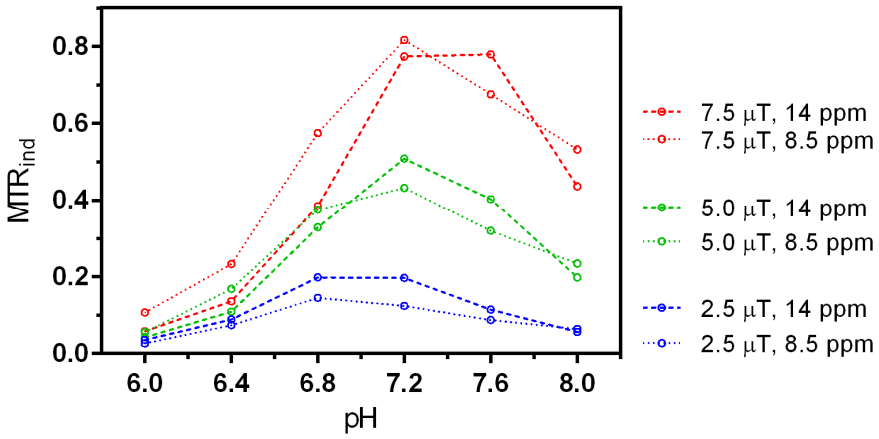

Figure S5. MTR_{ind} as a function of pH (5 mM **EuL** in PBS, 37 ^{o}C).

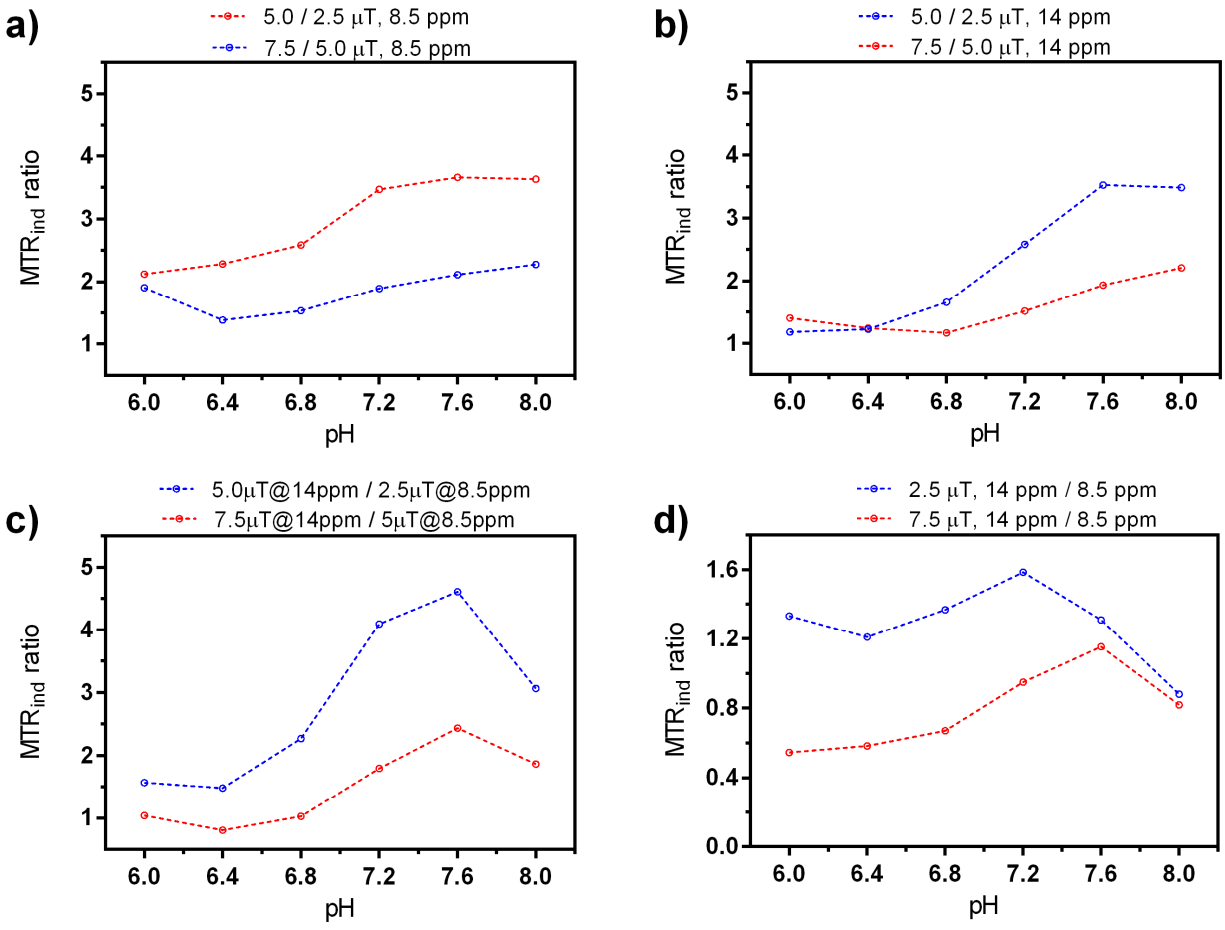

Figure S6. Ratio of MTR_{ind} for **EuL** (5 mM in PBS, 37 ^{o}C, NMR spectrometer) at varying pH values: a) signals obtained at same frequency (8.5 ppm) and different B_1; b) signals obtained at same frequency (14 ppm) and different B_1; c) signals obtained at different frequencies and different B_1; d) signals obtained at different frequencies and same B_1.

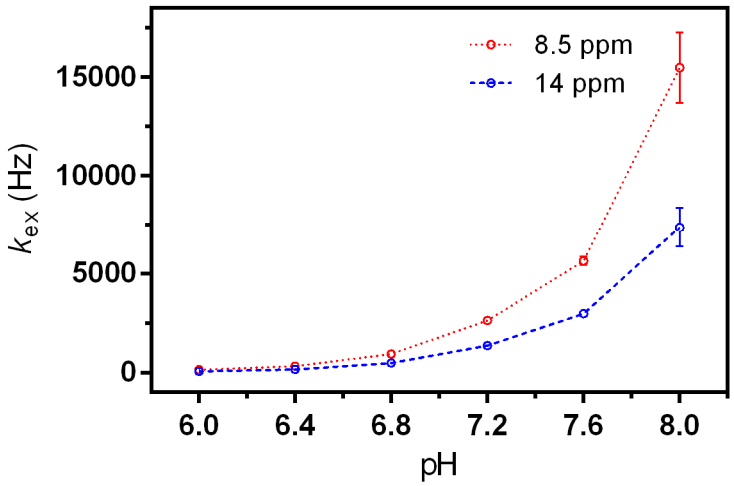

Figure S7. Exchange rate values obtained at different pH using the qCEST method (5 mM **EuL** in PBS, 37 ^{o}C).

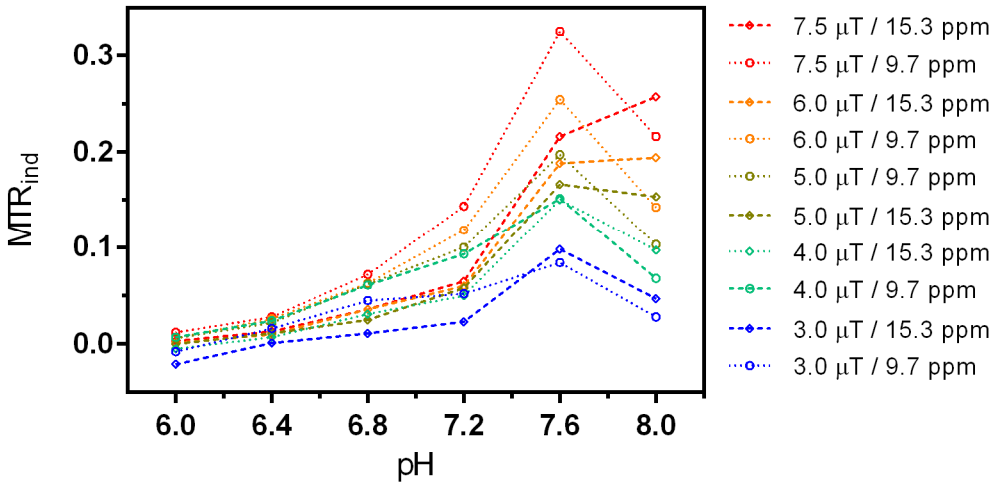

Figure S8. MTR_{ind} as a function of pH, obtained from experiments performed in the MRI scanner (3 mM **EuL** in PBS, RT).

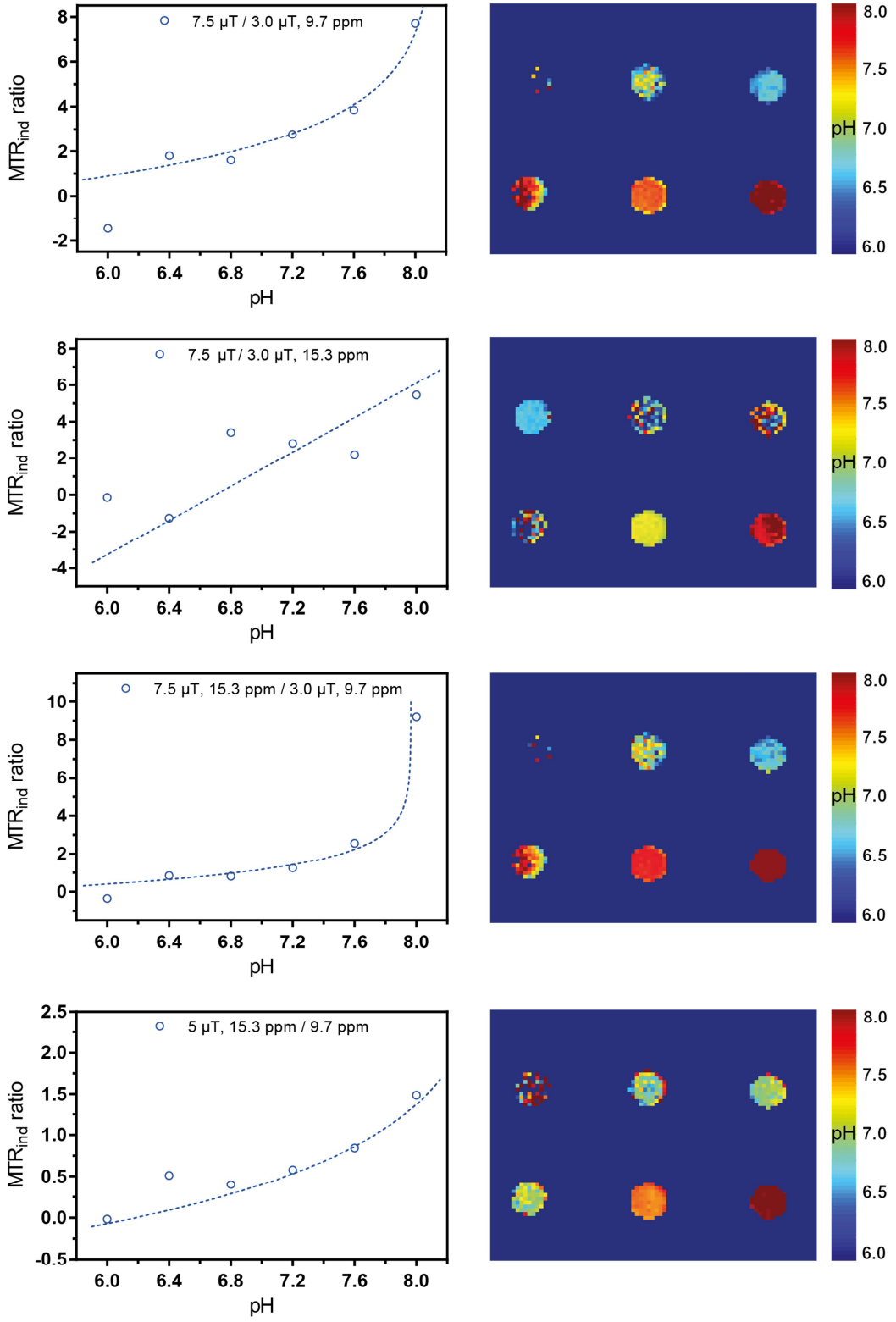

Figure S9. pH maps (right) obtained from MTR_{ind} ratio (left) on MRI tube phantoms (3 mM **EuL** in PBS, RT).

References

[1] G. R. Fulmer, A. J. M. Miller, N. H. Sherden, H. E. Gottlieb, A. Nudelman, B. M. Stoltz, J. E. Bercaw, K. I. Goldberg, *Organometallics* **2010**, *29*, 2176-2179.

[2] A. S. Chauvin, F. Gumy, D. Imbert, J. C. G. Bunzli, *Spectrosc Lett* **2004**, *37*, 517-532.

[3] P. A. Brayshaw, J. C. G. Bunzli, P. Froidevaux, J. M. Harrowfield, Y. Kim, A. N. Sobolev, *Inorg. Chem.* **1995**, *34*, 2068-2076.

[4] G. L. Rothermel, L. Miao, A. L. Hill, S. C. Jackels, *Inorg. Chem.* **1992**, *31*, 4854-4859.

[5] Bruker, *SAINT*. **2012**, Bruker AXS Inc., Madison, Wisconsin, USA.

[6] G. M. Sheldrick, *SADABS, Program for Empirical Absorption Correction of Area Detector Data.* **1996**, University of Götingen, Germany.

[7] G. M. Sheldrick, *Acta Crystallogr. A* **2015**, *71*, 3-8.

[8] P. Vandersluis, A. L. Spek, *Acta Crystallogr. A* **1990**, *46*, 194-201.

[9] L. J. Farrugia, *J. Appl. Cryst.* **1997**, *30*, 565.

[10] M. Zaiss, J. Z. Xu, S. Goerke, I. S. Khan, R. J. Singer, J. C. Gore, D. F. Gochberg, P. Bachert, *NMR Biomed.* **2014**, *27*, 240-252.

[11] M. Zaiss, G. Angelovski, E. Demetriou, M. T. McMahon, X. Golay, K. Scheffler, *Magn. Reson. Med.* **2018**, *79*, 1708-1721.

[12] http://cest-sources.org/doku.php?id=bm_sim_fit